Spectral continuation study of the temporally periodic solitons of the damped-driven nonlinear Schrödinger equations.

James Lee-Thorp

Thesis presented for the degree of Master of Science in the Department of Mathematics and Applied Mathematics, University of Cape Town.

August 22, 2012

Plagiarism declaration

I know the meaning of plagiarism and declare that all of the work in this document, save for that which is properly acknowledged, is my own.

Abstract

In this thesis we develop and employ a spectral continuation algorithm, implemented in AUTO [30], to study the temporally periodic spatially localised soliton solutions of the driven, damped nonlinear Schrödinger equations, both in the case of parametric driving and direct driving. We hope that this study is of interest not only in the context of the nonlinear Schrödinger equations but also separately as a study of an efficient numerical algorithm for continuing (path-following) solutions to general two-dimensional periodic soliton bearing PDEs.

Previous studies have described much of the structure of the stationary and time-periodic soliton solutions of the parametrically driven, damped nonlinear Schrödinger equation, with particular focus on the strong to moderately damped cases. We aim to extend these works by investigating two regimes which, up until now, have been inaccessible due to numerical difficulties: namely, large-period solutions and the case of weak damping. With numerical access to large-period solutions we are able to fully reveal the characteristic snaking structure of the bifurcation diagram for the moderate damping regime and relate the observed structure to Shil'nikov's theorems. In the weakly damped regime we observe the appearance of new regions of stable periodic solutions along with the emergence of finer structure. This latter phenomenon is investigated in some detail and found to be a result of the finite, periodic spatial interval upon which we numerically study solutions, and the increased presence of large amplitude radiation waves.

There have been significantly fewer studies of the time-periodic soliton solutions of directly driven, damped nonlinear Schrödinger equation. We offer a cursory investigation of such solutions and construct an overview of the dynamics that arise in the different damping regimes. In the strongly damped case, we find that the phase space of periodic solutions is characterised by the transformation of the single periodic soliton into a periodic soliton complex. Similar dynamics arise in the moderately damped system, but in addition period doubling is observed. No soliton complexes are observed in the weakly damped regime, where the system dynamics are dominated by large-amplitude radiation waves. Broadly speaking, the dynamics observed in directly driven case show many similarities with those in the parametrically driven case and we take the time to highlight several of these parallels.

Contents

Chapter 1

Introduction

The recipe for computing general solutions to linear equations is neatly encoded in the linear superposition principle. With the help of the superposition principle then, we are able to obtain a complete picture of linear systems. However, no such standard prescription exists for finding the general solution of nonlinear equations. Instead we are forced to investigate specific cases in the hope that we can obtain a good understanding of how the nonlinear system behaves.

Particular nonlinear solutions of great interest are localised solutions, which crop up in a great variety of forms in physical, chemical and biological processes. Indeed such solutions (or states) have been observed in experiments spanning all these fields: from vertically vibrated granular materials [37, 82], ferrofluids in an applied vertical DC magnetic field [70], nonlinear optics [62, 71, 79] and liquid crystals [19] to autocatalytic chemical reactions such as in the Belousov-Zhabotinsky system [25, 83]. In addition, localised solutions have received a surge of interest recently [20, 56] for the rich structure they exhibit.

The localised solutions that will be of interest in the present work are the temporally periodic soliton solutions of the driven, damped nonlinear Schrödinger equations. We will be using numerical continuation to study these solutions. This thesis is therefore concerned firstly with the development of a numerical spectral continuation algorithm which is of general applicability to two dimensional partial differential equations (PDEs) possessing some form of periodicity; and secondly, with the study of the periodic solitons of the driven, damped nonlinear Schrödinger equations.

As this dissertation is born out of the author's previous work [55], the focus of the present study is on the *parametrically driven*, damped nonlinear Schrödinger equation, which we henceforth abbreviate as the parametrically driven NLS. Indeed, the bulk of our investigation centres around understanding the dynamics of the periodic soliton solutions of the parametrically driven NLS in different damping regimes and expounding on previous

works [10, 11, 14, 15, 18, 84]. However, given the broad applicability of our continuation algorithm we have extended our work to include a cursory investigation of the temporally periodic soliton solutions of the *directly driven* damped nonlinear Schrödinger equation, henceforth referred to as the directly driven NLS. This supplementary work exemplifies the robustness of our algorithm and is further motivated by the lack of previous studies pertaining to the periodic solutions of the directly driven NLS, with the notable exception of [76]. Much attention [7, 8, 9, 13, 23, 60, 61, 78] has, however, been given to the stationary soliton solutions of the directly driven NLS and those works lay the groundwork for our study.

In contrast to the directly driven system, significant progress [10, 11, 14, 15, 18, 84] has been made in understanding the dynamics of the temporally periodic solitons of the parametrically driven NLS. Nevertheless, two regimes in particular have been difficult to investigate: large-period periodic solitons in general and periodic solitons in the weakly damped system. The difficulties in examining both these regimes are numerical, the former due to the presence of large-amplitude radiation waves and the later due to the accuracy and robustness of the numerical algorithms. Further discussion of these difficulties and how the spectral algorithm employed in this work avoids them is included in §4.1.1, where we discuss our continuation algorithm in detail.

While a great amount of work has been put into describing the soliton solutions of the parametrically driven NLS and its bifurcating structure, it is still not completely clear what the mechanisms explaining this bifurcation structure actually are. The characteristic snaking structure of the bifurcation curves in the moderately damped regime of the periodic single-soliton, for instance, has been identified in a recent study by Barashenkov, Zemlyanaya and van Heerden [15] but is still not well understood. Building on our numerical investigation we will relate these dynamics to Shil'nikov's results. This investigation carries further interest in the context of general applied bifurcation theory as a case study wherein Shil'nikov's classical *finite* dimensional system results are applicable to an (*infinite* dimensional) PDE.

The rest of this dissertation is organised as follows. In the remainder of this introductory chapter we consider the parametrically driven NLS and its stationary soliton solutions and review several relevant numerical continuation studies. We then present a brief introduction to the directly driven NLS and its stationary soliton solutions. Chapter 2 covers elements from bifurcation analysis and, in particular, Shil'nikov's theorems, which will be pertinent to our numerical study of the parametrically driven NLS. Chapter 3 gives an introduction to the elementary principles of numerical continuation, with particular focus on the methods employed by AUTO [30]. In Chapter 4 we provide the details of our numerical algorithms: the spectral continuation algorithm that is our primary tool in this work along with a

direct numerical simulation (integration) algorithm, the split-step Fourier method, which we will use to verify the stability of solutions. Our main results from the continuation of moderately and weakly damped temporally periodic solitons of the parametrically driven NLS are presented in Chapter 5, including the application of Shil'nikov's results and detailed discussions of the observed fine structure. We close Chapter 5 with the construction of the bifurcation diagram for the periodic solitons of the parametrically driven NLS. Chapter 6 then gives a cursory study of the temporally periodic soliton solutions of the directly driven NLS. Finally, a brief summary of results along with concluding remarks can be found in Chapter 7.

1.1 The parametrically driven NLS

An intuitive introduction to the parametrically driven NLS is given in [11], which we paraphrase here. We begin with the nonlinear Schrödinger equation in the case of a cubic nonlinearity and subject to a generic small dissipative term:

$$i\Psi_t + \Psi_{xx} + 2|\Psi|^2\Psi = -i\gamma\Psi, \quad \gamma > 0. \tag{1.1}$$

Left to its own devices any solution satisfying equation (1.1) will quickly decay to zero. This dissipation can be compensated for by pumping energy into the system. The energy input typically takes the form of a driving term, which is either direct (external) driving (cf. §1.2) or parametric driving. In the latter case, the form of the corresponding amplitude equation is

$$i\Psi_t + \Psi_{xx} + 2|\Psi|^2\Psi = h\Psi^* e^{i\Omega t} - i\gamma\Psi, \tag{1.2}$$

where the star indicates complex conjugation.

Now, if $\Psi(x,t)$ is a solution to equation (1.2) corresponding to the parameters h, γ, and Ω, then $\widetilde{\Psi}(x,t) = k\Psi(kx, k^2t)$ is the solution corresponding to $\widetilde{h} = k^2h$, $\widetilde{\Omega} = k^2\Omega$, and $\widetilde{\gamma} = k^2\gamma$. Thus only two of the three parameters h, γ, and Ω, are significant and we can always fix the third parameter [6, 78] in an effort to reduce our three parameter study to a two parameter study. Moreover, the U(1) invariance of the unperturbed nonlinear Schrödinger equation allows us to render equation (1.2) autonomous. Indeed, normalising the driving frequency Ω to unity before making the substitution $\Psi(x,t) = e^{it}\psi(x,t)$ and simplifying, transforms equation (1.2) into the standard form of the parametrically driven NLS:

$$i\psi_t + \psi_{xx} + 2|\psi|^2\psi - \psi = h\psi^* - i\gamma\psi. \tag{1.3}$$

Equation (1.3) finds application as a model of resonant phenomena in a variety of physical contexts in nonlinear dispersive media, including the nonlinear Faraday resonance in a vertically oscillating water trough [33, 54, 67], synchronisation in parametrically excited pendula arrays [24], and the

propagation of magnetization waves in an easy-plane ferromagnet placed in a microwave field [5]. It also governs the amplitude of breather solutions in a variety of systems reducible to the parametrically driven damped sine-Gordon [5] and the ϕ^4 [49] equations; Barashenkov, Bogdan and Korobov [5] offer a perturbation expansion derivation of the parametrically driven NLS from the sine-Gordon equation. The interested reader is referred to [15] and references therein for further contexts.

Two stationary soliton solutions of the parametrically driven NLS (1.3) are known analytically:

$$\psi_\pm(x) = A_\pm \mathrm{sech}(A_\pm x) e^{-i\theta_\pm}, \tag{1.4}$$

where

$$A_\pm = \sqrt{1 \pm \sqrt{h^2 - \gamma^2}}, \quad \theta_+ = \frac{1}{2}\arcsin\frac{\gamma}{h}, \quad \theta_- = \frac{\pi}{2} - \theta_+. \tag{1.5}$$

Although we will be chiefly interested in single-soliton solutions, we mention that the ψ_+ and ψ_- solitons can form a variety of soliton complexes [12].

The stationary ψ_- soliton exists in the parameter range $\gamma \le h \le h_{\mathrm{cont}}(y)$, where

$$h_{\mathrm{cont}} = \sqrt{1+\gamma^2}, \tag{1.6}$$

and is unstable for all driving strengths h and all damping γ [5, 54]. As an unstable solution, the ψ_- soliton will be of little physical interest, but it will play a central role in understanding the dynamics of the parametrically driven NLS in relation to Shil'nikov's results [74, 75] in §5.2. As such, we take the time to discuss its eigenvalues.

To study the eigenvalues of the ψ_- soliton we linearise equation (1.3) about $\psi(x,t) = \psi_-(x) + \delta\psi(x,t)$, where

$$\delta\psi(x,t) = e^{-i\theta_-}\left[u(x,t) + v(x,t)\right]$$

is a small perturbation. Taking the ansatz

$$u(x,t) = \mathrm{Re}\left(e^{\lambda t}p(x)\right), \quad v(x,t) = \mathrm{Re}\left(e^{\lambda t}q(x)\right),$$

with p, q and λ complex, yields the eigenvalue problem [15]

$$L_1 p + 2\widetilde{\gamma} q = -\widetilde{\lambda} q, \quad (L_0 + \epsilon) q = \widetilde{\lambda} p. \tag{1.7}$$

Here $\widetilde{\gamma} = \gamma/A_-^2$ and $\widetilde{\lambda} = \lambda/A_-^2$, and two Sturm-Liouville operators have been introduced:

$$L_0 = -d^2/dX^2 + 1 - 2\mathrm{sech}^2 X,$$
$$L_1 = -d^2/dX^2 + 1 - 6\mathrm{sech}^2 X.$$

The independent variable x has been rescaled as $X = A_- x$ and the parameter ϵ is defined by

$$\epsilon = \sqrt{h^2 - \gamma^2}/A_-^2. \tag{1.8}$$

The two-parameter eigenvalue problem (1.7) can be solved [15] to find the eigenvalues λ; a summary of results is given below.

Firstly, the ψ_- soliton has one zero stability eigenvalue,

$$\lambda_0 = 0,$$

originating from the translation invariance of the parametrically driven NLS (1.3). It is important to note that because this zero mode is a result of translation invariance of the system itself, it will persist under all C^1 perturbations to the ψ_- soliton. That is to say, that, for all h and γ for which the ψ_- soliton is defined it will carry this zero mode. This observation will be important when we seek to understand the dynamics of the parametrically driven NLS in light of Shil'nikov's results; Chapter 2 gives further details.

The linear spectrum of the ψ_- soliton consists of a continuum of values,

$$\lambda = -\gamma + i\omega, \tag{1.9}$$

where $|\omega| \geq \omega_0$, $\omega_0 = \sqrt{1 - h^2}$, and two discrete eigenvalues,

$$\lambda_\pm = -\gamma \pm \sqrt{\gamma^2 + A_-^4 \Lambda_0^2}, \tag{1.10}$$

where $\Lambda_0 = \Lambda_0(\epsilon)$ with ϵ defined in equation (1.8). The function $\Lambda_0(\epsilon)$ has the asymptotic behaviours $\Lambda_0 \to (4\epsilon)^{1/2}$ as $\epsilon \to 0$ and $\Lambda_0 \to (3\epsilon)^{1/2}$ as $\epsilon \to \infty$, and intermediate values of Λ_0 have been computed numerically [15]. In particular, for future reference (cf. §5.2), we have for $h = 0.385$ and $\gamma = 0.2$ that $\epsilon = 0.983$ and therefore that [15]

$$\lambda_+ = 1.025. \tag{1.11}$$

The stationary ψ_+ soliton on the other hand exists for all $h \geq \gamma$ and its stability properties depend on both h and γ. For strong damping, $\gamma > 0.356$ [5], the ψ_+ soliton is stable for all driving strengths h satisfying $\gamma < h < h_{\text{cont}}(\gamma)$. For moderate and weak damping, $\gamma < 0.356$, the ψ_+ soliton is only stable for $\gamma < h < h_{\text{Hopf}}(\gamma)$, where $h_{\text{Hopf}}(\gamma)$ is the point of Hopf bifurcation which lies between γ and $h_{\text{cont}}(\gamma)$. For larger driving strengths, $h > h_{\text{Hopf}}(\gamma)$, the stationary ψ_+ soliton loses its stability to a time-periodic soliton [2, 5] (see curve 1 in Figure 1.1). Increasing the driving strength h further leads to complicated dynamics which depend on the (fixed) value of γ.

Bondila, Barashenkov and Bogdan [18] made an attempt to classify these dynamics by direct numerical simulation. Their attractor chart is reproduced in Figure 1.1. In the chart, curve 1 indicates the value of the Hopf

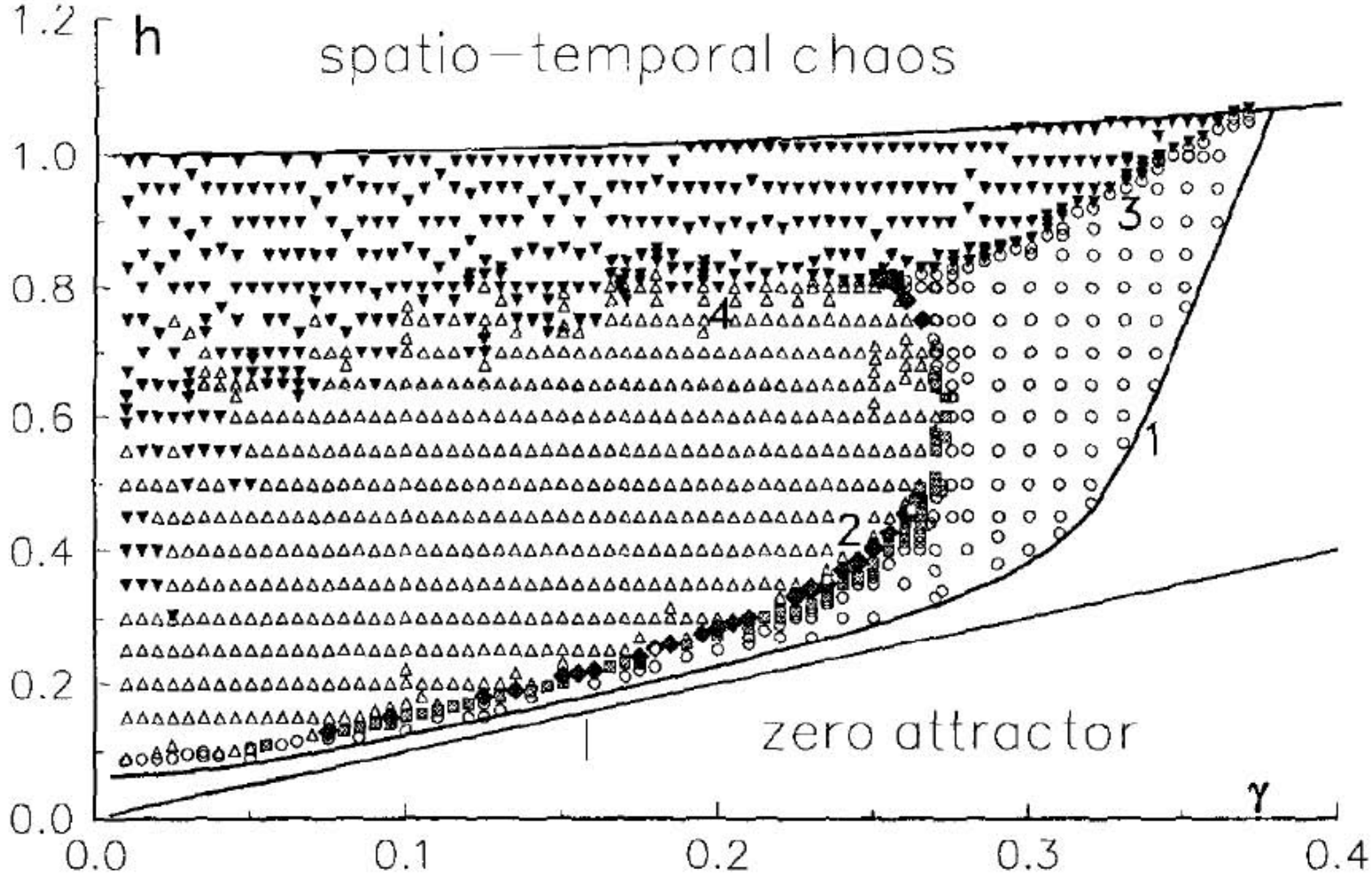

Figure 1.1: Attractor chart reproduced from Bondila *et al* [13] with their annotation. "Below the line $h = \gamma$ there are no localised solutions, and the only attractor is $\psi = 0$. Above the line $h = (1 + \gamma^2)^{1/2}$, the zero solution is unstable with respect to the excitation of continuous spectrum waves. In the area between these two lines, we used empty circles to denote period-I solitons and shadowed boxes for periods 2 and 3. Small white blobs indicate period-6, period-7 and period-10 solitons observed at $(\gamma = 0.202, h = 0.48)$, $(\gamma = 0.235, h = 0.355)$ and $(\gamma = 0.18, h = 0.254)$, respectively. Finally, shadowed diamonds stand for type-I and type-II strange attractors observed at $(\gamma = 0.18, h = 0.253)$ and $(\gamma = 0.26, 0.4530 < h < 0.4539)$, respectively, as well as for complex cycles. The region of stable stationary solitons is left blank; empty triangles mark the area where the only attractor is $\psi = 0$, and the domain of spatio-temporal chaos is marked by black triangles. Note an unexpectedly complex, "shark jaw" shape of the interface between the regions of spatio-temporal chaos and zero attractor."

Figure 1.1: Single soliton attractor chart for the parametrically driven NLS compiled by direct numerical simulations [18]. In the blank area below the line $h = \gamma$ the only attractors are stationary solitons. The complicated dynamics of the system are found in the band between the upper unlabelled curve ($h_{2\to4}(\gamma)$) and curve 1 ($h_{1\to\infty}(\gamma)$). The "desert" area where only the trivial attractor is found is marked by empty triangles. Empty circles indicate stable periodic solitons; black triangles represent spatio-temporal chaos. Other symbols mark stable higher-periodic and temporally chaotic solitons. For further details the reader is referred to [18].

bifurcation of the ψ_+ soliton. The $h_{\text{cont}}(\gamma)$ (1.6) curve is given by the upper (unlabelled) curve. It is between these two curves that the complicated dynamics of the parametrically driven NLS arise.

Specifically, the direct numerical simulations revealed that for $\gamma \lessapprox 0.25$, increasing the driving strength h results in the periodic soliton following a period-doubling route to temporal chaos. Increasing h further beyond this chaotic domain leads to a "desert" region where the parametrically driven NLS does not support any stable spatially localised solutions and the only attractor is the trivial one $\psi = 0$. Finally, for very large driving strengths h we find spatio-temporal chaos seeded by the unstable soliton [18] (see also [38]).

For strong damping $\gamma \gtrapprox 0.275$, the transformation of the soliton is different: the periodic soliton remains stable until it yields to a spatio-temporal chaotic state [18]. In the intermediate damping region $0.25 < \gamma < 0.275$ the soliton transformation is a combination of the scenarios seen in the two complementary regions. As the driving strength h is increased in this intermediate damping region, the soliton first follows a period-doubling route to temporal chaos before it dies out to the trivial solution. Further increase in the driving strength h results in the recovery of the stable periodic soliton before it too loses its stability to a spatio-temporal chaotic state [18]. This discussion is neatly summarised in the attractor chart in Figure 1.1.

The chart does not include any simulations with zero damping. Insight into this case is provided by Alexeeva, Barashenkov and Pelinovsky [2] who derived a reduced amplitude equation (using a multi-scale expansion) governing the behaviour of the undamped parametrically driven NLS. Their analytical work suggested that no periodic solution exists for $\gamma = 0$ due to the proximity of the continuous spectrum of the stationary solitons. They also provided direct numerical simulation verifying this. In §5.3.3 we will investigate the undamped periodic solutions of the parametrically driven NLS in detail. There we will find that undamped periodic solutions do in fact exist, but only on a *finite periodic* spatial interval. This is not in contradiction to [2] who studied the periodic solutions on an *infinite* spatial interval; the full details are in §5.3.3.

We reiterate that all of the numerical results discussed above were obtained from direct simulation of the parametrically driven NLS. It is therefore natural to question the robustness of these results. For example, would changing the parameters of the numerical scheme or the initial condition alter the qualitative features of the attractor chart? Furthermore, given that direct simulation can only ever capture the behaviour of stable solutions, we do not have a *complete* picture of the behaviour of the system.

1.1.1 Numerical continuation and the parametrically driven NLS

In an effort to answer these questions, Barashenkov, Zemlyanaya and van Heerden [15] and Zemlyanaya and Alexeeva [86] employed numerical continuation to investigate the periodic solitons. They were able to verify many of results of the direct numerical simulations as well as investigate *unstable* periodic solitons. In this section we discuss their work and offer a brief account of previous numerical continuation on the parametrically driven NLS and related work relevant to our application.

Both studies [15, 86] found that in the strongly damped regime ($\gamma > 0.275$), the parametrically driven NLS does indeed support stable periodic solutions. The bifurcating behaviour of these solutions was examined as a function of the driving strength h and, notably, the transformation of single-solitons into soliton complexes was observed. For weaker damping ($\gamma < 0.25$), period-doubling bifurcations of the periodic solution were observed along with a characteristic snaking structure of the bifurcating curve. For intermediate damping ($0.25 < \gamma < 0.275$), they noted a composite behaviour between the two aforementioned regimes as the periodic solitons were continued (path-followed) in h. The results are summarised in the attractor chart of Barashenkov, Zemlyanaya and van Heerden [15] [15], which we reproduce in Figure 1.2.

Prior to this work, Barashenkov and Zemlyanaya [10] identified stable and unstable complexes of the parametrically driven NLS using numerical continuation, and later [11, 14] showed that some of these complexes travel without violating momentum conservation. The behaviour of the stationary ψ_+ soliton and the periodic soliton produced at the point of Hopf bifurcation of the stationary ψ_+ soliton is also discussed extensively by van Heerden [84].

In Chapter 3 we will delve into the specifics of numerical continuation, but for the time being it suffices to state that the only solutions we will be able to continue are solutions governed by ordinary differential equations (ODEs). As the parametrically driven NLS is a PDE it therefore needs to be reduced to a systems of ODEs. In all of the previous studies of the parametrically driven NLS discussed above, this discretisation was achieved using finite differences.

Our aim in this work is to implement an alternate discretisation using Fourier expansions. In this respect we draw inspiration from Melvin, Champneys, Kevrekidis and Cuevas [64, 65] and Pelinovsky, Melvin and Champneys [66, 69], who, based on previous work [1, 31, 32], investigated travelling waves in the discrete nonlinear Schrödinger equation using a spectral continuation approach.

Zemlyanaya and Alexeeva [87] adopted a similar spectral analysis approach, studying the bifurcating structure of the parametrically driven NLS. More specifically, modelling the system as a boundary value problem formu-

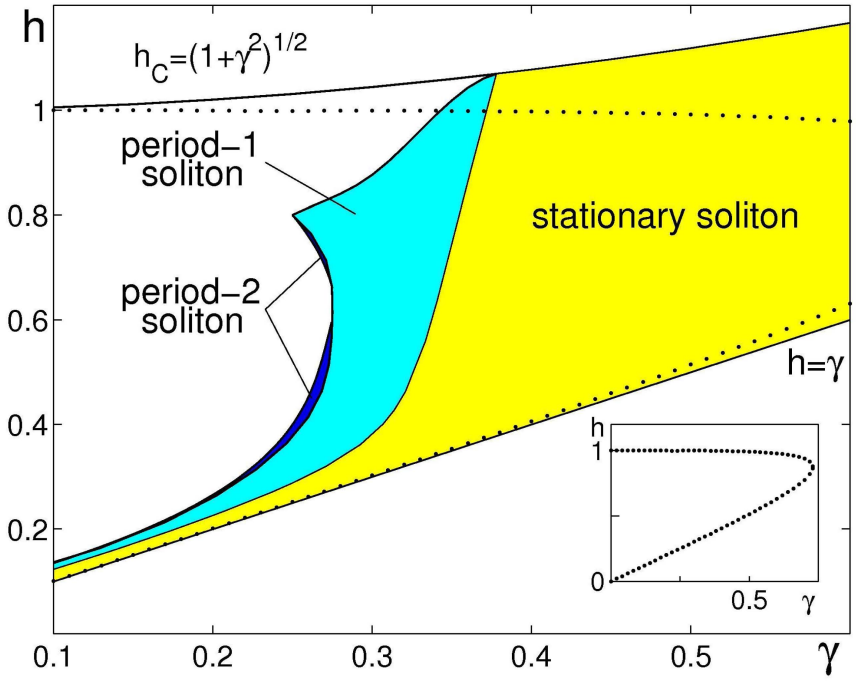

FIG. 2.7: Single-soliton attractor chart produced from [15]. The chart was constructed by interpolating (21) bifurcation points computed through numerical continuation. The inset gives a reduced perspective of this region.

Figure 1.2: Single-soliton attractor chart reproduced from [15]. The chart was constructed by interpolating (21) bifurcation points computed through numerical continuation. Figure 1.2 gives a reduced perspective of this region, produced using direct numerical simulations, Figure 1.1.

lated on a two-dimensional periodic domain and using a low order Fourier expansion (zeroth, first and second order harmonics only), they investigated the domain of existence and stability of the stable time-periodic soliton for $\gamma = 0.27$.

odic solitons are observed in numerical simulations. The question here is why does the $h(\gamma)$ curve bounding this region fold on itself for γ between 0.25 and 0.275.

This phenomenon is accounted for by the restabilisation of the periodic soliton as h is increased for $\gamma = 0.265$ (Fig.5). We note that the case $\gamma = 0.265$ is intermediate between the small- and large-γ transformation scenarios.

On the one hand, similar to the weakly-damped scenario, the soliton undergoes a period-doubling cascade as h is raised for this γ (more precisely, it undergoes *two* period-doubling cascades). On the other, the domain occupied by the periodic attractor is bounded by a saddle-node bifurcation in this case, as in the strongly-damped situation.

Fig.7 summarises our conclusions on single-soliton periodic attractors. This diagram is in a good agreement with the attractor chart produced using direct numerical simulations, Fig.1.

Naturally, the nonlinear Schrödinger equation has not been the only focus of spectral continuation schemes. In particular we draw the reader's attention to Lloyd, Sandstede, Avitabile and Champneys [56], who investigated stationary spatially localised hexagon patterns of the two-dimensional Swift-Hohenberg equation using a spectral approach. McSloy, Firth, Harkness and Oppo [62] employed a similar approach very successfully to compute and continue hexagonal patches for the Ginzburg-Landau equation with a saturable nonlinearity in the context of nonlinear optics.

We also remark that, in a more general setting, Cabral and Rosa [22] employed Fourier numerical analysis in a similar manner: they used a Fourier pseudo-spectral method for case, spatial discretisation and a first order implicit scheme in time to discover a period-doubling cascade of periodic solu-

Appendix A: Eigenvalues of the soliton ψ_-

tions in a damped and forced version of the Korte-de Vries equation. And more recently Ambrose and Wilkening [3] presented a method for finding time-periodic solutions of nonlinear PDEs based on minimizing a functional. All these recent numerical algorithms underline an active research interest in nonlinear numerical methods and in spectral methods in particular.

1.2 The directly driven NLS

As mentioned in §1.1 we can also pump energy into the damped nonlinear Schrödinger equation (1.1) through a *direct driving* term. In this case the corresponding amplitude equation is

$$i\Psi_t + \Psi_{xx} + 2|\Psi|^2\Psi = -he^{i\Omega t} - i\gamma\Psi. \tag{1.12}$$

Importantly, equation (1.12) is the small-amplitude limit of the ac-driven damped sine-Gordon system,

$$\theta_{tt} + \alpha\theta_t - \theta_{xx} + \sin\theta = \Gamma\cos(\omega t). \tag{1.13}$$

Both systems have numerous applications in a variety of fields, including plasma and condensed matter physics, nonlinear optics and superconducting electronics. In particular, Barashenkov and Zemlyanaya [13] offer a physical discussion of equation (1.12) as the small-amplitude limit model of a strongly coupled pendulum array with horizontal sinusoidal driving. For further specific applications the interested reader is referred to [7, 9, 13] and references therein.

In a similar manner to the parametrically driven NLS, we note that if $\Psi(x,t)$ is a solution to equation (1.12) corresponding to the parameters h, γ, and Ω, then $\widetilde{\Psi}(x,t) = k\Psi(kx, k^2t)$ is the solution corresponding to $\widetilde{h} = k^3h$, $\widetilde{\Omega} = k^2\Omega$, and $\widetilde{\gamma} = k^2\gamma$. Thus only two of the three parameters h, γ, and Ω, are significant and we can always fix the third parameter [6, 78]. Using this freedom we choose to set Ω to unity. Substituting $\Psi(x,t) = e^{it}\psi(x,t)$ in and simplifying, transforms equation (1.12) into autonomous form:

$$i\psi_t + \psi_{xx} + 2|\psi|^2\psi - \psi = -h - i\gamma\psi. \tag{1.14}$$

Equation (1.14) is the representation of the directly driven NLS we shall be using in this dissertation.

Two stationary soliton solutions of the directly driven NLS (1.14) for $\gamma = 0$ are known explicitly [6]:

$$\psi_\pm(x) = \psi_0\left[1 + \frac{2\sinh^2\beta}{1 \pm \cosh\beta\cosh(Ax)}\right], \tag{1.15}$$

where the parameter β is in one-to-one correspondence with the driving strength h,

$$h = \frac{\sqrt{2}\cosh^2\beta}{(1 + 2\cosh^2\beta)^{3/2}}. \tag{1.16}$$

The domain of existence of these two *undamped* solitons is defined over the range $0 \leq h \leq 0.272$; these values are traced out as β decreases from infinity to zero. The asymptotic value ψ_0 and the inverse width A are also expressible through β:

$$\psi_0 = \frac{1}{\sqrt{2}} \frac{1}{\sqrt{1 + 2\cosh^2 \beta}}, \quad A = \frac{\sqrt{2}\sinh \beta}{\sqrt{1 + 2\cosh^2 \beta}}. \tag{1.17}$$

The stability properties of the $\psi_\pm$ (undamped) solitons have been thoroughly studied by [6]. The ψ_+ soliton is unstable for all h for which it exists, while the ψ_- soliton is stable for $0 \leq h < h_{\text{Hopf}}$ and unstable for $0.272 \geq h \geq h_{\text{Hopf}}$, where $h_{\text{Hopf}} = 0.077$ is the point of Hopf bifurcation. The undamped stationary solitons can also form a variety of stationary soliton complexes [13].

When damping is added to the directly driven NLS (1.14), no exact solutions are available. Nevertheless, analogues of the ψ_+ and ψ_- solitons exist which we can study numerically. As in the undamped case, these damped stationary solitons can form a variety of multi-soliton complexes [8, 23, 52].

Another important class of solutions of the directly driven NLS are the solutions that form the background of the stationary soliton solutions. These solutions are called flat-locked solutions because that are constant in space ($\Psi_{xx} = 0$) and are locked to the driver's frequency ($\Psi(x,t) = \psi_0 e^{it}$). The stability properties of the flat-locked solutions impose strict limitations on the domain of existence of the stationary solitons. Coupling an analytical study of the flat-locked solutions with numerical results, Barashenkov and Smirnov [7] were able to construct the existence and stability chart for the stationary solitons of the directly driven NLS as a function of the forcing amplitude h and the damping coefficient γ. This chart is reproduced in Figure 1.3 and below we summarise the existence and stability boundaries briefly. The interested reader is referred to [7] for full details.

For fixed γ, no localised solutions are possible for $h < h_{\text{thr}}$, where the threshold driving strength (the lower existence boundary) is given to good accuracy by

$$h_{\text{thr}} = \frac{2}{\pi}\gamma. \tag{1.18}$$

This result was first obtained by Kaup and Newell [50] through inverse scattering-based perturbation theory, and has been reproduced by expanding ψ_- in a perturbation series in powers of small h and γ [76, 78]. Through numerical study Barashenkov and Smirnov [7] found that equation (1.18) was unexpectedly accurate with the deviation of actual h_{thr} being very small for $\gamma \leq 1/2$ and reasonably small for $\gamma \geq 1/2$. This phenomenon was later explored by Barashenkov and Zemlyanaya [9], who evaluated the next order in the expansion of h_{thr} to show that the reason for the accuracy of the

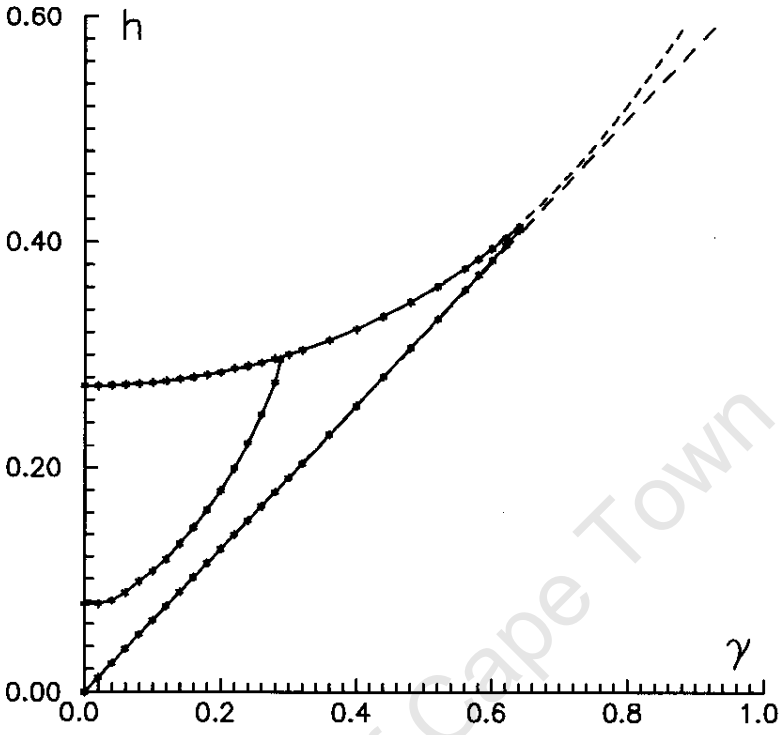

Figure 1.3: Existence and stability chart for the directly driven NLS stationary solitons, reproduced from [7]. The upper and lower solid lines demarcate the boundaries of the soliton's existence domain. The middle solid line is the line of the Hopf bifurcation; the ψ_- soliton is stable (unstable) below (above) this line. The upper and lower dashed lines mark the boundaries where the flat-locked solution is stable.

first order approximation was that the next-order coefficient is anomalously small: $h_{\rm thr} = (2/\pi)\gamma + 0.002\gamma^3$.

The upper existence boundary, marked by the solid and dashed upper line in Figure 1.3, is more complicated and was constructed by separate analysis of three typical regions dependent on γ. In summary, the upper dashed line, which is given by

$$h(\gamma) = \begin{cases} h_+(\gamma), & \gamma \leq 1/2, \\ h_*(\gamma), & \gamma > 1/2, \end{cases} \tag{1.19}$$

where

$$h_+(\gamma) \equiv \left\{ \frac{1}{3}\left(\gamma^2 + \frac{1}{9}\right) + \frac{1}{3}\sqrt{\frac{1}{3}\left(\frac{1}{3} - \gamma^2\right)^3} \right\}^{1/2},$$

and

$$h_*(\gamma) \equiv \sqrt{\gamma^3 - \gamma^2 + \gamma/2},$$

demarcates the upper boundary of the domain of existence of the ψ_+ soliton. The upper solid line outlines the upper boundary for the ψ_- soliton's domain of existence. For $\gamma < 1/2$, this boundary is given by equation (1.19), but as γ increases above $1/2$ it begins to deviate from equation (1.19) and must be determined numerically.

In between the upper and lower existence boundaries the ψ_+ and ψ_- solitons coexist. While ψ_+ soliton is unstable for all h and γ, the stability properties of the ψ_- soliton depend on whether γ is greater or smaller than $\gamma_{\rm cr}$, where $\gamma_{\rm cr} \approx 0.3$ [7]. When $\gamma > \gamma_{\rm cr}$, the ψ_- soliton is stable for all h, whereas for $\gamma < \gamma_{\rm cr}$, the ψ_- soliton is stable for small h and loses stability via a Hopf bifurcation as h is increased.

All of the aforementioned stability results of the ψ_- soliton apply to solutions that live on the *infinite* line and it is important to bear in mind that these stability properties will be affected by shortening the length of the spatial interval. Barashenkov and Smirnov [7] highlighted this when they showed that previously observed [78] "stability windows" of the ψ_- soliton occurred only when the directly driven NLS was considered on a small finite interval but not on larger intervals.

An open question about the directly driven NLS stationary solitons is whether the extent of their domain of existence (in (h, γ) parameter space) is infinite or not. In the case of the parametric driving, the stationary solitons exist for all γ within the infinite wedge $\gamma \leq h \leq h_{\rm cont}$. However we have no corresponding analytical result for the directly driven NLS stationary solitons for nonzero γ. In §6.1, through numerical continuation of the stationary ψ_- soliton in h and γ, we find that, within numerical accuracy, the domain of existence is in fact finite.

The primary numerical tool employed in many of the studies referenced in this section was numerical continuation. More specifically, all of the existence and stability results of the stationary solitons of the directly driven NLS were confirmed, or in fact originally obtained, using a finite difference numerical continuation scheme similar to that implemented in studies of the parametrically driven NLS soliton solutions; the full details are given in [7]. However, to our knowledge, numerical continuation has not yet been employed to investigate the *time-periodic* soliton solutions of the directly driven NLS. For insight into the attractor chart of these solutions we turn to Spatschek, Pietsch, Laedke and Eickermann [76]. They constructed the attractor chart reproduced in Figure 1.4 using direct numerical simulation. Our study of the temporally periodic directly driven NLS soliton solutions will be largely concerned with refining their chart.

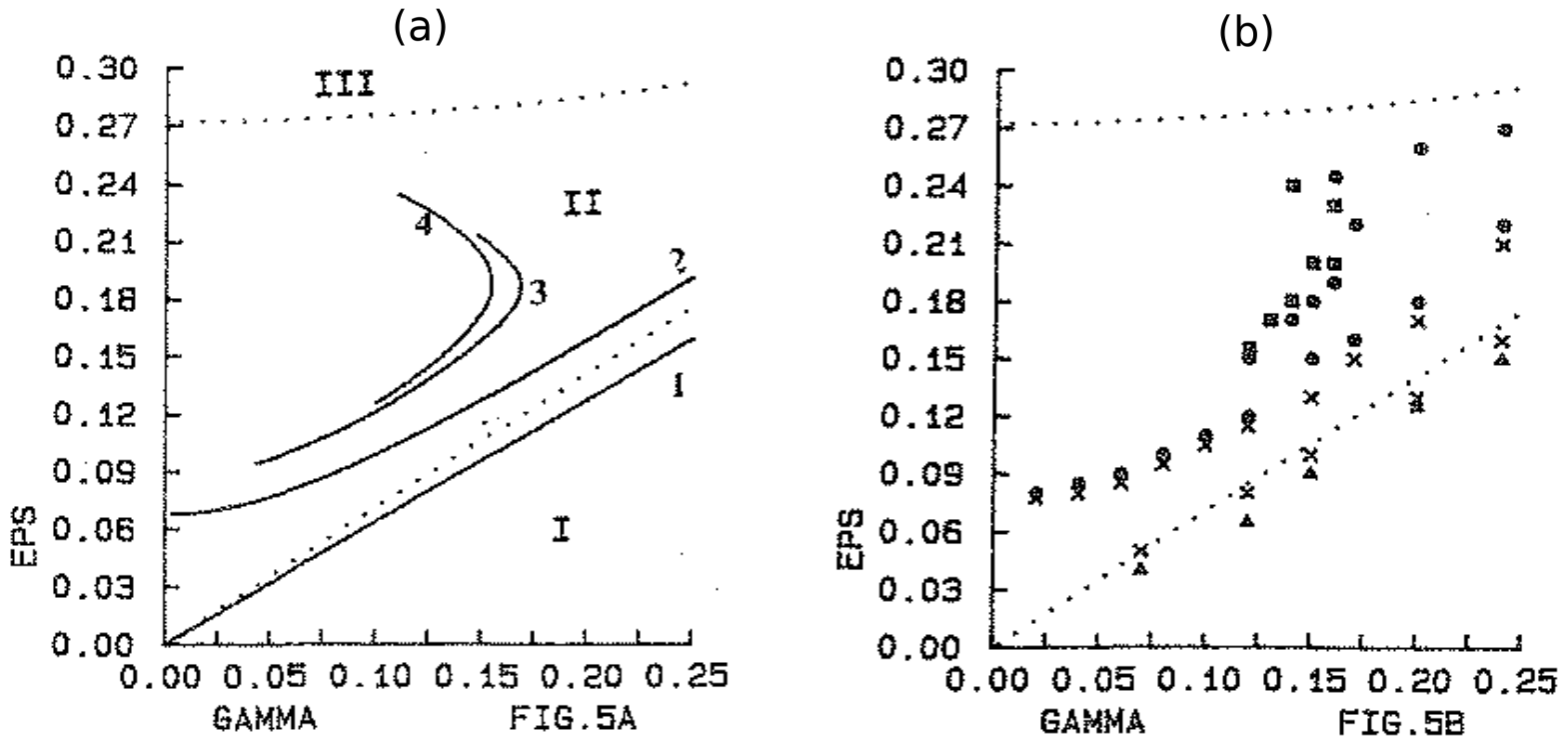

Figure 1.4: Attractor chart for the directly driven NLS reproduced from [76]. Here EPS$\equiv h$ and GAMMA$\equiv \gamma$. The dotted lines separate the regions where one or three flat solutions exist. (a) Bifurcation set computed from reduced ODE system obtained from the directly driven NLS using an (approximate) variational approach [76]: below line 1 only flat solutions exist; below line 2 we find the stable stationary ψ_- soliton; temporally periodic solitons exist outside line 3; outside line 4 period two soliton solutions exist; and inside line 4 higher period solitons and chaotic states are found. (b) Points obtained from direct numerical simulation of the directly driven NLS: triangles indicate flat-locked solutions; crosses the stable stationary ψ_- solitons; circles period-one periodic solitons; squares higher order periodic or temporal chaotic states.

Chapter 2

Preliminary Theory

In this chapter we recall some theorems pertaining to orbits homoclinic to saddle-focus fixed points which will help us understand the results of the periodic parametrically driven NLS solitons collected in Chapter 5. These theorems, originally due to Shil'nikov [74, 75], describe the behaviour of three- and n-dimensional systems near bifurcations of homoclinic orbits to hyperbolic equilibria.

We begin by introducing the homoclinic bifurcation before giving a sketch proof of Shil'nikov's theorem for orbits homoclinic to saddle-foci in 3 dimensional systems. We go on to thoroughly discuss the dynamics near the homoclinic orbit through the study of an explicit form for the Poincaré return map in a 3-dimensional system. Finally, we conclude this chapter by showing that, under the appropriate conditions, the study of the (generic) n-dimensional case can be reduced to the considered three-dimensional case.

Throughout this section we have emphasized understanding over rigour. That said, we assume that the reader is familiar with the fundamental notions of topological equivalence, homoclinic orbits and standard one-parameter bifurcations. Excellent introductions to these concepts and applied bifurcation theory in general can be found in the textbooks by Kuznetsov [53] and Guickenheimer and Holmes [41]. Indeed, much of the work included in this chapter is adapted from the treatment of homoclinic bifurcations given in [53]. A thorough and more detailed survey of homoclinic bifurcation literature can be found in [47].

2.1 Homoclinic bifurcations

We will be concerned with the continuous-time dynamical system defined by a system of ODEs:

$$\dot{x} = f(x, \alpha), \quad x = (x_1, x_2, \ldots, x_n)^T \in \mathbb{R}^n, \ \alpha \in \mathbb{R}, \tag{2.1}$$

where f is smooth and α is a control parameter. For definiteness, assume that $h(t)$ is a homoclinic orbit of (2.1) for $\alpha = 0$, which tends to the equilibrium x_0 as $t \to \pm\infty$.

A key assumption often imposed when considering homoclinic bifurcations is that the equilibrium x_0 itself does not undergo a local bifurcation at $\alpha = 0$. A sufficient condition for this assumption is the hyperbolicity of x_0: we refer to an equilibrium x_0 as hyperbolic if there are no eigenvalues of the Jacobian matrix f_x evaluated at the equilibrium point x_0 on the imaginary axis.

Keeping with tradition, we state all relevant results and theorems in this chapter under the assumption of the hyperbolicity of x_0. However, it is important to note that the hyperbolicity of x_0 is only a *sufficient* condition and not a *necessary* condition. This distinction will be key in analysing our numerical results for the parametrically driven NLS in §5.2. There the stationary ψ_- soliton (1.4) will play the role of the equilibrium x_0. As discussed in §1.1 the ψ_- soliton possesses a zero mode and is therefore clearly not hyperbolic. However, because this mode persists as long as the solution itself is defined, we are assured that the ψ_- soliton does not undergo any local bifurcation near the homoclinic bifurcation.

Another important general assumption we will impose is that the systems we study are *generic*. We describe a system as "generic" if the system satisfies a finite number of *genericity conditions*. These genericity conditions take the form of nonequalities:

$$N_i[f] \neq 0, \quad i = 1, 2, \ldots, s,$$

where each N_i is a function of the partial derivatives of $f(x, \alpha)$ evaluated at the equilibrium and bifurcation points. Intuitively, we expect a "typical" parameter-dependent system to satisfy these conditions. Otherwise put, a system which does not satisfy these genericity conditions is unusual or exceptional.

Finally, we define the stable and unstable manifolds of a hyperbolic equilibrium x_0 by

$$W^s(x_0, 0) = \{u(0); u(t) \text{ satisfies (2.1) and } u(t) \to x_0 \text{ as } t \to \infty\}$$
$$W^u(x_0, 0) = \{u(0); u(t) \text{ satisfies (2.1) and } u(t) \to x_0 \text{ as } t \to -\infty\}.$$

With this preamble established let us now introduce precisely the homoclinic bifurcation.

Consider the case $n = 3$ in system (2.1): Assume then, that we have a system in $\mathbb{R}^3$ with a homoclinic orbit Γ_0 to a saddle fixed point x_0 as shown in the central image of Figure 2.1. We may further assume that $\dim W^u = 1$ (otherwise simply reverse the time direction). If we introduce a two-dimensional local cross-section Σ near the saddle as in Figure 2.1, we can select coordinates (ξ, η) along Σ such that the point of the intersection

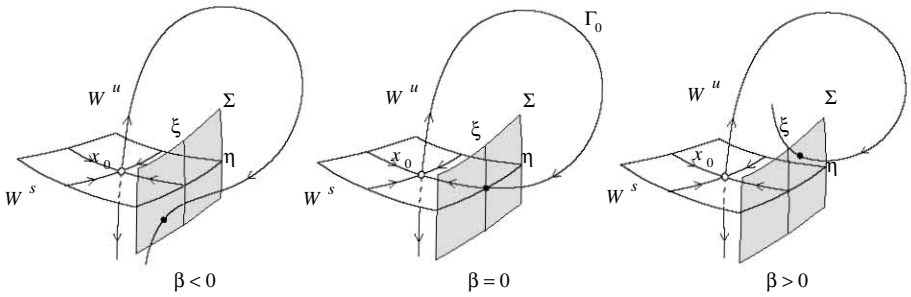

FIGURE 6.5. Split function in the case $n = 3$.

Figure 2.1: Split function in the case $n = 3$. Figure taken from [53].

has a homoclinic orbit to a saddle, then the system

$$\begin{cases} \dot{x}_1 &= f_1(x_1, x_2) - \alpha f_2(x_1, x_2), \\ \dot{x}_2 &= \alpha f_1(x_1, x_2) + f_2(x_1, x_2), \end{cases} \tag{6.3}$$

with the stable manifold W^s corresponds to $\xi = 0$. Under a generic C^1-perturbation, or equivalently by varying the control parameter α, the unstable manifold W^u does not return to the saddle and will intersect Σ at some $(\xi, \eta) \neq 0$. Two possibilities for W^u missing the saddle are illustrated in Figure 2.1. Denote by (ξ^u, η^u) the point of the intersection of the unstable manifold W^u_{α} with Σ. Then we can define the following (vector) function which serves as a notational and geometrical convenience

Definition 2.1. *$\beta := (\xi^u, \eta^u)$ is called the split function.*

The zero of the split function, $\beta = 0$, is precisely the bifurcation condition for the homoclinic bifurcation in $\mathbb{R}^3$.

2.2 Shil'nikov's theorem for orbits homoclinic to a saddle-focus equilibrium

In the planar case ($n = 2$) any homoclinic orbit must be bi-asymptotic to a *saddle* equilibrium. Moreover in this case, the homoclinic bifurcation is fully characterised by the Andronov and Leontovich Theorem [4].

In three dimensions a wider variety hyperbolic equilibria allowing for homoclinic orbits are possible and therefore a wider variety of homoclinic bifurcations can be considered. We will limit our study to the saddle-focus case. Specifically, we assume that the particular hyperbolic equilibrium is a saddle-focus and further, without loss of generality, that it has a one-dimensional unstable manifold W^u (with eigenvalue $\lambda_1 > 0$) and a two-dimensional stable manifold W^s (with eigenvalues $\lambda_{2,3} = \lambda^*$ and $\mathrm{Re}\lambda_{2,3} < 0$).

The ratio of the real parts of the stable and unstable eigenvalues is important enough to warrant a definition.

Definition 2.2. *The saddle quantity δ of a saddle-focus is defined as*

$$\delta = -\frac{\mathrm{Re}\lambda_{2,3}}{\lambda_1}. \tag{2.2}$$

Case $n = 3$. It is also possible to define a split function in this case. Consider a system in $\mathbb{R}^3$ with a homoclinic orbit Γ_0 to a saddle x_0. Assume that $\dim W^u = 1$ (otherwise, reverse the time direction), and introduce a two-dimensional cross-section Σ with coordinates (ξ, η) as in Figure 6.5. Suppose that $\xi = 0$ corresponds to the intersection of Σ with the stable manifold W^s of x_0. As before, this can be done for all sufficiently close systems. Let the point (ξ^u, η^u) correspond to the intersection of W^u with Σ. Then, a split function can be defined as in the planar case before: $\beta = \xi^u$. Its zero

$$\beta = 0$$

gives a condition for the homoclinic bifurcation in $\mathbb{R}^3$.

Remarks:

(1) The preceding cases are examples of nontransversal intersections of the invariant manifolds W^u and W^s. One can construct a three-dimensional system with a structurally stable *heteroclinic* orbit connecting two saddles. This orbit must be a transversal intersection of the corresponding *two-dimensional* stable and unstable manifolds.

(2) There are similar results for dynamical systems with the saddle-focus case for which the presence of a nontransversal homoclinic orbit is generic. ♢

Thus, we have found that under certain conditions the presence of a homo-/hetero-clinic orbit Γ_0 to a saddle/saddles implies a bifurcation. Our

Theorem 2.3. (Shil'nikov [74]) *Suppose that a three-dimensional system*

$$\dot{x} = f(x, \alpha), \quad x \in \mathbb{R}^3, \ \alpha \in \mathbb{R}, \tag{2.3}$$

with smooth f, has at $\alpha = 0$ a saddle-focus equilibrium point $x_0 = 0$ with eigenvalues $\lambda_1(0) > 0 > \mathrm{Re}\lambda_{2,3}(0)$ and a homoclinic orbit Γ_0. Assume that the following genericity conditions hold:

(H.1) $\delta_0 = -\mathrm{Re}\lambda_{2,3}(0)/\lambda_1(0) < 1$*;*

(H.2) $\lambda_2(0) \neq \lambda_3(0)$.

Then, system (2.3) *has an infinite number of saddle limit cycles in a neighbourhood U_0 of $\Gamma_0 \cup x_0$ for all sufficiently small $|\beta|$.*

Sketch Proof of Theorem: An outline of the proof is instructive. We follow the sketch proof given in Kuznetsov [53]; for full details the interested reader is referred to [81].

We can select a coordinate system in which the stable and unstable manifolds, $W^s(x_0)$ and $W^u(x_0)$ respectively, are locally linear in some neighbourhood of the equilibrium x_0. Moreover, we can choose coordinates such that $W^s(x_0)$ is locally the plane $x_1 = 0$, while $W^u(x_0)$ is locally the line $x_2 = x_3 = 0$ (the situation is illustrated in Figure 2.2). Introduce two rectangular two-dimensional cross-sections $\Sigma \subset \{x_2 = \epsilon_2\}$ and $\Pi \subset \{x_1 = \epsilon_1\}$, where $\epsilon_{1,2}$ are small and chosen such that the homoclinic orbit Γ_0 intersects both cross sections as shown in Figure 2.2. We next define a Poincaré return map $P : \Sigma^+ \to \Sigma$ along the orbits of system (2.3) where Σ^+ is the upper part of Σ with $x_1 \geq 0$. We can then represent P as a superposition of maps:

$$P = Q \circ \Delta,$$

where $\Delta : \Sigma^+ \to \Pi$ and $Q : \Pi \to \Sigma$ map near the saddle-node and along the global part of Γ_0 respectively. This construction can be carried out for all sufficiently small $|\beta|$.

Bearing in mind the flow on the unstable manifold, we find that the image of Σ^+ under the action of the map Δ, $\Delta\Sigma^+$, looks like a solid spiral, sometimes referred to as the *Shil'nikov snake* (note that we are free to choose the cross-sections Σ and Π such that we have $\Delta\Sigma^+ \subset \Pi$ provided $|\beta|$ is sufficiently small). The global map Q maps this "snake" back into the plane containing Σ.

Let us first assume that $\beta = 0$ and consider the intersection of the "snake" image, $P\Sigma^+$, with the local cross-section Σ as shown in Figure 2.3. The origin of the "snake" is at the intersection of Γ_0 with Σ. The intersection of Σ with $W^s(x_0)$ splits the "snake" into an infinite number of upper and lower "half-spirals". The preimages Σ_i of the upper "half-spirals" $P\Sigma_i$, with $i = 1, 2, \ldots$, are horizontal strips in Σ^+. The intersection $\Sigma_i \cap P\Sigma_i$

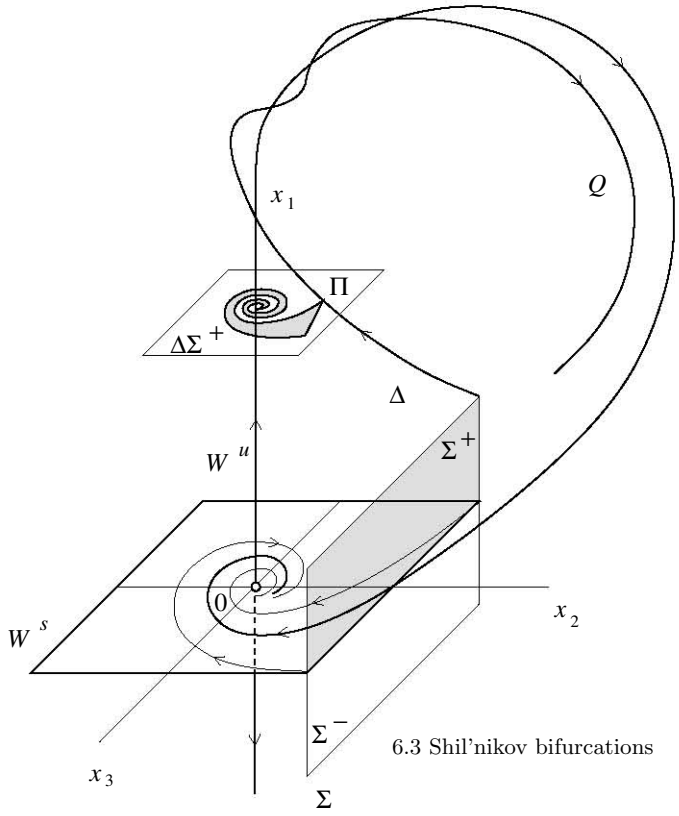

FIGURE 6.32. Construction of the Poincaré map in the saddle-focus case.

Figure 2.2: Construction of the Poincaré map. Figure taken from [53].

logically equivalent. The reason is the same: the topological invariance of ν_0 given by (6.15). Actually, the complete topological structure of the phase portrait near the homoclinic orbit is not known, although some substantial information is available due to Shil'nikov. Let $\tilde{\Omega}(\nu)$ be the set of all nonequivalent bi-infinite sequences

$$\omega = \{\ldots, \omega_{-2}, \omega_{-1}, \omega_0, \omega_1, \omega_2, \ldots\},$$

where ω_i are nonnegative integers such that

$$\omega_{i+1} \leq \nu\omega_i$$

for all $i = 0, \pm 1, \pm 2, \ldots$, and for some real number $\nu > 0$. Then, at $\beta = 0$ there is a subset of orbits of (6.17) located in a neighborhood U_0 of $\Gamma_0 \cup x_0$ for all $t \in \mathbb{R}^1$, whose elements are in one-to-one correspondence with $\tilde{\Omega}(\nu)$, where ν does not exceed the topological invariant ν_0. The value ω_i can be viewed as the number of "small" rotations made by the orbit near the saddle after the ith "global" turn.

(2) As β approaches zero taking positive or negative values, an *infinite* number of bifurcations results. Some of these bifurcations are related to a "basic" limit cycle, which makes one global turn along the homoclinic

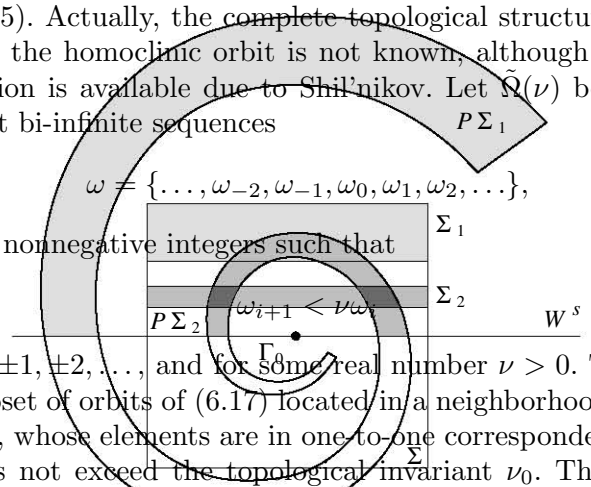

Figure 2.3: Poincaré map structure for $\delta < 1$. Figure taken from [53].

is nonempty and consists of two components for $i \geq i_0$, where i_0 is some positive integer. Although we will not do so here, it can be checked [41] that the necessary conditions are satisfied and that each of these intersections forms a Smale horseshoe. Each horseshoe gives a infinite number of saddle fixed points for the map P and thus system (2.3) has an infinite number of saddle limit cycles for $\beta = 0$.

If $\beta \neq 0$, the origin of the "snake" is displaced from the horizontal line in Σ (shifted up or down). Therefore there remains only finitely many Smale horseshoes. Nevertheless, each horseshoe still gives an infinite number of saddle fixed points for P and therefore an infinite number of saddle limit cycles for system (2.3) for sufficiently small $|\beta|$. □

2.3 Study of explicit Poincaré return map

We now have an intuitive idea of the dynamics near the homoclinic orbit and saddle-focus of system (2.3). However, the dynamics are in fact even richer than Theorem 2.3 leads us to believe. Indeed, as β approaches zero taking on both positive and negative values, an infinite number of bifurcations occur. To properly understand this phenomenon we need an explicit form for the Poincaré return map P. Such a construction and analysis has been carried out by Glendinning and Sparrow [40] who perform a study of the local and global behaviour near homoclinic orbits to fixed points of the saddle-focus type. Their construction is very similar to the Poincaré map P which we have described above, except that they choose the cross-section Σ to be perpendicular to the stable manifold $W^s(x_0)$. The situation is illustrated in Figure 2.4.

In cylindrical coordinates for $z \ll 1$ the Poincaré map takes the form [40]

$$P_\alpha(r, z) = \Big(\tilde{r} + a\alpha + brz^\delta \cos(\xi \ln z + \Phi_1), \\ \alpha + cz^\delta \cos(\xi \ln z + \Phi_2)\Big), \tag{2.4}$$

where $\tilde{r}$ is the intersection of the homoclinic orbit Γ_0 with the cross-section Σ, $a,\ b,\ c,\ \xi$, and $\Phi_{1,2}$ are constants, and $\delta \equiv \delta_0$ is the saddle quantity (2.2) (we have set $\delta \equiv \delta_0$ for the sake of brevity).* The angular coordinate, θ, has been dropped on account of being zero. As we did in the previous section we will confine our attention to the case with $\delta < 1$ as this is the situation relevant to our results in §5.2.

To determine the fixed points of the Poincaré map (2.4) and hence the periodic orbits of system (2.3), we set the left and right sides of equation (2.4) equal to obtain for the radial coordinate r,

$$r = \frac{\tilde{r} + a\alpha}{1 - bz^\delta \cos(\xi \ln z + \Phi_1)}. \tag{2.5}$$

*For notes on the validity and domain of applicability of the Poincaré map (2.4) see [40].

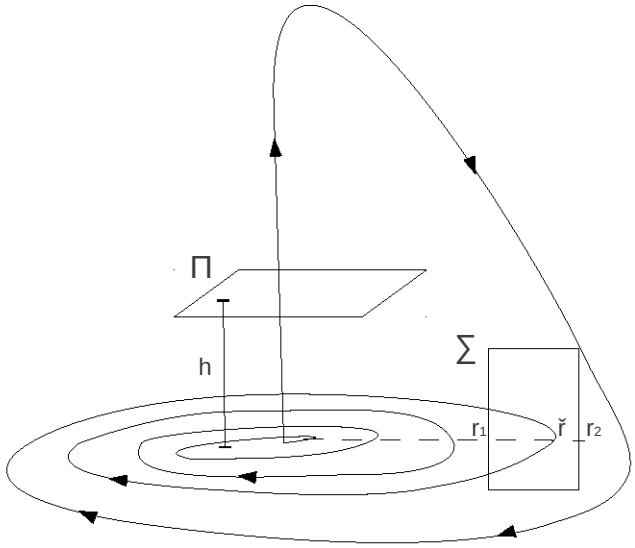

Figure 2.4: Construction of the Poincaré map, illustrated at $\alpha = 0$. Surface Π is parallel to the stable manifold and a distance h above it. Surface Σ is perpendicular to the stable manifold and the stable manifold strikes it a distance $\tilde{r}$ from the fixed point. Moreover, Σ is chosen such that each trajectory strikes it only once as it spirals into the stationary point.

Substituting (2.5) into the equation for the z coordinate we find

$$(z-\alpha)\left(1 - bz^{\delta} cos(\xi \ln z + \Phi_1)\right) = (\tilde{r} + a\alpha)cz^{\delta} \cos(\xi \ln z + \Phi_2). \qquad (2.6)$$

Restricting our attention to the region $z \ll 1$, the left side of (2.6) simplifies to approximately $z - \alpha$. The intersection of the two curves representing the left and right sides of equation (2.6) then give the z values of the fixed points of the Poincaré map (2.4) for $z \ll 1$; representative examples for three cases for the considered regime $\delta < 1$ are shown in Figure 2.5.

From Figure 2.5 we can deduce the following:

- $\alpha < 0$. There is a finite number of intersections of the two curves representing a finite number of periodic orbits of system (2.3).
- $\alpha = 0$. There is a countable infinity of intersections representing a countable infinity of periodic orbits of system (2.3).
- $\alpha > 0$. A finite number of intersections of the two curves exists and therefore system (2.3) has a finite number of periodic orbits.

The above summary is well illustrated by the dependency of the period on the parameter α. To determine this dependency we first observe, from

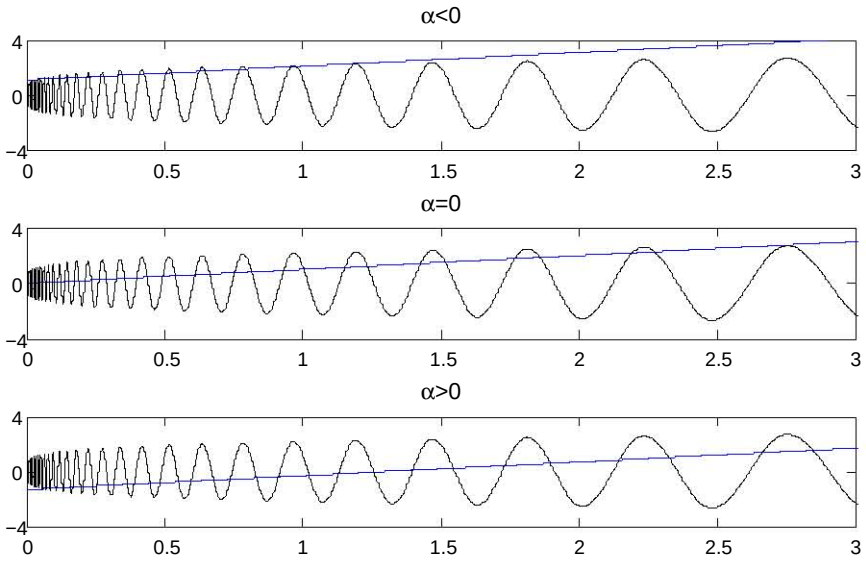

Figure 2.5: The curves $z - \alpha$ (blue) and $cz^{\delta}\cos(\xi \ln z + \Phi_2)$ (black) for $\delta < 1$ and various values of α. Intersections of the curves give the z coordinate of the fixed points of the Poincaré map (2.4) for $z \ll 1$.

Figure 2.4, that in cylindrical coordinates the flow along the z coordinate in the linear region ($z \ll 1$) is given by

$$\dot{z} = \lambda_1 z,$$

which has solution

$$z(t) = z_0 e^{\lambda_1 t}.$$

Thus, provided $z_0 > 0$, the time T taken for a trajectory starting on the cross-section Σ at $(r_0, 0, z_0)$ to strike Π is

$$T = \ln\left(\frac{h}{z_0}\right)/\lambda_1. \tag{2.7}$$

Hence, on the assumption that the time of return along the global part of Γ_0 from Π to Σ is approximately constant, periodic orbits corresponding to fixed points of the Poincaré map (2.4) with smaller z coordinates have longer periods. Noting the qualitative structure of the curve of the right hand side of (2.6), viz. $cz^{\delta}\cos(\xi \ln z + \Phi_2)$, as illustrated in Figure 2.5, we can qualitatively construct the bifurcation diagram with the period plotted as a function of the parameter α as shown in Figure 2.6. The results of Glendinning and Sparrow's [40] stability analysis of the fixed points of the Poincaré map (2.4), are included in the figure.

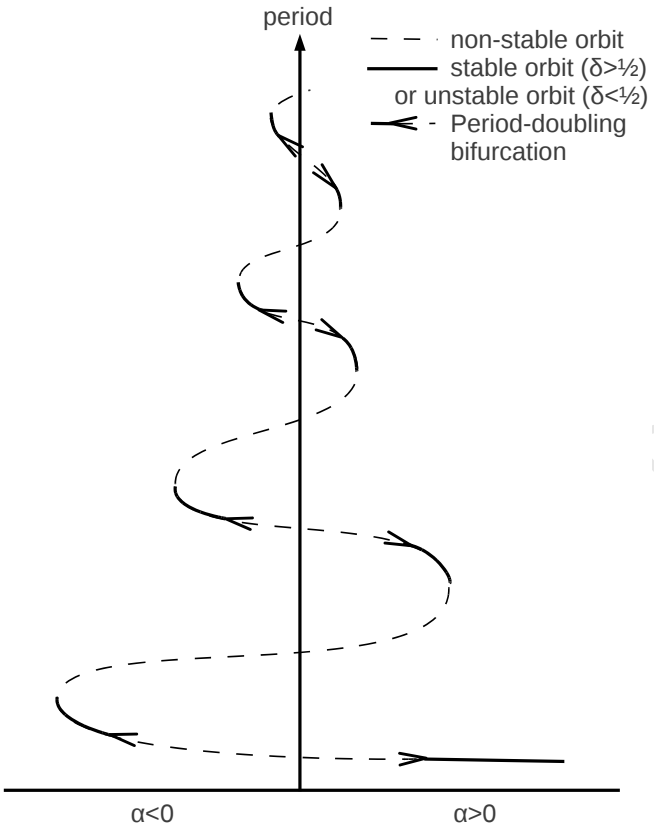

Figure 2.6: Bifurcation curve giving the period of the orbit as a function of the control parameter α for the case $\delta < 1$. Glendinning and Sparrow [40] note that, in the case studies they investigate, the stable/unstable sections of the curve are very short.

As we vary α, we encounter turning points on bifurcation curve, at each of which a pair of periodic orbits appears or disappears. Each of these turning points represent a saddle-node bifurcation. These saddle-node bifurcations produce or destroy either a stable/saddle pair of orbits or an unstable/saddle pair of orbits. Glendinning and Sparrow's analysis reveals that the former is the case when $1 > \delta > 1/2$ and the latter is the case when $\delta < 1/2$. Moreover, a careful study reveals that at each saddle-node bifurcation: the lower period orbit is either stable ($1 > \delta > 1/2$) or unstable ($\delta < 1/2$) while the higher period solution is of the saddle type; the periodic solution loses stability/unstability above the saddle-node bifurcation in a period-doubling bifurcation; finally regaining stability/unstability through a reverse period-doubling bifurcation before arriving at the next saddle-node bifurcation.

Through direct numerical simulation, Glendinning and Sparrow [40] ob-

served exactly these homoclinic dynamics in a number of ODE systems, including the Lorenz equations. They also hypothesised that such dynamics should persist in PDEs and indeed Knobloch, Moore, Toomre and Weiss [51] offer a careful study of such a homoclinic "explosion" in a PDE system, again using direct numerical simulation. However, to our knowledge no study has explicitly observed the homoclinic dynamics in PDEs using numerical continuation, and as a result all descriptions of such dynamics in PDEs have inevitably been somewhat qualitative. Thus our results in Chapter 5 are of great interest in the context of the parametrically driven NLS but also in nonlinear systems theory in general.

To study homoclinic dynamics in PDEs we need to understand how to apply the theory discussed in this and the preceding sections to n-dimensional systems. Before turning to this topic in the next section, we close our discussion about homoclinic orbits with a brief remark about other bifurcations that may occur near the (principal) homoclinic orbit.

These additional bifurcations are due to secondary or subsidiary homoclinic orbits, which make one or more close encounters with the stationary point and pass off without homoclinicity being achieved, before eventually arriving back in the linear region of our analysis and spiralling back into the stationary point. The simplest possible subsidiary homoclinic orbits, which make one unsuccessful encounter with the stationary point before achieving homoclinicity, are termed "double pulse" solutions and have been studied in detail in the literature [35, 36, 42].

2.4 Homoclinic Center Manifold Theorem

Sandstede [72, 73] and Homburg [46] proved that there exists a parameter-dependent invariant center manifold near homoclinic bifurcations. The existence of this center manifold implies that we can reduce the study of generic bifurcations of orbits homoclinic to a saddle-focus equilibria in an n-dimensional system with $n > 3$ to that of the three-dimensional case.

We again consider the system

$$\dot{x} = f(x, \alpha), \quad x = (x_1, x_2, \ldots, x_n)^T \in \mathbb{R}^n, \ \alpha \in \mathbb{R}^1, \tag{2.8}$$

where f is C^∞ smooth and $n \geq 3$. Suppose that system (2.8) has a hyperbolic equilibrium x_0 at $\alpha = 0$, and that the Jacobian matrix at x_0, $A_0 = f_x(x_0, 0)$, has n_+ eigenvalues with positive real parts and n_- eigenvalues with negative real parts. Assume further that system (2.8) has at $\alpha = 0$ an orbit Γ_0 homoclinic to x_0 and denote by $x_0(t)$ a solution of (2.8) corresponding to Γ_0. Because the equilibrium x_0 is hyperbolic, it persists for all sufficiently small $|\alpha|$ and has unstable and stable local invariant manifolds W^u and W^s that can be globally extended.

Definition 2.4. *The eigenvalues with positive (negative) real part that are closest to the imaginary axis are called the unstable (stable) leading eigenvalues, while the corresponding eigenspaces are called the unstable (stable) leading eigenspaces.*

Definition 2.5. *The stable and unstable leading eigenvalues together are called the central eigenvalues, while the corresponding eigenspace is called the central eigenspace.*

Almost all orbits on W^u (W^s) tend to the equilibrium as $t \to -\infty$ ($t \to \infty$) along the corresponding leading eigenspace, which we shall denote by T^u (T^s). Orbits which lie on the eigenspace T^{uu} (T^{ss}) corresponding to the nonleading eigenvalues form a nonleading manifold W^{uu} (W^{ss}). The final eigenspace of interest, introduced above, is the central eigenspace T^c, which is the direct sum of the stable and unstable leading eigenspaces: $T^c = T^u \oplus T^s$.

Provided both nonleading eigenspaces are nonempty, is useful to introduce the following two real numbers:

$$g^s = \frac{\mathrm{Re}\lambda_{s_1}}{\mathrm{Re}\lambda_s}, \quad g^u = \frac{\mathrm{Re}\lambda_{u_1}}{\mathrm{Re}\lambda_u},$$

where λ_s (λ_u) are the leading stable (unstable) eigenvalues and λ_{s_1} (λ_{u_1}) are the nonleading stable (unstable) eigenvalues with the smallest real part in absolute value. g^s and g^u therefore serve as a measure of the relative gaps between the corresponding nonleading and leading eigenvalues. If one of the nonleading eigenspaces is empty, we formally set $g^s = -\infty$ or $g^u = +\infty$.

Returning to system (2.8) we note that it can be recast as the extended system:

$$\begin{cases} \dot{x} = f(x, \alpha), \\ \dot{\alpha} = 0. \end{cases} \tag{2.9}$$

Let us consider the linearisation of the extended system (2.9) around the homoclinic solution $x^0(t)$ at $\alpha = 0$:

$$\begin{cases} \dot{v} = f_x(x^0(t), 0)v + f_\alpha(x^0(t), 0)\mu, \\ \dot{\mu} = 0. \end{cases} \tag{2.10}$$

Because the equation for μ in (2.10) is trivial and we can simply focus on the *variational equation* around Γ_0:

$$\dot{v} = A(t)v, \quad v \in \mathbb{R}^n, \tag{2.11}$$

where $A(t) = f_x(x^0(t), 0)$.

Now $x^0(t) \to x_0$ as $t \to \pm\infty$, so we have that

$$\lim_{t \to \pm\infty} A(t) = A_0.$$

Therefore, for $t \to \pm\infty$, solutions of (2.11) behave like solutions of the autonomous linear system

$$\dot{v} = A_0 v,$$

and we can introduce four linear subspaces of $\mathbb{R}^n$:

$$E^{uu}(t_0) = \left\{ v_0 : \lim_{t\to-\infty} \frac{v(t)}{\|v(t)\|} \in T^{uu} \right\},$$
$$E^{ss}(t_0) = \left\{ v_0 : \lim_{t\to+\infty} \frac{v(t)}{\|v(t)\|} \in T^{ss} \right\},$$
$$E^{cu}(t_0) = \left\{ v_0 : \lim_{t\to-\infty} \frac{v(t)}{\|v(t)\|} \in T^{c} \oplus T^{uu} \right\},$$
$$E^{cs}(t_0) = \left\{ v_0 : \lim_{t\to+\infty} \frac{v(t)}{\|v(t)\|} \in T^{c} \oplus T^{ss} \right\},$$

where $v(t)$ is the solution to (2.11) with the initial data $v = v_0$ at $t = t_0$. Finally, define

$$E^c(t_0) = E^{cu}(t_0) \cap E^{cs}(t_0).$$

We now formulate without proof the following theorem.

Theorem 2.6. (Homoclinic Center Manifold [73]) *Suppose that system* (2.8) *has at* $\alpha = 0$ *a hyperbolic equilibrium* $x_0 = 0$ *with a homoclinic orbit*

$$\Gamma_0 = \left\{ x \in \mathbb{R}^n : x = x^o(t), t \in \mathbb{R}^1 \right\}.$$

Assume the following conditions hold:

(H.1) $\dot{x}^0(0) \in E^c(0)$;

(H.2) $E^{uu}(0) \oplus E^c(0) \oplus E^{ss}(0) = \mathbb{R}^n$.

Then, for all sufficiently small $|\alpha|$, (2.8) *has an invariant manifold* $\mathcal{M}_\alpha$ *defined in a small neighbourhood* U_0 *of* $\Gamma_0 \cup x_0$ *and having the following properties:*

(i) $x^0(t_0) \in \mathcal{M}_0$ *and the tangent space* $T_{x^0(t_0)}\mathcal{M}_0 = E^c(t_0)$, *for all* $t_0 \in \mathbb{R}^1$;

(ii) *any solution to* (2.8) *that stays inside* U_0 *for all* $t \in \mathbb{R}^1$ *belongs to* $\mathcal{M}_\alpha$;

(iii) *each* $\mathcal{M}_\alpha$ *is* C^k *smooth, where* $k \geq 1$ *is the maximal integer number satisfying both*

$$g^s > k \quad \textit{and} \quad g^u > k.$$

Definition 2.7. *The manifold* $\mathcal{M}_\alpha$ *is called the homoclinic center manifold.*

By analogy we extend the definition of the saddle-quantity to the n-dimensional case:

Definition 2.8. *The saddle quantity δ of a hyperbolic equilibrium is the ratio of the real parts of its leading eigenvalues:*

$$\delta = -\frac{\mathrm{Re}\lambda_s}{\mathrm{Re}\lambda_u}, \tag{2.12}$$

where λ_s (λ_u) is the leading stable (unstable) eigenvalue.

We will further assume that the following nondegeneracy condition holds at $\alpha = 0$:

(H.0) *$\delta \neq 1$ and the leading eigenspaces $T^{u,s}$ are either one- or two-dimensional.*

The following theorem is a direct consequence of the application of the Homoclinic Center Manifold Theorem and Theorem 2.3.

Theorem 2.9. *For any generic one-parameter system having a saddle-focus equilibrium point x_0 with a homoclinic orbit Γ_0 at $\alpha = 0$ there exists a neighbourhood U_0 of $\Gamma_0 \cup x_0$ such that one of the following alternatives hold:*

(a) *if $\delta > 1$, a unique limit cycle L_α bifurcates from Γ_0 in U_0 as α passes through zero, and $\dim W^s(L_\alpha) = n_- + 1$;*

(b) *if $\delta < 1$, the system has an infinite number of saddle limit cycles in U_0 for all sufficiently small $|\alpha|$.*

The genericity conditions alluded to in Theorem 2.9 are the nondegeneracy conditions (H.0), (H.1) and (H.2) listed above, as well as the transversality condition:

(H.3) *the homoclinic orbit Γ_0 is regular; i.e., the intersection of the tangent spaces $T_{x^0(t)}W^s$ and $T_{x^0(t)}W^u$ at each point $x^0(t) \in \Gamma_0$ is one-dimensional and W^s and W^u split by an $O(\alpha)$ distance as α moves away from zero.*

Chapter 3

Numerical Continuation

In this chapter we give an elementary introduction to numerical continuation, the principal numerical tool used in this dissertation. We will follow the introduction given by Kuznetsov [53] and seek to familiarise the reader with numerical continuation by focusing our introduction on one-parameter bifurcation analysis and the location and continuation of equilibria and limit cycles; we will not delve into the details of the numerical methods for detection of higher dimension bifurcations nor for the continuation of two-parameter bifurcation curves.

We begin by discussing equilibrium location and introducing the Newton and Newton-chord methods. Following this, we turn to the problem of finding limit cycles and in particular introduce the orthogonal collocation discretisation method. Having discussed the location of equilibria and limit cycles were are able to introduce the basic predictor-corrector method for continuation of such phase objects and discuss the test functions used to detect bifurcations during continuation.

Throughout this section we will be concerned with the one-parameter continuous-time system,

$$\dot{x} = f(x, \alpha), \quad x \in \mathbb{R}^n, \ \alpha \in \mathbb{R}, \tag{3.1}$$

where as usual f is sufficiently smooth. For our purposes, a numerical analysis of system (3.1) will entail locating and determining the stability of its equilibria and limit cycles and studying the orbit structure near these phase objects as the control parameter α is continuously varied.

3.1 Location of equilibria

Let us first assume that the parameter α is fixed:

$$\dot{x} = f(x), \quad x \in \mathbb{R}^n. \tag{3.2}$$

We wish to determine the equilibria of the system (3.2) for this fixed α:

$$f(x) = 0, \quad x \in \mathbb{R}^n. \tag{3.3}$$

If the equilibrium we seek x^0 is stable or totally unstable, then it can be found by numerical integration of (3.2) in forward or reverse time respectively. However, typically this is not the case and we need a more general method such as Newton's method.

To apply Newton's method we first approximate the system (3.3) by its linear part. Assume first that we have an initial point $x^{(j)}$ that is close to the equilibrium x^0. The linear approximation for the equilibrium condition (3.3) near $x^{(j)}$ is

$$f(x^{(j)}) + A(x^{(j)})(x - x^{(j)}) = 0, \tag{3.4}$$

where $A(x^{(j)})$ denotes the Jacobian matrix f_x evaluated at $x^{(j)}$. If the Jacobian matrix $A(x^{(j)})$ is invertible, then the linear system (3.4) has the solution

$$x = x^{(j)} - A^{-1}(x^{(j)})f(x^{(j)}),$$

which will generally be closer to x^0 than $x^{(j)}$ as illustrated by Figure 3.1. Newton iterations are thus defined by the recurrence relation

$$x^{(j+1)} = x^{(j)} + \eta^{(j)}, \quad j = 0, 1, 2, \ldots, \tag{3.5}$$

where $x^{(0)}$ is our sufficiently close initial guess for the equilibrium x^0 and the displacement $\eta^{(j)}$ is given by the solution of the linear system,

$$A(x^{(j)})\eta^{(j)} = -f(x^{(j)}). \tag{3.6}$$

The following theorem, proved in most introductory numerical textbooks (for example [34]), justifies the use of Newton's method and tells us that the convergence is quadratic.

Theorem 3.1. *Suppose the system* (3.2) *is smooth and has an equilibrium* $x = x^0$ *with no zero eigenvalues of the Jacobian matrix* $f_x(x^0)$*. Then there is a neighbourhood* U *of* x^0 *such that the Newton iterations* (3.5), (3.6) *converge to* x^0 *from any initial point* $x^0 \in U$*. Moreover,*

$$\|x^{(j+1)} - x^0\| \leq \kappa_0 \|x^{(j)} - x^0\|^2, \quad j = 0, 1, 2, \ldots,$$

for some $\kappa_0 > 0$*, uniformly for* $x^0 \in U$*.*

The most computationally taxing part of each Newton iteration is computation of the Jacobian A, by numerical differentiation of $f(x)$. Several modifications of Newton's method have therefore been proposed to help reduce this computational expense. We discuss only the relevant modification, the Newton-chord method, which AUT0 uses in conjunction with the full Newton method.

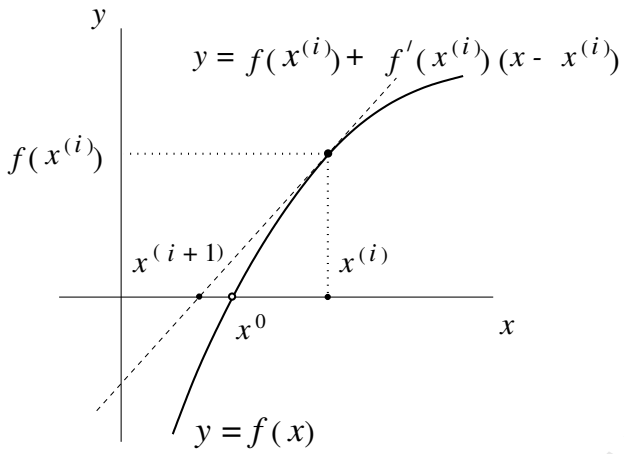

Figure 3.1: Newton iterations. Figure taken from [53].

Given that our initial guess $x^{(0)}$ is already close to the equilibrium x^0, it is reasonable to assume that the Jacobian matrix A does not change much throughout Newton's method. Thus we can approximate A by the initial matrix $A(x^{(0)})$ for all iterations. This gives us the Newton-chord iteration formula:

$$x^{(j+1)} = x^{(j)} + \eta^{(j)}, \quad j = 0, 1, 2, \ldots, \tag{3.7}$$

where the displacement $\eta^{(j)}$ is now defined by

$$A(x^{(0)})\eta^{(j)} = -f(x^{(j)}). \tag{3.8}$$

The Newton-chord method also convergences, but the cost of computational efficiency is that the convergence is less rapid [34].

Theorem 3.2. *Under the conditions of Theorem 3.1, there is a neighbourhood U of x^0 such that the Newton-chord iterations* (3.7), (3.8) *converge to x^0 from any initial point $x^0 \in U$. Moreover,*

$$\|x^{(j+1)} - x^0\| \leq \kappa_1 \|x^{(j)} - x^0\|, \quad j = 0, 1, 2, \ldots,$$

for some $0 < \kappa_1 < 1$, uniformly for $x^0 \in U$.

We have a sufficiently close approximation to the equilibrium x^0 when some convergence criteria are satisfied. If the Newton iterations converge, then both the norm of the displacement $\|\eta^{(j)}\|$ and the norm of the function $\|f(x^{(j)})\|$ must tend to zero. Thus our criteria for convergence are

$$\|\eta^{(j)}\| < \epsilon_x \quad \text{and} \quad \|f(x^{(j)})\| < \epsilon_f,$$

where ϵ_x and ϵ_f are user-defined tolerances.

After an equilibrium x^0 has been located within desired accuracy, we can analyse the local phase portrait by determining the stability of x^0. In the generic case, the stability of x^0 is determined by the equilibrium point's eigenvalues, which are the roots of the characteristic polynomial

$$p(\lambda) = \det(A - \lambda I_n).$$

Most eigenvalue solvers, AUTO included, will use transformations to bring A into a block diagonal form before extracting the eigenvalues, rather than explicitly constructing the characteristic polynomial.

3.2 Location of limit cycles

Finding limit cycles of system (3.2) is naturally a more complicated task than finding its equilibria. If the limit cycle is stable or totally unstable we could try to find it by direct numerical simulation. However, this trick will fail if we are trying to locate a saddle cycle - a limit cycle that has both a stable and an unstable manifold.

More generally we assume that the position of the cycle is known approximately and then seek to locate it more accurately. So, if we know that system (3.1) has a limit cycle at the (fixed) parameter value $\alpha = \alpha_0$, then we can "continue" it with respect to α by making small steps in α. If the limit cycle varies continuously with α, its position at the previous α provides a good approximation of the cycle at the next α. The limit cycle will vary continuously near α_0 assuming the it does not undergo a bifurcation near α_0. A sufficient condition for this assumption is the hyperbolicity of the limit cycle, which is defined in an analogous manner to the case of equilibria.

It is convenient to formulate this task of cycle location as a periodic boundary-value problem (BVP) on a fixed interval. We consider the cycle period T as an extra parameter which we scale out, $t = T\tau$, and seek solutions of the system

$$\frac{du}{d\tau} = Tf(u). \tag{3.9}$$

A solution $u(\tau)$ to (3.9) with fixed T and satisfying the periodic boundary conditions

$$u(0) = u(1) \tag{3.10}$$

corresponds to a T-periodic solution of (3.2).

The boundary conditions (3.10) are not sufficient to define the periodic solution uniquely as we have an extra degree of freedom, the cycle period T. This degree of freedom is related to the time translational invariance of the periodic BVP: any time shift of a solution to (3.9), (3.10) is another solution. Thus we need to append an extra phase condition to the problem (3.9), (3.10)

to select a unique solution. There are several ways to set up such a phase condition. A particularly reliable condition (and the one used in AUTO) is

$$\int_0^1 \langle u(\tau), \dot{v}(\tau) \rangle d\tau = 0. \tag{3.11}$$

Here $v(\tau)$ is the (normalised) periodic solution corresponding to the limit cycle at the "previous" parameter value of α, henceforth referred to as the reference solution; and $\langle \cdot, \cdot \rangle$ denotes the regular dot product on $\mathbb{R}^n$. Condition (3.11) is called the integral phase condition. One can show [29] that it is a necessary condition for a minimum of the "error"

$$\rho(\sigma) = \int_0^1 \|u(\tau + \sigma) - v(\tau)\|^2 d\tau,$$

between the (normalised) periodic solutions u and v with respect to time shifts σ.

To solve the BVP (3.9)-(3.11) we have to first reduce it to a finite-dimensional problem. There are several methods for such a discretisation but we will confine our attention to orthogonal collocation, the discretisation AUTO uses.

We introduce a partitioning of the temporal (τ) interval $[0, 1]$ by $N - 1$ mesh points,

$$0 = \tau_0 < \tau_1 < \ldots < \tau_N = 1,$$

and approximate the solution within each subinterval $[\tau_j, \tau_{j+1}]$, $j = 0, 1, \ldots, N - 1$, by a piecewise-differentiable vector-polynomial $u^j(\tau)$ of maximal degree m. We demand that the approximate solution *exactly* satisfies system (3.9) at m collocation points within each subinterval:

$$\tau_j < \zeta_{j,1} < \zeta_{j,2} < \ldots < \zeta_{j,m} < \tau_{j+1}.$$

That is to say, we require that

$$\left. \frac{du^{(j)}}{d\tau} \right|_{\tau = \zeta_{j,i}} = Tf\left(u^{(j)}(\zeta_{j,i})\right), \tag{3.12}$$

for all $i = 1, \ldots, m$, and $j = 0, 1, \ldots, N - 1$.

We characterise each polynomial $u^{(j)}(\tau)$, $j = 0, 1, \ldots, N-1$, by a vector

$$u^{j,k} = u^{(j)}(\tau_{j,k}) \in \mathbb{R}^n, \quad k = 0, 1, \ldots, m,$$

which represents the unknown solution at equidistant points

$$\tau_j = \tau_{j,0} < \tau_{j,1} < \tau_{j,2} < \ldots < \tau_{j,m} = \tau_{j+1},$$

given by

$$\tau_{j,k} = \tau_j + \frac{k}{m}(\tau_{j+1} - \tau_j), \quad j = 0, 1, \ldots, N - 1, \quad k = 0, 1, \ldots, m.$$

The polynomial $u^{(j)}(\tau)$ can then be represented via the interpolation formula

$$u^j(\tau) = \sum_{i=0}^{m} u^{j,i} \ell_{j,i}(\tau), \tag{3.13}$$

where $\ell_{j,i}(\tau)$ are the Lagrange basis polynomials:

$$\ell_{j,i}(\tau) = \prod_{k=0, k\neq i}^{m} \frac{\tau - \tau_{j,k}}{\tau_{j,i} - \tau_{j,k}},$$

which satisfy

$$\ell_{j,i}(\tau_{j,k}) = \begin{cases} 1 & \text{if } i = k, \\ 0 & \text{if } i \neq k. \end{cases}$$

Equations (3.12) can now be treated as equations for $u^{j,i}$. The periodic boundary condition (3.10) and the phase condition (3.11) can be substituted by their discrete counterparts,

$$u^{0,0} = u^{N-1,m} \tag{3.14}$$

and

$$\sum_{j=0}^{N-1} \sum_{i=0}^{m} \omega_{j,i} \langle u^{j,i}, \dot{v}^{j,i} \rangle = 0, \tag{3.15}$$

where $\dot{v}^{j,i}$ are the values of the derivative of the reference periodic solution at the points $\tau_{j,i}$, and $\omega_{j,i}$ are the Lagrange quadrature coefficients. Equations (3.12), (3.14) and (3.15) comprise a system of $nmN + n + 1$ equations for the unknown components of $u^{j,i}$ and the period T. The resulting finite dimensional system can be solved by the Newton or Newton-chord method, or a combination of the two. The method of orthogonal collocation is made efficient by taking into account the block structure of the Jacobian. Moreover, we can also extract the cycle multipliers from the Jacobian and determine the stability of the located limit cycle.

Finally, we need to discuss how to select the collocation points $\{\zeta_{j,i}\}$. The optimal choice is to place them at the Gauss points, which are the roots $\zeta_{j,i}$, $i = 1, 2, \ldots, m$, of the mth degree Legendre polynomial relative to the subinterval $[\tau_j, \tau_{j+1}]$. These roots are tabulated numerically in the standard interval $[-1, 1]$ and can be easily translated to the subinterval $[\tau_j, \tau_{j+1}]$. Collocation at Gauss points leads to an extremely high accuracy of approximation of smooth solutions, thus making the method of orthogonal collocation very reliable and effective.

3.3 The continuation problem

We now allow α in system (3.1) to vary. We wish to construct the one-parameter bifurcation diagram by studying the dependence of the equilibria and limit cycles on α as well as locating and analysing their bifurcations.

Consider the equilibrium points of (3.1), which satisfy

$$f(x, \alpha) = 0. \tag{3.16}$$

Equation (3.16) is a system of n equations in $\mathbb{R}^{n+1}$ with coordinates (x, α). Generically, (3.16) defines a smooth curve in $\mathbb{R}^{n+1}$.

Computing the curve of equilibrium points of (3.1) is a particular case of the continuation problem, which more generally entails finding a curve M in $\mathbb{R}^{n+1}$ defined by n equations,

$$F(y) = 0, \quad F : \mathbb{R}^{n+1} \to \mathbb{R}^n; \tag{3.17}$$

for example, in the case of equilibria we have $y = (x, \alpha)$. The Implicit Function Theorem guarantees that system (3.17) locally defines a smooth curve passing through a point y^0 satisfying (3.17), provided the rank of the Jacobian matrix of (3.17) at y^0, $J = F_y(y^0)$, is n. This condition on the rank of the Jacobian matrix is known as regularity. The regularity of M is essentially equivalent to the existence of a unique tangent direction at each point $y \in M$.

Determining the numerical solution of the continuation problem involves computing a sequence of points, $y^1, y^2, y^3, \ldots$, which approximate the curve M within desired accuracy. We assume that we have an initial point y^0 which is sufficiently close to the curve from which we can begin the numerical continuation. This initial point could be an known analytical solution or a numerical solution generated by direct numerical simulation for example.

We turn now to the actual mechanics of the continuation. We will be concerned with predictor-corrector methods which loop through three steps until a user-defined accuracy is achieved:

(i) *prediction of the next point;*
(ii) *correction;*
(iii) *step-size control.*

3.3.1 Prediction

Assume that we have an initial point y^j in the sequence. Then the next point can be estimated using the tangent prediction:

$$\tilde{y}^{j+1} = y^j + h_j v^j, \tag{3.18}$$

where h_j is the current step size and $v^j \in \mathbb{R}^{n+1}$ is the normalized tangent vector to the curve M at the point y^j.

The tangent vector v^j can be determined from (3.17), but we first need to choose a parametrisation for the curve near y^j. Two convenient parametrisations, discussed in more detail below, are any one of the coordinates $y = (x, \alpha)$ (natural continuation) and s, the arclength of the curve M (arclength or pseudo-arclength continuation). For the present discussion let us choose the arclength s as our parametrisation. Substituting $y = y(s)$, with $y(0) = y^j$, into (3.17) and computing the derivative with respect to s gives

$$J(y^j)v^j = 0, \tag{3.19}$$

since $v^j = \dot{y}(s)$. Here the dot now denotes differentiation with respect to s and $J(y^j)$ is the Jacobian of (3.17) evaluated at y^j,

$$J(y^j) = \left.\frac{\partial F}{\partial y}\right|_{y=y^j}.$$

To compute the tangent vector v^j from (3.19) we still have to fix its norm. A simple way to achieve this is to fix one of its components, say $v_{i_0} = 1$, and solve the system for the other components before normalizing the resulting vector.* This amounts to solving the $(n+1)$-dimensional appended system,

$$\begin{pmatrix} J \\ (v^{j-1})^T \end{pmatrix} v^j = \begin{pmatrix} 0 \\ 1 \end{pmatrix}, \tag{3.20}$$

where $v^{j-1} \in \mathbb{R}^{n+1}$ is the tangent vector at the previous point y^{j-1} on the curve M. Assuming that M is a regular curve and that the points y^j and y^{j-1} are sufficiently close, system (3.20) will nonsingular.

3.3.2 Correction

We can refine our predicted point $\tilde{y}^{j+1}$ to within a specified accuracy by using a corrector method. The corrector method typically used is a Newton-like method. Because standard Newton methods require that the number of equations equal the number of unknowns, we append an extra scalar condition,

$$g^j(y) = 0, \tag{3.21}$$

to (3.17) and apply Newton's method to the system

$$\begin{cases} F(y) = 0, \\ g^j(y) = 0. \end{cases} \tag{3.22}$$

Geometrically, solving system (3.22) means looking for an intersection of the curve M with some surface near $\tilde{y}^{j+1}$. There are several different ways to specify this surface with the function $g^j(y)$.

*An index i_0 that ensures the solvability of the linear system is guaranteed to exist.

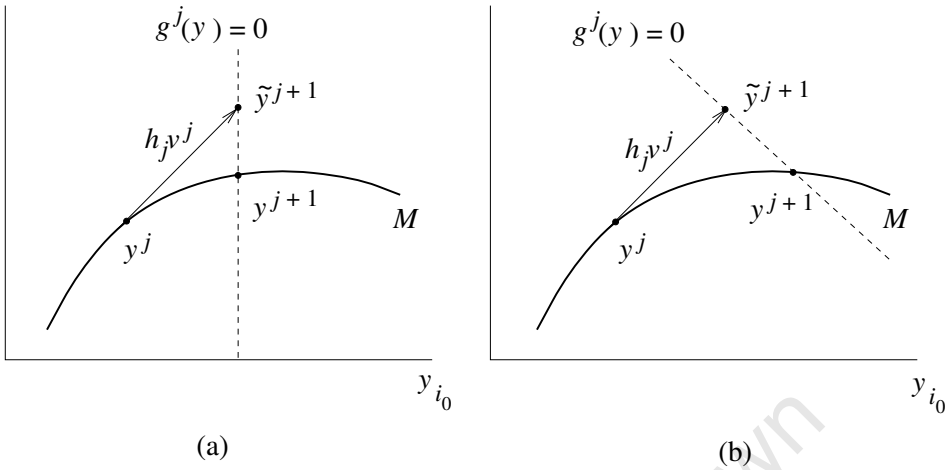

Figure 3.2: (a) Natural and (b) pseudo-arclength continuation. Figure taken from [53].

(Natural continuation) A simple choice for the scalar condition (3.21) is to take a hyperplane passing through the point $\tilde{y}^{j+1}$ that is orthogonal to one of the coordinate axes:

$$g^j(y) = y_{i_0} - \tilde{y}_{i_0}^{j+1}. \tag{3.23}$$

A good choice for the coordinate y_{i_0} is the most rapidly changing coordinate along M. Thus the choice of i_0 is provided by the index of the component of v^j with the maximum absolute value; the situation is illustrated in Figure 3.2 (a). Natural continuation is so called because condition (3.23) selects one of the (natural) coordinates $y = (x, \alpha)$ to step along the curve M with (although the coordinate may differ from step to step).

(Pseudo-arclength continuation) We could alternatively select a hyperplane passing through the point $\tilde{y}^{j+1}$ that is orthogonal to the vector v^j:

$$g^j(y) = \langle y - \tilde{y}^{j+1}, v^j \rangle = \langle y - y^j, v^j \rangle - h_j, \tag{3.24}$$

as show in in Figure 3.2 (b). Condition (3.24) amounts to stepping along the curve M in steps measured along the distance of the curve (i.e. the arclength s). Pseudo-arclength continuation turns out to be more robust than natural continuation and is the preferred method implemented in AUTO.

If the curve M is regular and the step size h_j is sufficiently small, Newton iterations for (3.22) will converge to a point y^{j+1} on the curve M from the predicted point $\tilde{y}^{j+1}$ for both continuation methods.

3.3.3 Step-size control

There are a number of ways to control the step size h_j, but the simplest and most reliable is to implement a *convergent-dependent control*: we decrease the step size and repeat the corrections if no convergence occurs after a prescribed number of iterations; we increase the step size h^{j+1} with respect to h^j if the convergence occurs after only a few iterations; and we keep the current step size $h^{j+1} = h^j$ if the convergence requires a moderate number of iterations.

3.3.4 Continuation of limit cycles

By performing a discretisation of the periodic boundary-value problem, the continuation of limit cycles in one-parameter systems also reduces to the continuation problem:

$$\begin{cases} \dot{u}(\tau) - Tf(u(\tau), \alpha) = 0, \\ u(1) - u(0) = 0, \\ \int_0^1 \langle u(\tau), \dot{u}_0(\tau) \rangle d\tau = 0, \end{cases}$$

where the last equation is the integral phase condition with reference solution $u_0(\tau)$. We denote the resulting resulting system by

$$\mathcal{F}(\xi, \alpha) = 0, \quad \mathcal{F} : \mathbb{R}^{N+1} \to \mathbb{R}^N,$$

where $\xi \in \mathbb{R}^N$ is the discretisation data corresponding to $u(\cdot)$ and the cycle period T, and we have highlighted the system's dependence on α. In the context of orthogonal collocation, ξ is composed of the interpolation coefficients $\{u^{j,i}\}$ and T. We remind the reader that the reference periodic solution u_0 is taken to be a solution corresponding to the cycle obtained at the previous step (in α) along the bifurcation curve M.

3.3.5 Detection and location of bifurcations

Finally, we turn to the problem of detection and location of bifurcations. Our approach is to define a smooth scalar function, called a test or bifurcation function, that will vanish at the bifurcation points. A bifurcation will be detected between two successive points y^k and y^{k+1} on the curve

$$F(y) = 0, \quad F : \mathbb{R}^{n+1} \to \mathbb{R}^n,$$

if the test function $\psi = \psi(y)$ has the opposite signs at these points

$$\psi(y^k)\psi(y^{k+1}) < 0. \tag{3.25}$$

Once detected we can locate the point where ψ vanishes more accurately by applying a Newton-like method to the system

$$\begin{cases} F(y) = 0, \\ \psi(y) = 0, \end{cases} \tag{3.26}$$

with the initial approximation $y^{(0)} = y^k$.

Consider then the equilibrium curve

$$f(x, \alpha) = 0, \quad x \in \mathbb{R}^n, \ \alpha \in \mathbb{R}^1, \tag{3.27}$$

corresponding to the system (3.1). If we denote the eigenvalues of the Jacobian matrix f_x evaluated at (x, α) by $\lambda_i(x, \alpha)$, then the test function

$$\psi_{\text{sn}}(x, \alpha) = \lambda_1(x, \alpha)\lambda_2(x, \alpha) \dots \lambda_n(x, \alpha), \tag{3.28}$$

will vanish at a saddle-node bifurcation (where one of the eigenvalues equals zero). To avoid explicitly computing all the eigenvalues $\lambda_i(x, \alpha)$ we could use an equivalent test function

$$\psi_{\text{sn}}(x, \alpha) = \det\left(\frac{\partial f(x, \alpha)}{\partial x}\right). \tag{3.29}$$

Similarly, the test function

$$\psi_{\text{H}}(x, \alpha) = \prod_{i>j} (\lambda_i(x, \alpha) + \lambda_j(x, \alpha)) \tag{3.30}$$

will detect Hopf bifurcations (where there is a pair of eigenvalues $\lambda_{1,2} = \pm i\omega_0$). However, we have to be careful to ignore points where there is a pair of real eigenvalues

$$\lambda_1 = \kappa, \lambda_2 = -\kappa,$$

for which $\psi_{\text{H}} = 0$ also. We can avoid explicit computation of all the eigenvalues by using the bialternate product to compute ψ_{H}; an introduction to the bialternate product and relevant details of avoiding the explicit computation of the eigenvalues can be found in [53].

We can also construct test functions to locate bifurcations for cycles. Given the Poincaré return map

$$x_{k+1} = P(x_k, \alpha), \quad x_k \in \mathbb{R}^n, \ \alpha \in \mathbb{R},$$

we wish to continue its fixed point curve

$$P(x, \alpha) - x = 0.$$

Let $\mu_1, \mu_2, \ldots, \mu_n$ be the multipliers of the Jacobian matrix $A = P_x$ evaluated at (x, α). The following test functions will locate saddle-node, period-doubling and Neimark-Sacker (torus) bifurcations respectively:

$$\psi_{\mathrm{t}} = \prod_{i=1}^{n}(\mu_i - 1), \tag{3.31}$$

$$\psi_{\mathrm{pd}} = \prod_{i=1}^{n}(\mu_i + 1), \tag{3.32}$$

$$\psi_{\mathrm{NS}} = \prod_{i>j}(\mu_i \mu_j - 1). \tag{3.33}$$

To confirm that we have detected a true Neimark-Sacker bifurcation we must check that $\psi_{\mathrm{NS}} = 0$ due to the presence of *nonreal* multipliers with unit product.

As in the case of equilibria, we can express the test functions in terms of the Jacobian matrix itself:

$$\psi_{\mathrm{t}} = \det(A - 1), \tag{3.34}$$

$$\psi_{\mathrm{pd}} = \det(A + 1). \tag{3.35}$$

For the Neimark-Sacker bifurcation we must again turn to the bialternate product; details are available in [53].

The test functions are not the full story though. To locate and analyse bifurcation points we also have to check the nondegeneracy conditions. That is, we need to verify the transversality condition and compute the relevant topological normal form coefficients. This is generally amounts to a large amount of algebraic work which we shall not delve into. The interested reader is referred to Kuznetsov [53] for an accessible exposition.

We shall also use two-parameter bifurcation analysis to continue one-parameter bifurcations of equilibria (Hopf bifurcations) and limit cycles (period-doubling bifurcations), and to compute the locus of homoclinic orbits. Computing the approximate loci of the homoclinic orbits can be achieved by fixing the period T of a large-period periodic solution and continuing the solution in the control parameters. In a similar manner, continuing the one-parameter bifurcations can intuitively be understood as continuing the appended-system given by appending the condition that the relevant test function remain zero, $\psi_{\mathrm{test}} = 0$, to system (3.17). However, the actual implementation of these continuation algorithms is quite a bit more involved [53].

Chapter 4

Numerical Algorithms

In our study we will make use of two numerical algorithms: a continuation algorithm and a direct simulation algorithm, the Fourier split-step method. The latter method has proven particularly successful in the study of the nonlinear Schrödinger equations (see [17] and references cited therein) and we will employ it to confirm the reported stability of the numerically continued solutions.

For the numerical continuation we use AUTO [30] which is a pseudo-arclength continuation software. As alluded to in §1.1.1 and from our discussion of numerical continuation theory in Chapter 3 we recall that the only solutions we are able to continue are solutions governed by ODEs. As both the parametrically driven NLS and the directly driven NLS are PDEs we need to reduce them to respective systems of ODEs. We shall do this by way of Fourier expansion.

The actual computations for the numerical continuation simulations were carried out on the UCT and SAGrid High Performance Computing servers, each server running 8 2.6 GHz CPUs with between 16 and 32 GB of RAM. The computations for the direct simulations were performed on a quad core 1.6 GHz PC with 8GB of RAM.

4.1 Parametrically driven NLS

4.1.1 Numerical continuation

We include the parametrically driven NLS here for reference purposes:

$$\psi_t = i\psi_{xx} + 2i|\psi|^2\psi - i\psi - ih\psi^* - \gamma\psi. \tag{4.1}$$

Our approach to numerically continuing periodic solutions to the parametrically driven NLS is as follows. For fixed damping γ, we initialise our computation by continuing the stationary ψ_+ soliton solution (1.4) in the driving strength parameter h until the point of Hopf bifurcation. The periodic solution born at the Hopf point is then continued in h.

Before outlining our algorithm we make an important observation. Because the parametrically driven NLS (4.1) is parity invariant, if we start from a solution that is spatially symmetric then the time evolution of this solution will also be spatially symmetric. As we have taken a spatially symmetric stationary solution, ψ_+, as our initial condition there is therefore no loss of generality in demanding that our continued solutions be spatially symmetric. Thus we can confine our algorithm to the continuation of solutions which are even in space: $\psi(-x,t) = \psi(x,t)$.

Because of this symmetry, our soliton solution will always be periodic over its spatial domain. Indeed, if we centre our solution on the interval $[-L/2, L/2]$ at $x = 0$, then by the spatial symmetry we have, in particular, that $\psi(-L/2,t) = \psi(L/2,t)$ for all time t. Thus we can expand ψ in a truncated Fourier series in space:

$$\psi(x,t) = \sum_{n=-N}^{N} \widehat{\psi}_n(t) e^{i\mu_n x}, \tag{4.2}$$

where $\mu_n = (2\pi n/L)$, $N \in \mathbb{N}$ is the truncation order and $\widehat{\psi}_n(t)$ are (complex valued) Fourier coefficients.

We are interested in solutions that are time-periodic with period T. Given that the period of the solutions varies as a function of the driving strength h and damping γ, it will be beneficial to scale out the time dependence. Thus we make the transformation $t = T\tau$ (so that $\tau \in [0,1]$) and regard T as a parameter. Substituting now the Fourier expansion (4.2) into the parametrically driven NLS (4.1), using the linear independence of the exponentials and breaking the Fourier coefficients into their real and imaginary parts $\widehat{\psi}_n(t) = a_n(t) + ib_n(t)$, we find that the parametrically driven NLS (4.1) can be written as a system of ODEs in Fourier space:

$$\begin{cases} \dot{a}_n = T\left[(\mu_n^2+1)b_n - hb_{-n} - \gamma a_n - 2\mathrm{Im}\left\{\mathbb{F}_n(|\psi|^2\psi)\right\}\right], \\ \dot{b}_n = T\left[-(\mu_n^2+1)a_n - ha_{-n} - \gamma b_n + 2\mathrm{Re}\left\{\mathbb{F}_n(|\psi|^2\psi)\right\}\right]. \end{cases} \tag{4.3}$$

Here the overdot denotes differentiation with respect to τ, $-N \leq n \leq N$, and $\mathbb{F}_n(f(x))$ is the nth Fourier coefficient of the function $f(x)$.

To compute the Fourier coefficients of the nonlinear term in system (4.3) we first reconstruct the solution ψ using the inverse Fourier transform, then compute the nonlinear term $|\psi|^2\psi$ directly before finally extracting its Fourier coefficients with the (forward) Fourier transform. The particular FFT (Fast Fourier Transform) algorithm we use in this work is the FFTW [39].

It follows from the spatial symmetry of $\psi(x,t)$ that

$$\widehat{\psi}_{-n}(t) = \widehat{\psi}_n(t).$$

Thus we need only consider nonnegative coefficients in the Fourier expansion (4.2). Our problem then is to continue the system of equations

$$\begin{cases} \dot{a}_n = T\left[(\mu_n^2 + 1 - h)b_n - \gamma a_n - 2\mathrm{Im}\left\{\mathbb{F}_n(|\psi|^2\psi)\right\}\right], \\ \dot{b}_n = T\left[-(\mu_n^2 + 1 + h)a_n - \gamma b_n + 2\mathrm{Re}\left\{\mathbb{F}_n(|\psi|^2\psi)\right\}\right], \end{cases} \tag{4.4}$$

with the periodic boundary conditions

$$a_n(0) = a_n(1), \quad b_n(0) = b_n(1), \tag{4.5}$$

and where $0 \leq n \leq N$.

We are left with two parameters to fix, namely the Fourier truncation order N and the spatial interval size L.* Naturally, we want to ensure that we capture the core of the soliton in the spatial interval but we also know that the larger the spatial interval the more Fourier modes we require to discern small fluctuations in the solution. Although we shall have occasion to vary N, along with AUTO defined parameters for the temporal mesh and convergence criteria, from simulation to simulation, we can get a good estimate for L as follows. We set the Fourier truncation order to $N = 256$ and then determine the largest possible spatial interval such that we can discern half wavelength fluctuations of order $\delta x = 0.2$:

$$\frac{\pi}{\delta x} = \max\{\mu_n\} \Rightarrow L = 0.4N \approx 32\pi.$$

Thus the spatial interval is taken as $[-16\pi, 16\pi]$. This offers a good compromise between emulating the infinite line while still allowing us to discern small amplitude radiation waves. For smaller damping γ we will require more Fourier modes to discern the small wavelength fluctuations and thus ensure the convergence of the solution.

An immediate advantage we have gained over other continuation algorithms which have been applied to the parametrically driven NLS [15, 84] is that we do not require that the solution decays to zero for large x. Indeed, the solution need only be periodic in space to justify our Fourier expansion (4.2) and, as highlighted above, this assumption is automatically satisfied by the spatial symmetry of the parametrically driven NLS.

It is worthwhile commenting on our choice to Fourier expand our solution (4.2) in space rather than in time. There are several advantages that motivated this decision. The first advantage follows from the observation that working in Fourier space reduces differentiation to multiplication. Fourier expanding in space reduces the second derivative term ψ_{xx} to ψ (multiplied by a constant), while the Fourier expansion in time reduces the first derivative term ψ_t to ψ (multiplied by a constant). Because we need to

*Recall from (4.2) that the *effective* number Fourier modes in our Fourier expansion is $\mathcal{N} = 2N + 1$.

convert our PDE into a system of *first order* ODEs the Fourier expansion in space is advantageous. Indeed, Fourier expanding in time reduces our PDE to a system of second order ODEs (in x), which then still need to be reduced to a system of first order ODEs, while Fourier expanding in space reduces our PDE directly into a system of first order ODEs (in t). The former expansion therefore yields twice as many equations in our final system of ODEs.

The Fourier expansion in space also makes direct use of the spatial symmetry to decrease the computational load; we would not be able to take advantage of this symmetry using AUTO's built-in collocation mesh. Thirdly, the Fourier expansion in space is more robust for our purposes. This follows from the fact that the spatial interval length L is fixed while the period T is not, and that we are able to restart the continuation mid-computation and alter the collocation mesh but not the number of Fourier modes. Therefore, using the collocation mesh on the temporal domain allows us to refine our mesh depending on the value of period T.

We also remark that a great variety of other numerical continuation software packages exist (for example [28] and [58]). Of all the continuation packages, however, AUTO has been through the most versions, is the most widely used and has weathered the periodic euphoria associated with new software packages that come and go.

4.1.2 Split-step Fourier method

AUTO constructs the Jacobian matrix $A_j = f_x(x, \alpha_j)$ and extracts the eigenvalues at each step α_j and is therefore able to report the stability of the solution for each α_j. It is beneficial to be able to confirm that the solutions are indeed of the reported stability through direct numerical simulation of the solution. For this purpose we employ the split-step Fourier method as our numerical simulator.

More specifically, we check the solution stability by first extracting the Fourier coefficients from the numerical continuation (for a fixed h), then reconstructing the solution from these coefficients using an FFT algorithm and finally using the reconstructed solution $\psi(x,t)$, with some $t = t_0$, as the initial condition for the direct numerical simulation. Naturally, a stable periodic soliton will maintain its temporal and spatial shape over time, while an unstable solution will evolve into a different nontrivial solution, decay to zero or blow up.

The split-step Fourier method is a particularly effective numerical simulator for the nonlinear Schrödinger equation and PDEs in general. Indeed, Taha and Ablowitz [77] showed through extensive computational comparisons of the split-step Fourier method to a variety of numerical schemes including several finite difference and pseudospectral methods, that on the whole the split-step Fourier method was superior. In particular, for the

nonlinear Schrödinger equation, the success of the split-step Fourier method follows largely from our ability to solve the arising linear and nonlinear governing equations explicitly. With this justification, we now derive the algorithm.;the derivation of the split-step Fourier method given in this section is adapted from the author's previous work [55].

Following the standard prescription of the split-step Fourier method we advance the solution as

$$\psi(x, t+\tau) \approx e^{i\tau \mathbf{L}} e^{i\tau \mathbf{N}} \psi(x, t), \tag{4.6}$$

where

$$\mathbf{L}\psi = \psi_{xx} - \psi - h\psi^* + i\gamma\psi, \quad \mathbf{N}\psi = 2|\psi|^2\psi, \tag{4.7}$$

and τ is our step size. We are splitting the system into its nonlinear and linear parts, solving each separately and then stepping in time with each solution sequentially.

The solution to the nonlinear part of the parametrically driven NLS (4.1),

$$v_t = i\mathbf{N}v,$$

subject to the initial condition

$$v(x, 0) = \psi(x, t),$$

at time $t = \tau$ is precisely

$$v(x, \tau) = \psi(x, t) e^{2i\tau|\psi(x,t)|^2} \equiv e^{i\tau \mathbf{N}} \psi(x, t). \tag{4.8}$$

We are then left with the evolution of the linear part,

$$\psi(x, t+\tau) = e^{i\tau \mathbf{L}} v(x, \tau),$$

which denotes the solution $u(x, t)$ of the initial-value problem

$$u_t = i\mathbf{L}u, \quad u(x, 0) = v(x, \tau). \tag{4.9}$$

To determine $e^{i\tau \mathbf{L}}$ we must solve (4.9) or equivalently

$$iu_t + u_{xx} - u + i\gamma u - hu^* = 0 \quad \text{with } h, \gamma > 0. \tag{4.10}$$

The $i\gamma u$ term in equation (4.10) alerts us to the presence of exponential damping. We can peel off this damping by putting

$$u(x, t) = e^{-\gamma t} f(x, t) \tag{4.11}$$

where $f(x, t) = a(x, t) + ib(x, t)$ is a complex function. Substituting the ansatz (4.11) into equation (4.10) and equating the real and imaginary parts we obtain the system

$$\begin{cases} -b_t + a_{xx} - a - ha = 0, \\ a_t + b_{xx} - b + hb = 0. \end{cases} \tag{4.12}$$

Next we expand a and b in the (truncated) Fourier series in space:

$$\begin{aligned} a(x,t) &= \sum_{n=-N}^{N} A_n(t) e^{i\mu_n x}, \\ b(x,t) &= \sum_{n=-N}^{N} B_n(t) e^{i\mu_n x}, \end{aligned} \tag{4.13}$$

where $\mu_n = (2\pi n/L)$ and $N \in \mathbb{N}$ is the truncation order. Substituting the Fourier expansions (4.13) into system (4.12) and rearranging we find

$$\begin{cases} \dot{B}_n = -(\mu_n^2 + 1 + h) A_n, \\ \dot{A}_n = (\mu_n^2 + 1 - h) B_n, \end{cases} \tag{4.14}$$

where the overdot denotes differentiation with respect to time. We now look for a solution of the form

$$\begin{pmatrix} A_n(t) \\ B_n(t) \end{pmatrix} = \begin{pmatrix} \alpha_n \\ \beta_n \end{pmatrix} e^{i\Omega t}, \tag{4.15}$$

with α_n and β_n constants. This yields the algebraic system

$$\begin{cases} i\Omega\beta_n = -(\mu_n^2 + 1 + h)\alpha_n, \\ i\Omega\alpha_n = (\mu_n^2 + 1 - h)\beta_n. \end{cases} \tag{4.16}$$

System (4.16) has nontrivial solutions provided the determinant of the system is zero. That is if

$$\Omega_{1,2} = \pm\sqrt{(1+\mu_n^2)^2 - h^2}. \tag{4.17}$$

Depending on the value of the expression under the square root we would need to consider up to three different cases. However, we will only be using the split-step algorithm to investigate solutions with small driving strengths and thus we can confine our attention to the case $(1+\mu_n^2)^2 - h^2 > 0$. Indeed, since the minimum value of $(1+\mu_n^2)^2$ is always greater than unity, we can consider all small driving strengths $h < 1$. Moreover, in this regime we obtain the solutions

$$\begin{cases} A_n = c_n \cos\omega_n t + d_n \sin\omega_n t, \\ B_n = \left|\dfrac{1+\mu_n^2+h}{1+\mu_n^2-h}\right|^{1/2} \left(-c_n \sin\omega_n t + d_n \cos\omega_n t\right), \end{cases} \tag{4.18}$$

where $\omega_n = |(1+\mu_n^2)^2 - h^2|^{1/2}$ and c_n, d_n are arbitrary real coefficients to be fixed by the initial condition in (4.9). Expanding the real and imaginary parts of the initial condition in Fourier series we have

$$A_n(0) = y_n, \quad B_n(0) = z_n,$$

where y_n and z_n represent the Fourier coefficients of the real and imaginary parts of $v(x,\tau)$ respectively. From system (4.18) we then obtain

$$c_n = y_n, \quad d_n = \left|\frac{1+\mu_n^2-h}{1+\mu_n^2+h}\right|^{1/2} z_n. \tag{4.19}$$

The Fourier transform of our ansatz (4.11) is

$$\widehat{u}_n(t) = e^{-\gamma t}\left(A_n(t) + iB_n(t)\right), \tag{4.20}$$

and therefore, through the inverse Fourier transform of equation (4.20), we have that the numerical solution of the linear part of the parametrically driven NLS evolves as

$$u(x,t) = \sum_{n=-N}^{N} \widehat{u}_n(t) e^{i\mu_n x}. \tag{4.21}$$

We shall primarily be using the split-step Fourier method to simulate weakly damped ($\gamma < 0.05$) solutions to check their stability. In this weakly damped regime the soliton sheds a large amount of energy through radiation (cf. §5.3). Given that we are using a finite approximation to the infinite line for the spatial domain and that we have periodic (spatial) boundary conditions, this radiation will inevitably feed back into the soliton. If we are interested in physical states represented by spatially periodic solutions on a finite interval then this feedback *is* physical. However, it will also be of interest to simulate solutions on the infinite line, in which case we will wish to counter the radiation feedback. We can do this by modifying our system to include a radiation absorbing term at the boundaries as suggested by previous numerical studies [2].

We implement the radiation absorbing term by replacing the damping term $-i\gamma\psi$ in the parametrically driven NLS (4.1) with $-i\widehat{\Gamma}\psi$, where $\widehat{\Gamma}\psi$ is an operator which is defined as follows: replace γ in equation (4.20) with $\widetilde{\gamma} = \gamma + \Gamma$, where the function $\Gamma(x)$ is almost zero within the subinterval $(-30, 30)$ and increases smoothly to the value of approximately 0.35 as $x \to \pm 16\pi$:

$$\Gamma(x) = 0.2\left\{2 + \tanh\left(\frac{x-(16\pi-5)}{5}\right) - \tanh\left(\frac{x+(16\pi-5)}{5}\right)\right\}. \tag{4.22}$$

The form of the corresponding $\widehat{\Gamma}$-operator is

$$\widehat{\Gamma}\psi = (\gamma + \Gamma + i\Gamma_x^2 t^2 - i\Gamma_{xx}t)\psi - 2i\Gamma_x t\psi_x. \tag{4.23}$$

The effect of modifying parametrically driven NLS (4.1) with the $\widehat{\Gamma}$-operator is qualitatively similar to the effect of directly modifying the damping term $-i\gamma\psi$ in equation (4.1) to $-i\widetilde{\gamma}\psi$, in that both will damp radiation for large

$|x|$. The important difference, though, is that with the operator approach we can still solve equation (4.10) explicitly.

Finally, we mention that Bondila [17] obtains from a stability analysis that the numerical solution (4.21) is stable against high frequency perturbations provided

$$\tau < \frac{(\Delta x)^2}{\pi}, \tag{4.24}$$

where Δx is our spatial mesh spacing and τ our temporal step size.

4.2 Directly driven NLS

The continuation and split-step algorithms for the directly driven NLS can be obtained in much the same manner as for the parametrically driven NLS in §4.1. As such we omit the derivation and simply include the final algorithms.

4.2.1 Numerical continuation

Because the directly driven NLS carries the same parity invariance as the parametrically driven NLS we can focus our attention exclusively on symmetric solutions of the directly driven NLS. Furthermore, our soliton solution can always be described as spatially periodic and the Fourier series expansion in space is applicable. Keeping with the notation in §4.1.1, the continuation problem for the directly driven NLS is given by the systems:

$$\begin{cases} \dot{a}_0 = T\left[b_0 - \gamma a_0 - 2\mathrm{Im}\left\{\mathbb{F}_0(|\psi|^2\psi)\right\}\right], \\ \dot{b}_0 = T\left[-a_0 - \gamma b_0 + h + 2\mathrm{Re}\left\{\mathbb{F}_0(|\psi|^2\psi)\right\}\right], \end{cases} \tag{4.25}$$

and

$$\begin{cases} \dot{a}_n = T\left[(\mu_n^2+1)b_n - \gamma a_n - 2\mathrm{Im}\left\{\mathbb{F}_n(|\psi|^2\psi)\right\}\right], \\ \dot{b}_n = T\left[-(\mu_n^2+1)a_n - \gamma b_n + 2\mathrm{Re}\left\{\mathbb{F}_n(|\psi|^2\psi)\right\}\right], \end{cases} \tag{4.26}$$

for $1 \leq n \leq N$, with the periodic boundary conditions

$$a_n(0) = a_n(1), \quad b_n(0) = b_n(1), \tag{4.27}$$

for all $0 \leq n \leq N$.

4.2.2 Split-step Fourier method

In the notation of §4.1.2, we advance the directly driven NLS solution as

$$\psi(x, t+\tau) \approx e^{i\tau\mathbf{L}} e^{i\tau\mathbf{N}} \psi(x,t), \tag{4.28}$$

where **L** and **N** are the respective linear and nonlinear parts of the directly driven NLS. The nonlinear evolution of the directly driven NLS solution is exactly as for the parametrically driven NLS solution:

$$v(x,\tau) = \psi(x,t)e^{2i\tau|\psi(x,t)|^2} \equiv e^{i\tau\mathbf{N}}\psi(x,t). \tag{4.29}$$

The linear evolution of the directly driven NLS is described by

$$u(x,t) = \sum_{n=-N}^{N} \widehat{u}_n(t)e^{i\mu_n x}, \tag{4.30}$$

with

$$\widehat{u}_n(t) = e^{-\gamma t}\left(A_n(t) + iB_n(t)\right). \tag{4.31}$$

The Fourier coefficients A_n and B_n are now given by

$$\begin{cases} A_n = c_n \cos\omega_n t + d_n \sin\omega_n t + h/\omega_n, \\ B_n = -c_n \sin\omega_n t + d_n \cos\omega_n t, \end{cases} \tag{4.32}$$

where $\omega_n = |1 + \mu_n^2|$ and c_n, d_n are real coefficients fixed by the Fourier coefficients of the initial condition (the solution value after the nonlinear evolution step):

$$c_n = y_n - h/\omega_n, \quad d_n = z_n. \tag{4.33}$$

Chapter 5

Continuation of Temporally Periodic Solitons of the Parametrically Driven NLS

In this chapter we present and analyse our numerical results for the continuation of temporally periodic solitons of the parametrically driven NLS. We will focus on the three different damping regimes separately, namely strong damping ($\gamma = 0.3$), moderate damping ($\gamma = 0.2$), and weak damping ($\gamma < 0.05$). We choose to focus on these three regions separately as the dynamics arising in each are qualitatively different. Finally, we summarise and conclude this chapter by presenting the bifurcation diagram in (h, γ) parameter space which offers a summary of the dynamics of the system.

The strong damping regime has been thoroughly studied by Barashenkov, Zemlyanaya and van Heerden [15] and we shall simply use the case $\gamma = 0.3$ as a opportunity to compare or numerics to their results. The moderate damping regime was also studied in the same work [15]. However, the analysis there was incomplete due to the lack of numerical access to large-period periodic soliton solutions. We will therefore supplement their study by revealing, in detail, the bifurcation structure of the periodic solitons before relating the observed dynamics to Shil'nikov's results (cf. Chapter 2). The remaining damping regime, that describing the weakly damped system, has received the least attention in the literature. We give a careful analysis of the fine structure observed there and the unexpected presence of new regions of stable periodic solitons.

A note on the continuation diagrams included in this chapter and the next: Stable parts of solution branches are drawn in solid line, while the unstable parts are drawn in dashed line. Unless otherwise stated, all simulations use a spatial interval of fixed length $L = 32\pi$ and a fixed number of (complex) Fourier modes, dependent on the simulation (257, 513, or 1003). The temporal mesh on the other hand was refined as the period of the soli-

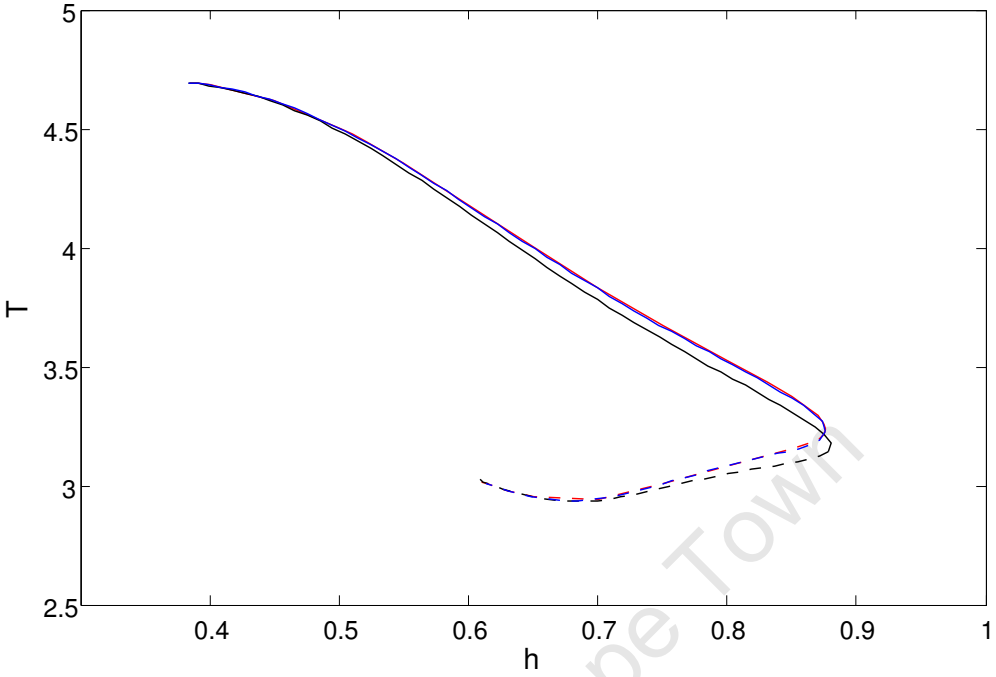

Figure 5.1: Comparison of periodic soliton bifurcation curve for 257- (black) and 513-mode (blue) cases to that of [15] (red) for $\gamma = 0.3$. The blue and red curves are practically indistinguishable.

ton increased. Specifically, the number of collocation points within each subinterval was fixed at NCOL = 4, while the number of subintervals over which the temporal domain was divided, NSTAT, was increased with increasing period T to ensure that we could discern half wavelength temporal fluctuations as small as $\Delta t = 0.2$:

$$\frac{\pi}{\Delta t} = \frac{\text{NCOL} \times \text{NSTAT}}{T} \Rightarrow \text{NSTAT} = \frac{5}{4}\pi T \leq 4T.$$

5.1 Strong damping: $\gamma = 0.3$

Figure 5.1 offers a comparison of the results of Barashenkov, Zemlyanaya and van Heerden [15] to those obtained using our algorithm for the case $\gamma = 0.3$. The 513-mode solution offers excellent correlation with the results obtained by [15], while the 257-mode solution still compares favourably. Given the close correlation of the results we shall generally favour the lesser, and therefore faster, mode expansion (257-modes) where possible and only check these results using the 513-mode solution. For weak damping we shall have to turn to 513-mode and 1003-mode expansions.

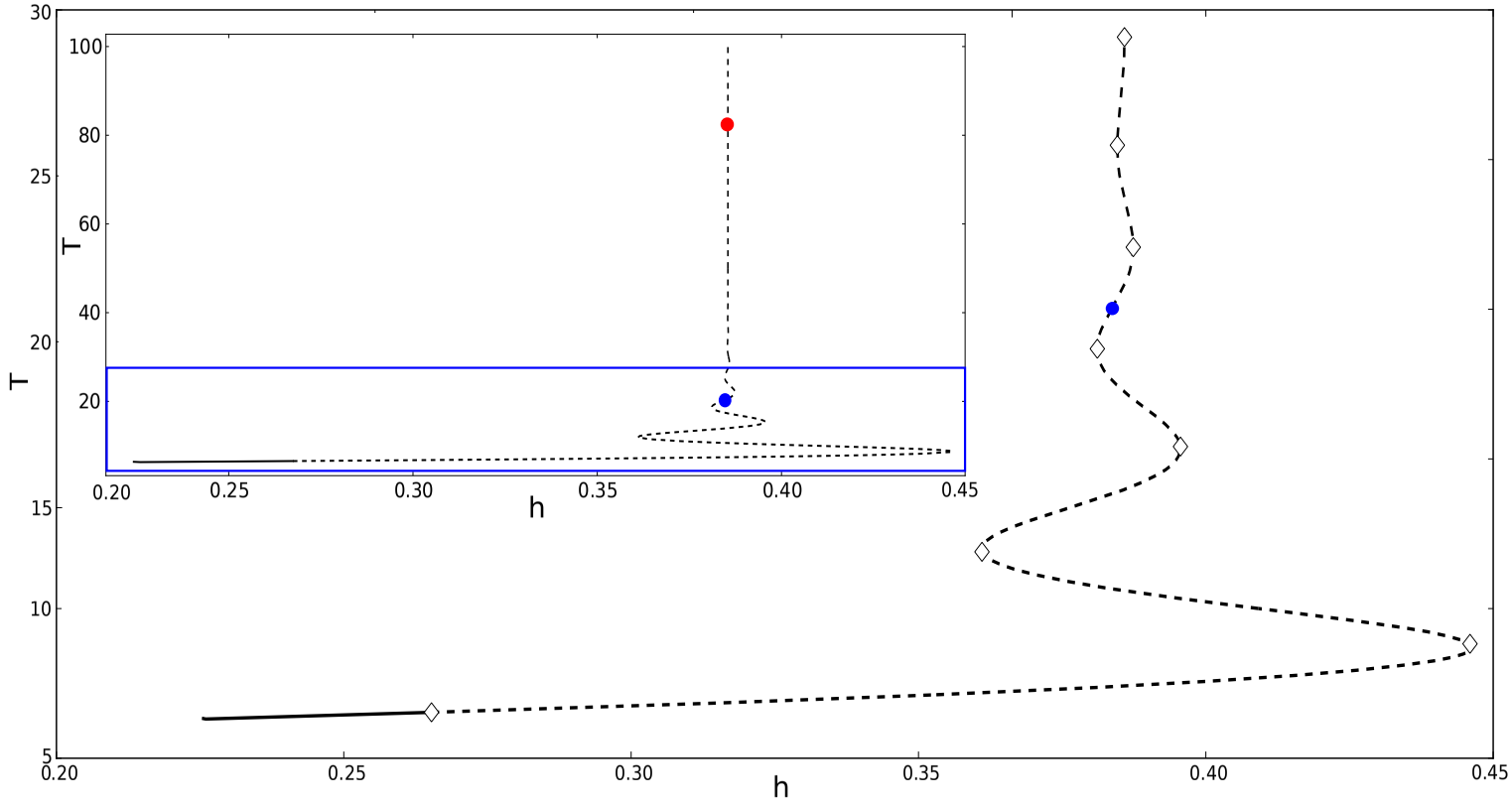

Figure 5.2: Bifurcation diagram of the periodic solitons for moderate damping $\gamma = 0.2$. The inset gives the full bifurcation diagram of which the blue square is enlarged. Open diamonds indicate period-doubling bifurcations. These period-doubling bifurcations were previously unidentified due to their close proximity to the saddle-node bifurcation points. A representative solution (blue dot) and its phase portrait are shown in Figures 5.3 and 5.4 respectively, while the approximate homoclinic solution (red dot) is shown in Figure 5.5.

5.2 Moderate damping: $\gamma = 0.2$

A typical bifurcation curve, with the period T plotted as a function of the driving strength h, of periodic soliton solutions in the moderately damped system is shown in Figure 5.2. All along this curve the solutions are characterised by a single temporal peak. As we ascend the snaking curve, this temporal peak becomes steeper and for very large periods the soliton experiences a quasi-stationary epoch followed by a sharp change in amplitude as shown in Figure 5.3. This is a result of the proximity of the periodic soliton orbit to the stationary soliton ψ_- (1.4). As the orbit passes close to the fixed point it is bottlenecked producing the characteristic plateau structure; away from the bottleneck region the soliton traces out the rest of its orbit relatively quickly. The bottlenecking is further highlighted by the solution phase portrait presented in Figure 5.4.

As the period increases, the periodic solution approximates the homoclinic solution that is bi-asymptotic to the stationary ψ_- soliton with increasing accuracy. Figure 5.5 shows the periodic solution for $T \approx 85$. For larger periods neither the spatial nor the temporal structure of the solution change; we already have a good approximation to the homoclinic solution. A natural question that arises is whether or not one could construct an analytical solution for the homoclinic solution. This question is motivated by previous success [80], where analytical solutions for bound states of quiescent solitons in the parametrically driven NLS were constructed using the Hirota method. However, studying the numerical solution given in Figure 5.5 we note two hindrances to this prospect in the present case: the temporal profile consists of a single large peak surrounded by several minor peaks and there are small radiation waves emanating from the these peaks.* Both these features will not lend themselves to analytical description by, for instance, simple exponentials such as in the Hirota method.

The bifurcation curve in Figure 5.2 strongly resembles the curve of Figure 2.6 in §2.3. Given this resemblance, let us analyse the periodic solitons of the parametrically driven NLS for the presently considered moderately damped case $\gamma = 0.2$ using the theory developed in §2.4. Firstly, based on our numerical results, it is clear that a homoclinic solution exists. And from our discussion of the solution in Figures 5.3 and 5.4 we deduce that the role of the saddle-focus is played by the stationary ψ_- solution. Due to the presence of its zero mode, the ψ_- soliton is clearly not a hyperbolic fixed point. However, the zero mode is due to the translation symmetry of the parametrically driven NLS and as such it cannot be related to any bifurcation. Indeed, as discussed in §2.1, because the zero mode persists as long as the solution itself is defined, we are assured that the ψ_- solution does not undergo any local bifurcation near the homoclinic bifurcation.

*These features are robust and persist to larger periods and for finer temporal meshes.

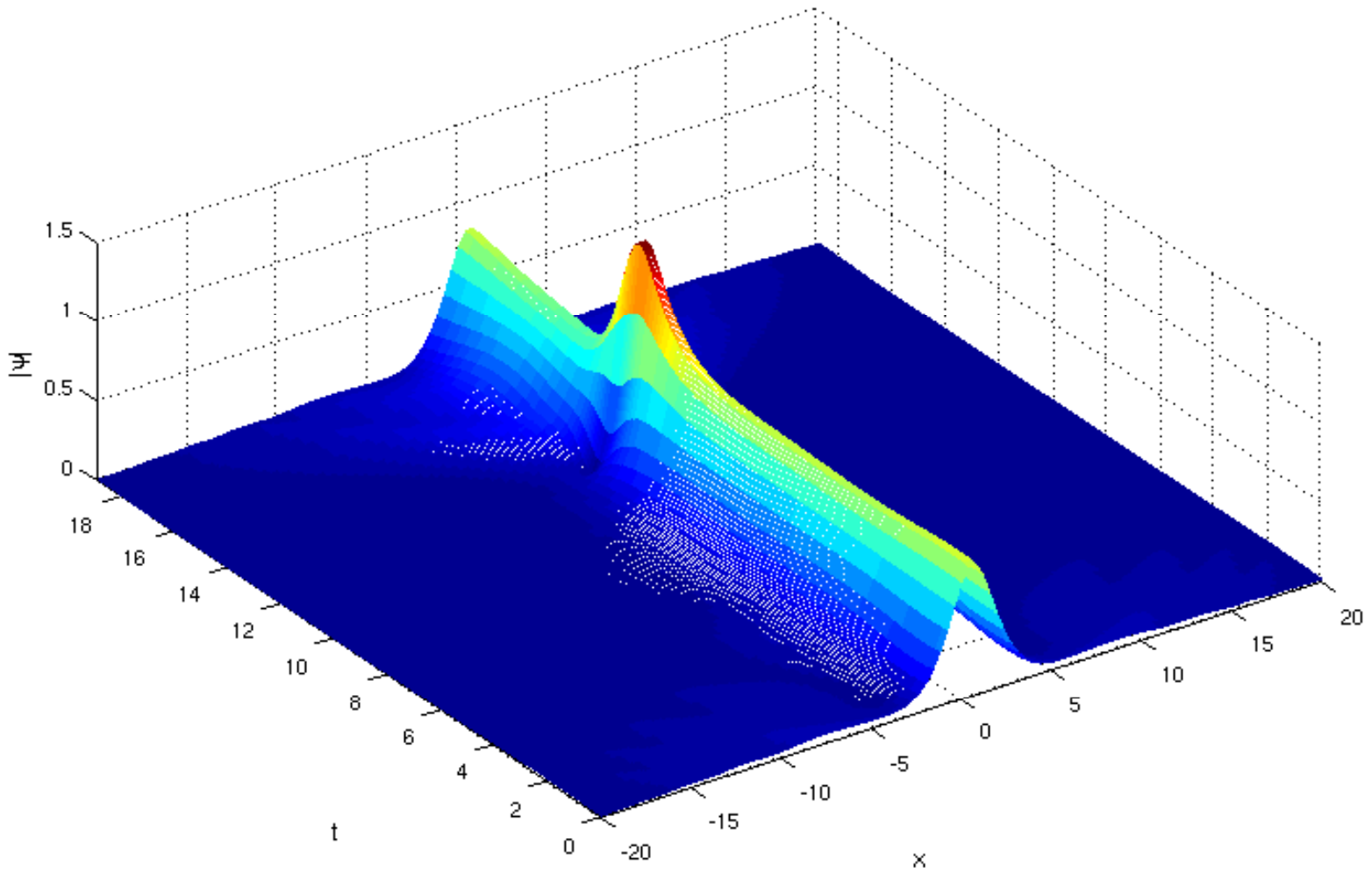

Figure 5.3: Absolute value of the periodic soliton with $\gamma = 0.2$, $h = 0.381$ and $T = 18.82$. Only the central section $[-20, 20]$ of the full spatial interval $[-16\pi, 16\pi]$ is shown. The soliton experiences a quasi-stationary epoch where the orbit of the solution remains near the fixed point ψ_-, followed by a rapid change in amplitude (cf. Figure 5.4).

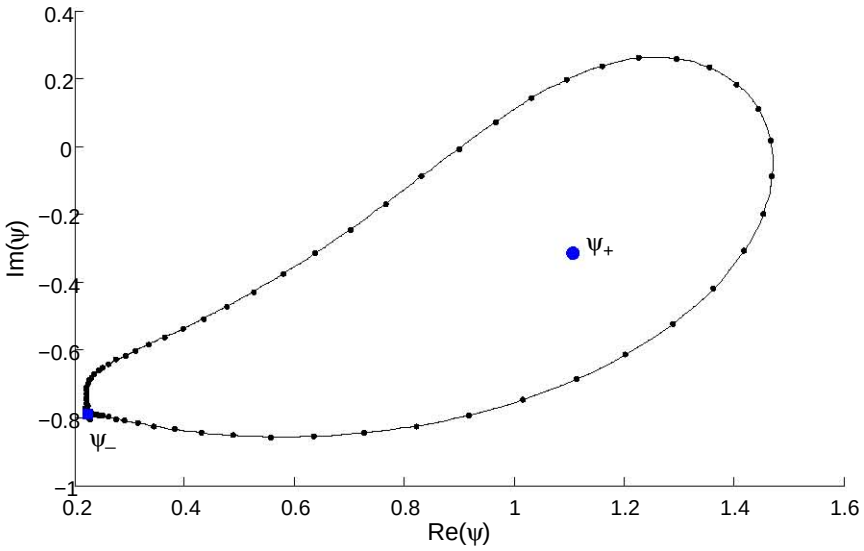

Figure 5.4: Phase portrait of periodic soliton shown in Figure 5.3 taken at $x = 0$. The dots along the curve serve as a temporal measure: a high (low) density of dots indicates that the solution spends more (less) time in a particular region of phase space. The blue square (blue circle) represents the stationary ψ_- (ψ_+) soliton.

Unfortunately, although we are able to skirt around the issue of hyperbolicity, we can go no further with the classical theory. Theorem 2.9 is inapplicable to the parametrically driven NLS as the fixed point ψ_- immediately fails the first genericity condition (H.0): the leading eigenspace T^s is infinite dimensional and not one- or two-dimensional as required. Indeed, from §1.1 we recall that linear spectrum of the stationary ψ_- soliton (the saddle-focus fixed point) consists of two discrete eigenvalues $\lambda_\pm$ (1.10) and a *continuum* of eigenvalues $\lambda = -\gamma + i\omega$ ($\omega_0 \leq |\omega| < \infty$) (1.9). That we are unable to directly apply Theorem 2.9 should not come as a surprise as we are attempting to apply theory developed for n-dimensional systems to the infinite dimensional parametrically driven NLS.

Nevertheless we are able to draw the following satisfactory parallel with Shil'nikov's result. From Figure 5.2 we see that the homoclinic orbit exists at the parameter value $h = 0.385$. For this h (and $\gamma = 0.2$) the "leading" stable and unstable eigenvalues[†] for the ψ_- soliton are, respectively, $\lambda_+ = 1.025$ (1.11) and any single eigenvalue of the family $\lambda = -\gamma + i\omega$ ($\omega_0 \leq |\omega| < \infty$) (1.9). Thus we have that, at the point of the homoclinic bifurcation, the

[†]Recall (Definition 2.4 in §2.4) that the leading stable and unstable eigenvalues are the respective eigenvalues with negative and positive real parts that are closest to the imaginary axis.

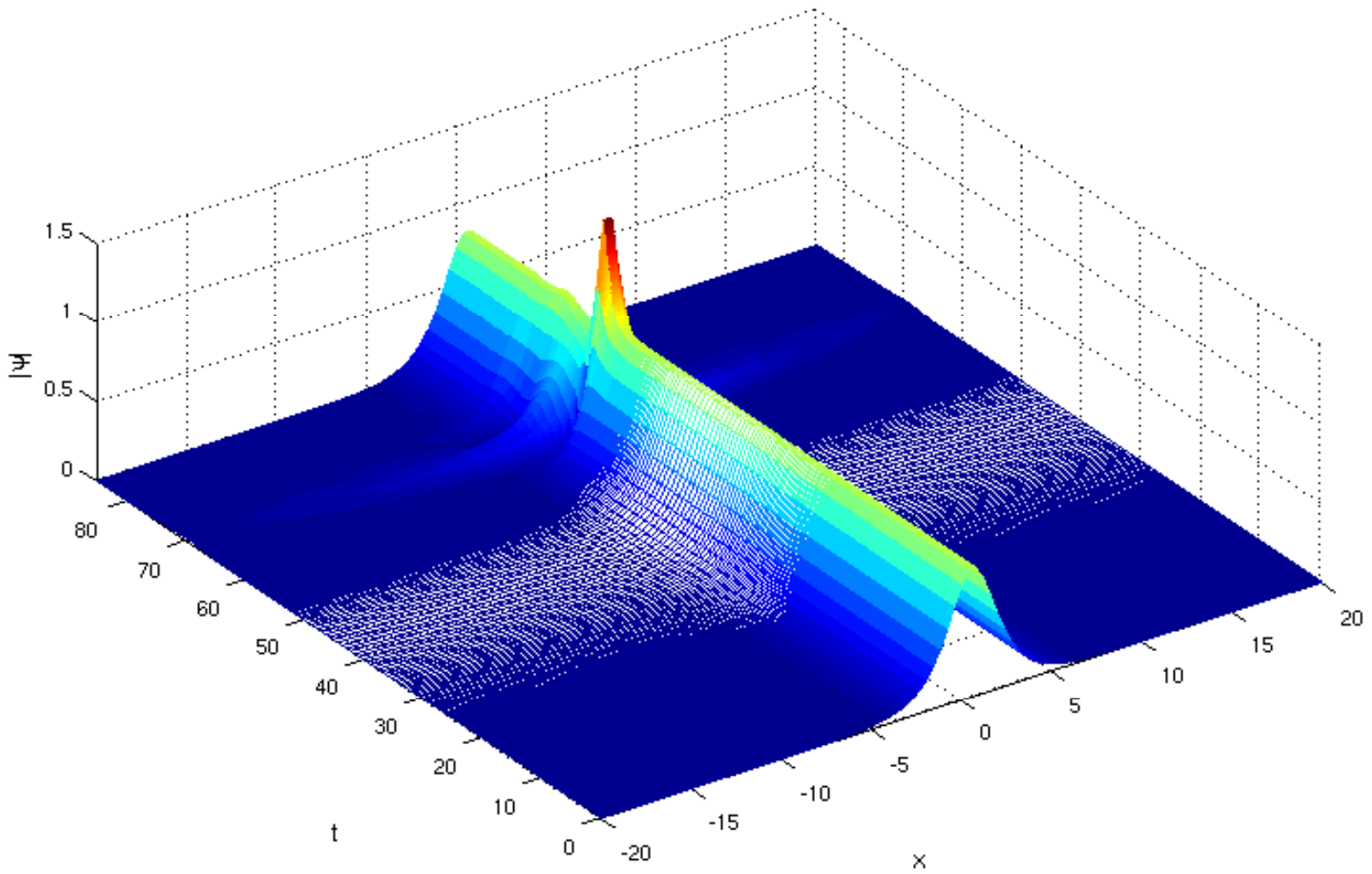

Figure 5.5: Absolute value of the periodic solution close to homoclinicity ($\gamma = 0.2$, $h = 0.385$ and $T = 85.10$). Only the central section $[-20, 20]$ of the full spatial interval $[-16\pi, 16\pi]$ is shown. The structure of the solution barely changes with increasing period T for large T, as is already clear in comparing Figures 5.5 and 5.3.

analogue of the saddle quantity satisfies

$$\widehat{\delta} = -\frac{\mathrm{Re}\lambda}{\mathrm{Re}\lambda_+} = \frac{\gamma}{\lambda_+} = 0.195 < 1/2.$$

Furthermore, the same structure is observed in the parametrically driven NLS bifurcation diagram (Figure 5.2) as predicted in §2.3 for $\delta < 1/2$. Numerical studies reveal that these moderately damped dynamics persist for $0.05 \lessapprox \gamma \lessapprox 0.25$ and we can conclude that the dynamics of the time-periodic solitons of the parametrically driven NLS for moderate damping are dominated by this interplay between the homoclinic solution and the stationary ψ_- soliton. That is to say that the phase space of the time-periodic solitons is organised around the homoclinic solution and the fixed point ψ_-.

The characteristic snaking structure of the bifurcation curve in Figure 5.2 might lead one to speculate that we are observing homoclinic snaking [16, 20, 21], or more specifically collapsed snaking [59] - the snaking curve narrows as the period T increases. Although originally studied in the Swift-Hohenberg equation and on the infinite line, homoclinic snaking has been identified and investigated in a wide variety of systems and on finite domains; case studies of snaking on finite domains are offered by Houghton and Knobloch [48] and Dawes [26] (see also [43]).

It is attractive to speculate that we are observing homoclinic snaking, as it would be a novel aspect of snaking, namely snaking of solutions (or states) in time. However, it is important to bear in mind that we are continuing periodic solutions and not two-dimensionally localised solutions, and furthermore, that no Maxwell point or curve indicating regions of bistability between two competing solutions exists.[‡] In fact, we are unable to even locate two competing solutions; only the ψ_- solution is an identifiable candidate.

5.2.1 Soliton complexes

We close this section with a brief observation about the soliton complexes in the parametrically driven NLS [10, 12]. Specifically, it is interesting to note that for moderate damping, the bifurcation curve of the periodic two-soliton complex is, up to scaling, exactly the same as the single-soliton solution bifurcation curve. This is illustrated in Figure 5.6. There, we have plotted the bifurcation curve of the single- and two-soliton complexes in terms of

[‡]As the parametrically driven NLS is neither a variational nor Hamiltonian system we have no energy integral of motion and therefore no means of extracting a Maxwell curve of any solution. Nevertheless, following [20, 68, 85] we may define, by analogy, the Maxwell point of our system to be the point where the homoclinic orbit connecting the stationary solution to itself becomes a pair of heteroclinic orbits between the stationary solution and a periodic or second stationary solution.

$L2$-norm defined as

$$\|\psi\| = \sqrt{\frac{1}{T}\int_0^T \sum_{i=-N}^{N} |\widehat{\psi}_n|^2},$$

with $\widehat{\psi}_n$ the Fourier coefficients (4.2). The single- and two-soliton complexes have the same (single peaked) temporal evolution over a single period and exhibit very similar bifurcation structures. So, although the parametrically driven NLS is nonlinear, the dynamics of the two-soliton complex are near identical to the dynamics of its constituent single-solitons.

5.3 Weak damping: $\gamma \leq 0.05$

Before analysing any results for the weakly damped system, it will be key to understand the effect of the finiteness of the spatial interval on the periodic soliton solution in detail. To do this we must first discuss the radiation from the periodic soliton.

5.3.1 Radiation from the oscillating soliton

The soliton is constantly attempting to maintain a balance between the energy fed into the system through the driving and the energy dissipated by the damping. Following [15] we can quantify this energy balance by considering the integral

$$N = \int_{-L/2}^{L/2} |\psi|^2 dx,$$

which in the context of waveguides, for example, measures the total power of light captured in the $(-L/2, L/2)$ section of the waveguide. The rate of change in the total power is given by

$$\dot{N} = 2h \int_{-L/2}^{L/2} |\psi|^2 \sin(2\theta) dx - 2\gamma N + \Phi \Big|_{-L/2}^{L/2}, \tag{5.1}$$

where ψ has been decomposed as $|\psi|e^{i\theta}$ and we have defined the flux

$$\Phi(x) = i\left(\psi_x \psi^* - \psi_x^* \psi\right).$$

The first term on the right-hand side of (5.1) gives the rate at which energy is pumped (or driven) into the soliton, while the second term represents the damping rate. The last term in (5.1) measures the radiation flux through the endpoints of the spatial interval.

The soliton therefore has two mechanisms for disposing energy, namely dissipating the energy over the core of the soliton and radiating the energy away. For strong and moderate damping the soliton is able to dissipate almost all of its energy over its core. As as the damping is decreased,

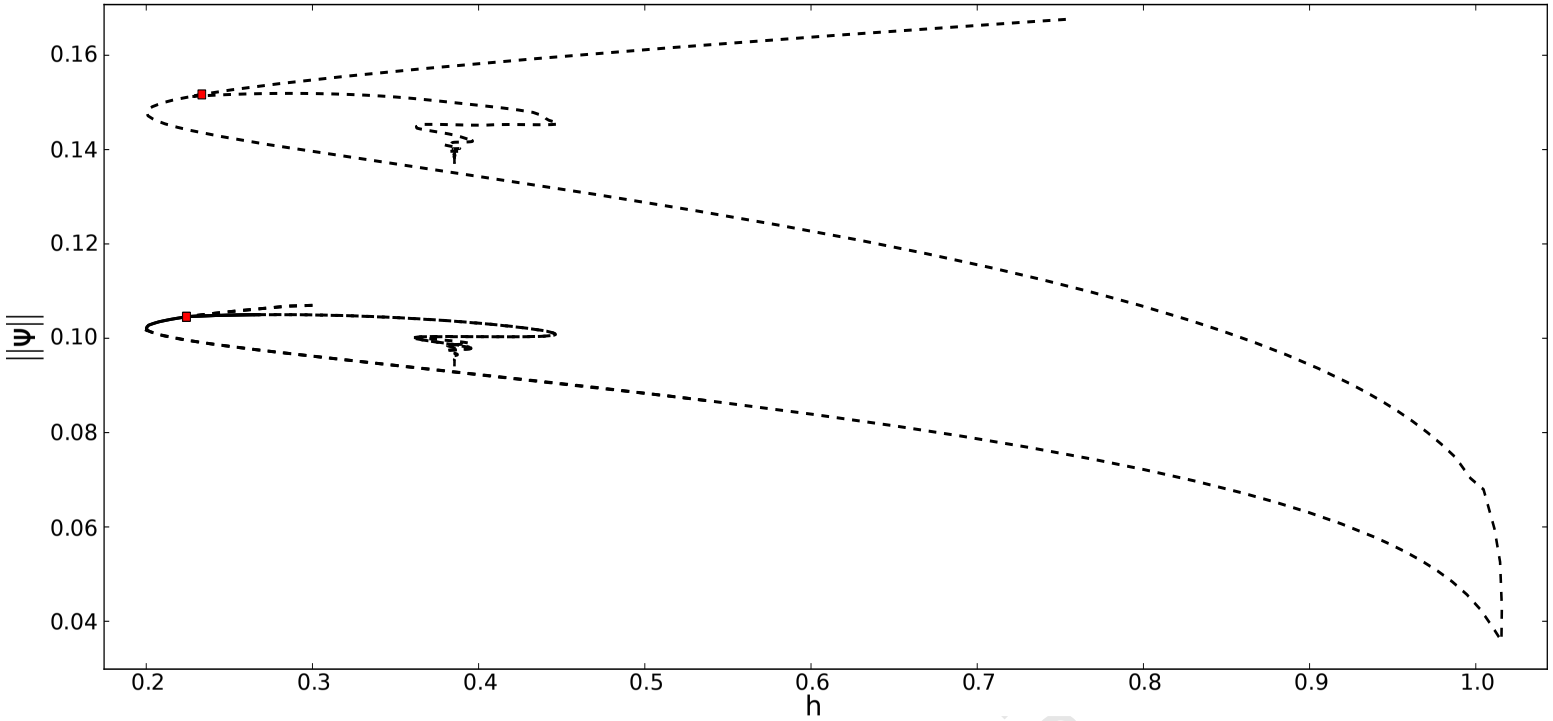

Figure 5.6: Bifurcation diagram of the stationary and periodic single- and two-soliton complex with $\gamma = 0.2$. The top curve corresponds to the soliton complex and the bottom curve to the single-soliton. The periodic solitons are born at the Hopf bifurcation points (indicated by the red squares) and snake downwards as they approach the homoclinic solution. Presumably larger soliton complexes consisting of three and more constituent solitons would have the same bifurcation structure and lie above the two-soliton complex curve.

however, the soliton can no longer dissipate enough of its energy over its core and it must find an alternative energy-draining mechanism, to wit: the long-range radiation. The radiation through the endpoints $x = \pm L/2$ is governed by the linearisation of the parametrically driven NLS (1.3) whose dispersion relation is

$$(\omega - i\gamma)^2 = (k^2 + 1)^2 - h^2. \tag{5.2}$$

The soliton will sustain radiation waves with frequencies $\omega = 2\pi n/T$, $n = 1, 2, \ldots$, where T is the period of the soliton. Thus we take ω to be real in the dispersion relation (5.2). For real ω then, equation (5.2) has two pairs of complex roots $k = \pm(p_{1,2} + iq_{1,2})$, with imaginary components

$$q_{1,2} = \sqrt{\frac{1}{2} \pm \frac{\mathcal{S}}{2} + \frac{1}{2}\sqrt{1 + 2(\mathcal{Q} + \mathcal{S})}}, \tag{5.3}$$

where

$$\mathcal{S} = \sqrt{\mathcal{P} + \mathcal{Q}}, \quad \mathcal{Q} = \sqrt{\mathcal{P}^2 + \gamma^2\omega^2}, \quad \text{and} \quad 2\mathcal{P} = h^2 - \gamma^2 + \omega^2.$$

The decay rate q_1 is always greater than q_2 and accounts for the rapidly decaying core of the soliton. Outside the core, q_2 is the dominant decay rate and the solution has a long oscillatory tail decaying as $e^{-q_2|x|}$.

It is useful to define the quantity

$$\sigma(\omega) = \sqrt{\omega^2 + h^2 - \gamma^2} - 1. \tag{5.4}$$

σ gives us information about the frequency of the radiation. For weak damping (γ small) the expression (5.3) can be simplified and we have, in particular,

$$\begin{aligned} (\sigma > 0) \quad & q_2 \to \frac{\omega/2}{1+\sigma}\sqrt{\frac{\gamma}{\sigma}}\sqrt{\gamma} \quad \text{as} \quad \frac{\gamma}{\sigma} \to 0; \\ (\sigma < 0) \quad & q_2 \to \sqrt{-\sigma} \quad \text{as} \quad \frac{\gamma}{\sigma} \to 0. \end{aligned}$$

Thus, for weak damping, when σ is positive the exponent q_2 is small, whereas when σ grows to large negative values q_2 grows as well. Hence $\sigma(\omega)$ indicates whether the long-range radiation with frequency ω can be excited (q_2 small) or not (q_2 large).

So, for weak damping, if the period T of the solution is small enough for the quantity $\sigma(\omega)$, with $\omega = 2\pi/T$, to be positive then the decay rate q_2 is small and the radiation flux is *not* exponentially small. In this case we say that the first-harmonic radiation is *not* blocked. As we climb the snaking curve the period increases and eventually σ will become negative and q_2 will grow to values of order 1. The flux is exponentially damped in this case and the first-harmonic radiation will be mostly suppressed at the extremities

of the soliton. However, $\sigma(\omega)$ with $\omega = 4\pi/T$ will still be positive so that the radiation tails will now be dominated by the second -harmonic radiation. Once the second-harmonic is blocked, the third-harmonic will take over, and so on.

Clearly, the second-harmonic radiation is present not only when the first-harmonic radiation is suppressed. However, the amplitude of the radiation typically scales as ϵ^n for the nth harmonic [15] so that the second-harmonic flux is far weaker when both channels are open.

5.3.2 Finite spatial intervals and fine structure

In discussing the strongly and moderately damped systems, we were able to approximate the infinite spatial interval with a finite interval because the soliton solution remained fully localised. In those damping regimes, our finite approximation of the infinite line was valid because the soliton dissipated very little energy as radiation; it was able to dissipate a sufficient amount of energy over its core. Almost no activity occurs away from the core of the soliton and the extremities of the solution are, in essence, of little consequence.

Indeed, we recall that the radiation waves decay as $e^{-q_2|x|}$ where q_2 is given by (5.3). And for large γ, q_2 is also large so that the radiation waves decay quickly over a short range $|x|$. As γ decreases, however, q_2 decreases and the radiation waves travel over a greater range. In terms of energy dissipation, the soliton must dissipate *more* energy as radiation to balance the energy input through the parametric driving. Thus there is an important connection between the spatial interval length L and the damping γ: with smaller γ we need a larger L to approximate the infinite interval sufficiently. Naturally, for larger spatial intervals we require more Fourier modes to ensure an accurate discretisation of the spatial mesh. Clearly then, it is computationally infeasible to increase L indefinitely. We are forced to shift the focus of our study for weakly damped periodic solutions.

The infinite interval interpretation was originally adopted simply because it simplifies the analytics of the stationary soliton analysis. The distinction between infinite and finite intervals was not important in our study of the strongly and moderately damped regimes because the finite interval gave an excellent approximation to the infinite interval anyway. But in truth, a paradigm shift to studying solutions on a finite interval is in fact rather natural. This is because an infinite spatial interval is not physically realisable. In a similar manner, we may argue that a very large interval is of less interest than a smaller finite interval.

The upshot of this is that we need to bear in mind that the results gathered in this section on the weakly damped system pertain to (temporally and spatially) periodic solutions defined on a finite interval. That is, solutions defined on a ring. It is worthwhile exploring in more detail the respective

effects of decreasing γ and changing L on the soliton solutions.

Figures 5.7 and 5.8, which show the bifurcation curves for various small γ but fixed L, give us the first look at the dynamics of the parametrically driven NLS for weak damping. The location of the Hopf bifurcation points correlate excellently with the perturbation expression for $\gamma \ll 1$ derived by Aleexeva, Barashenkov and Pelinovsky [2],

$$h_{\mathrm{HB}} = 0.063596 + 0.76013\gamma^2. \tag{5.5}$$

Studying the bifurcation curves we first note that the large-scale snaking structure persists for weak damping. The fact that the large-scale snaking structure persists, indicates that the Shil'nikov dynamics - the interaction between the homoclinic solution and the fixed point ψ_- - continue to play an important role in the organisation of the phase space of parametrically driven NLS for $\gamma = 0.05$. However, as γ is decreased, fine structure begins to emerge. Furthermore, decreasing γ results in the growth of new regions where stable periodic solution exist. Clearly, the weakly damped dynamics of the parametrically driven NLS on the ring can no longer simply be explained by the interaction of the homoclinic orbit and the saddle-focus fixed point ψ_-.

We pause to emphasize that the fine structure exhibited in Figures 5.7 to 5.9, and indeed in all numerical simulations in this section, is a robust feature: it persists when the number of Fourier modes is increased (or decreased), the temporal mesh is refined or the error tolerances are decreased. That is to say that the fine structure is *not* simply a numerical artifact.

Fixing now $\gamma = 0.01$, we can study the effect of varying L. The results are shown in Figure 5.9. The oscillations in the fine structure change shape and location as L is changed. For larger spatial intervals the fine structure oscillates with decreasing amplitude - the oscillations are confined to thinner channels. On the other hand, for smaller spatial intervals, the fine structure oscillates with increasing amplitude. Comparing Figures 5.7 and 5.8 to Figure 5.9 we see that the effect of increasing L is similar to the effect of increasing γ in that it dissipates the fine structure - compare the $\gamma = 0.05$ panel in Figure 5.7 with the $L = 256\pi$ panel in Figure 5.9. We also note that the large-scale snaking structure is largely unaffected by changes in the spatial interval length or damping. This is particularly apparent away from the fine structure where there is less radiation ($T \approx 13$ in Figures 5.7, 5.8 and 5.9).

The decreasing amplitude of the fine structure oscillations over larger spatial intervals, gives us a glimpse into the dynamics of the periodic solitons on the infinite line in the weakly damped system. Evidently, on the infinite line there would be no fine structure and only the regular snaking curve. In the case of the infinite spatial domain then, the weakly damped dynamics of the time-periodic solitons of the parametrically driven NLS would again be

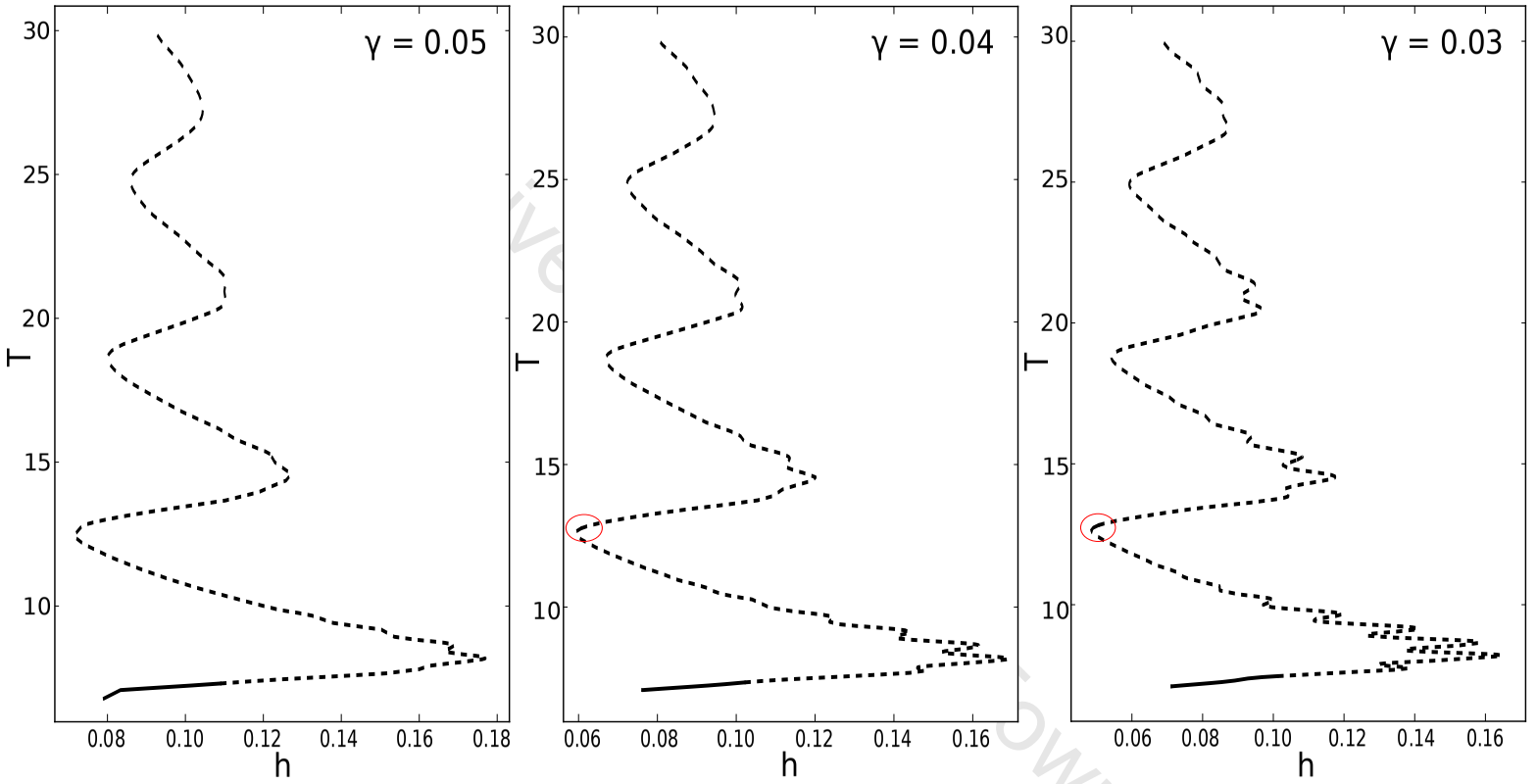

Figure 5.7: Bifurcation curves of periodic solitons for weak damping ($0.03 \leq \gamma \leq 0.05$). The fine structure along with new regions of stability (marked by open red circles) begin to proliferate within the large-scale structure at $\gamma \approx 0.04$. Period-doubling bifurcations are not shown. Smaller γ bifurcation curves are shown in Figure 5.8.

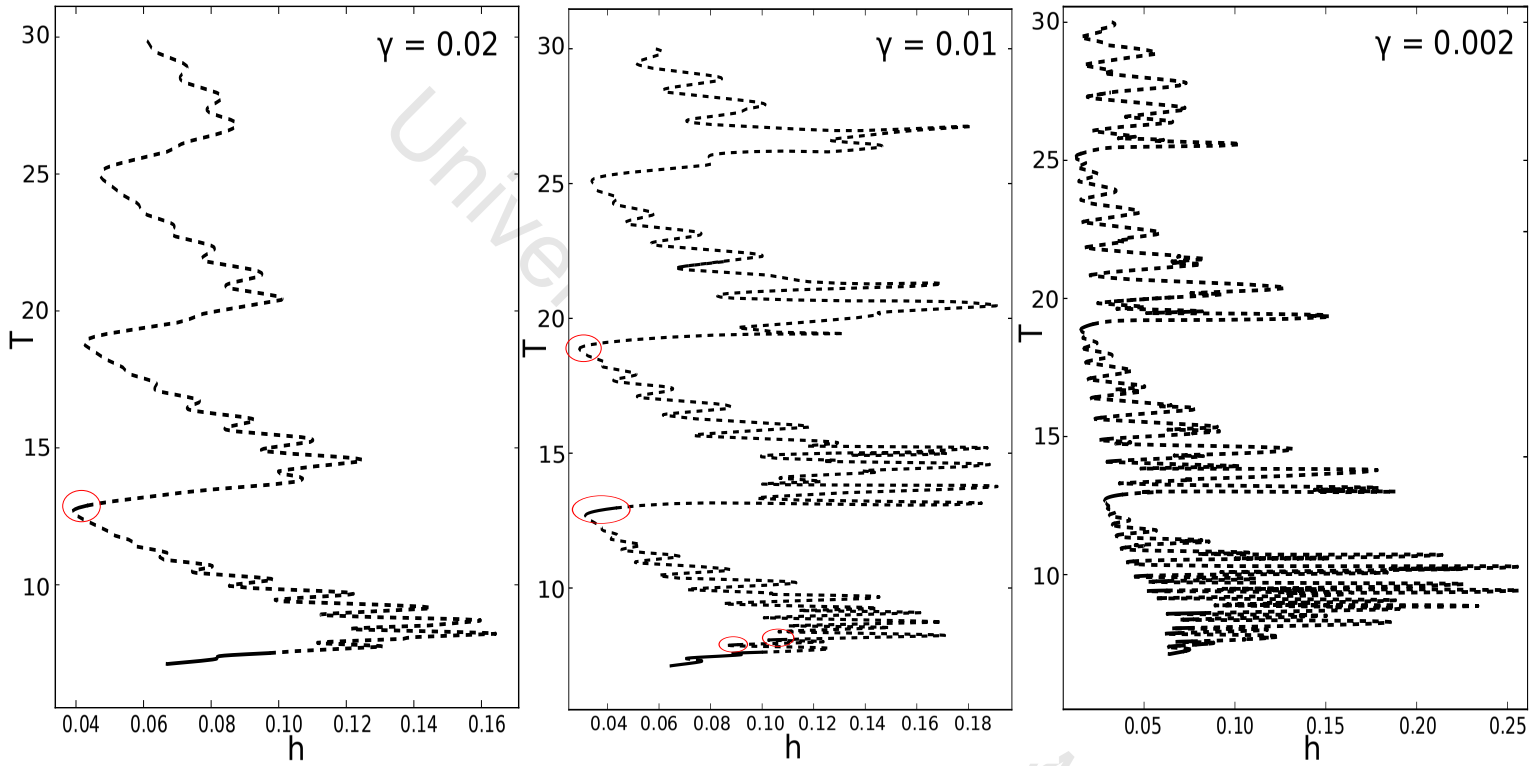

Figure 5.8: Bifurcation curves of periodic solitons for weak damping ($0.002 \leq \gamma \leq 0.02$). New regions of stability are marked by open red ellipses for $\gamma = 0.02$ and 0.01. For $\gamma = 0.002$, new regions of stability are *not* marked, but appear along nearly every left hand turning point of the fine structure. Period-doubling bifurcations are not shown.

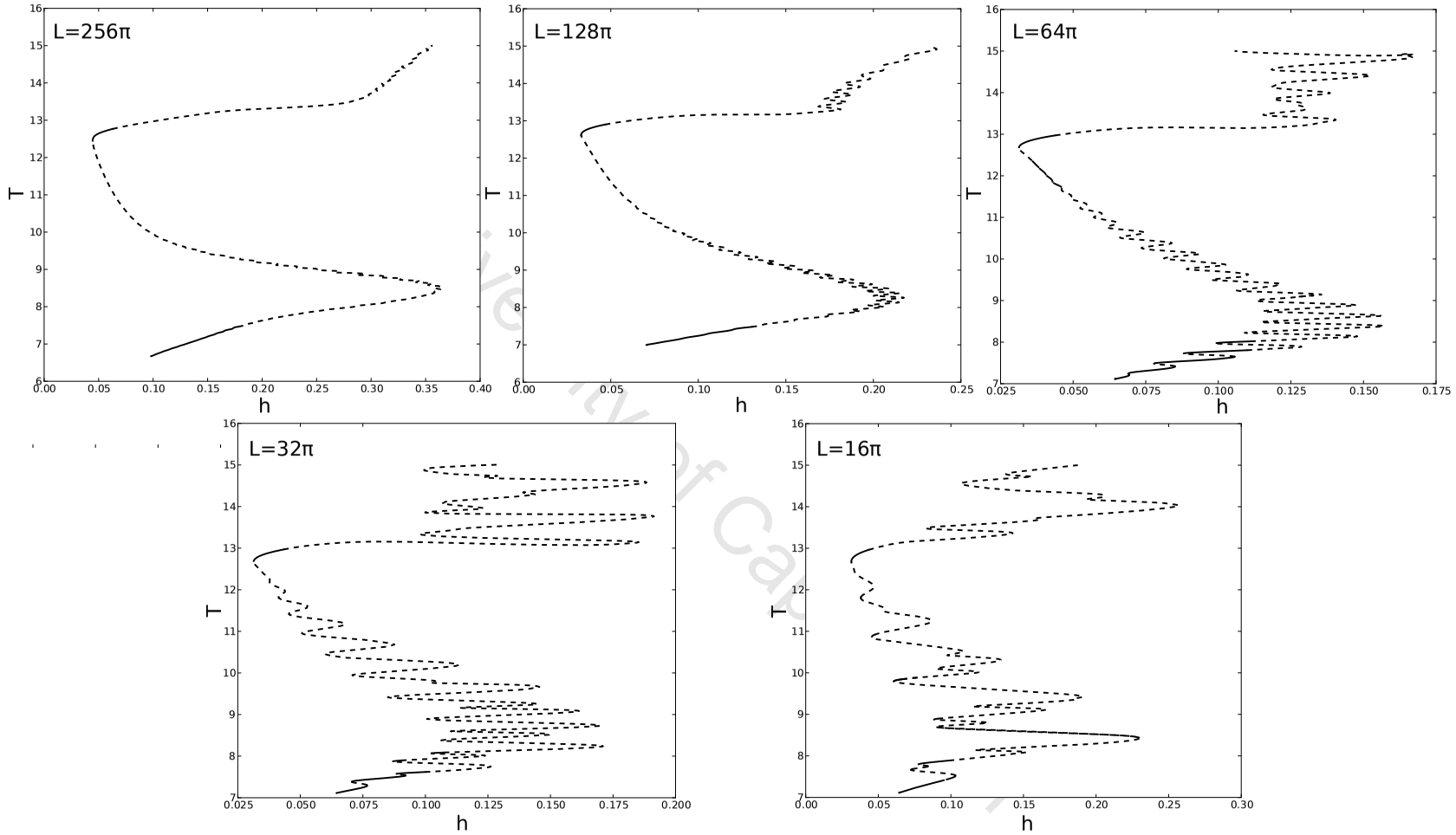

Figure 5.9: Bifurcation curves for various spatial interval lengths L with fixed $\gamma = 0.01$. For large L the oscillations in the fine structure are confined to smaller channels than for small L. In comparing the above plots to those in Figures 5.7 and 5.8, note that these plots only show solutions with periods $T \leq 15$, whereas the plots in Figures 5.7 and 5.8 show solutions with periods $T \leq 30$.

dominated by the interaction of the homoclinic orbit and the saddle-focus fixed point ψ_-.

The joint absence of fine structure and radiation in the moderately damped regime along with the observation that increasing L dissipates the fine structure is indicative that the radiation is the key factor giving rise to the fine structure. This is further exemplified by the fact the solutions located in the regions of parameter space where fine structure is present (cf. Figure 5.10) are surrounded by large-amplitude radiation waves, whereas solutions located in regions absent of fine structure (such as the solution shown in Figure 5.11) sit on a very small amplitude radiation wave background.

This begs the question as to why certain solutions have conspicuously little radiation? Indeed, from §5.3.1 we know that for weak damping the soliton dissipates large amounts of energy through radiation and thus we would expect the soliton to be surrounded by radiation waves. This lack of radiation at certain characteristic solution points can be understood in terms of which radiation channels are open. Panel (b) of Figure 5.12 gives the radiation indicator σ of the second-harmonic for small periods as a function of the driving strength parameter h. σ crosses through zero near the red dot solution. Here then, the second-harmonic becomes blocked. Because the second radiation channel is no longer available the soliton sheds less radiation. As we climb the bifurcation curve further to larger periods the frequency of the oscillating soliton decreases and the higher harmonics become a more and more viable means of dissipating energy.

To confirm which harmonics are most active in the fine structure we can directly measure the dominant frequencies in the radiation spectrum at several characteristic solution points along the bifurcation curve. The results are tabulated in Table 5.1. As expected from the positivity of σ (cf. panel (b) in Figure 5.12), the dominant harmonic is typically the second harmonic, with the exception of a few solutions points (12-13 and 16-17) highlighted in boldface where the second-harmonic is evidently suppressed.

Studying the relative contribution of the second most dominant harmonic to the dominant harmonic ($|Y_2/Y_1|^2$) we note that the second-harmonic is only slightly suppressed for the solution points 12-13. For solution points 16-17 on the other hand, the second-harmonic is completely suppressed. Moreover, solution points 16-17 lie on the shortest branch within the fine structure (cf. panel (a) of Figure 5.12).

We already have some idea of how the spatial interval length L affects the fine structure, but is worthwhile investigating in detail how varying L will affect the radiation itself. To study the dependency of the radiation on L, we continue characteristic solution points located within the fine structure in L. Figure 5.13 shows the ratio of the spatial interval length L to the wavelength of the radiation λ as measured directly using the FFT for a particular solution point. Remarkably, $m = L/\lambda$ remains locked exactly to an integer value. The fact that m is integer valued holds true for *all*

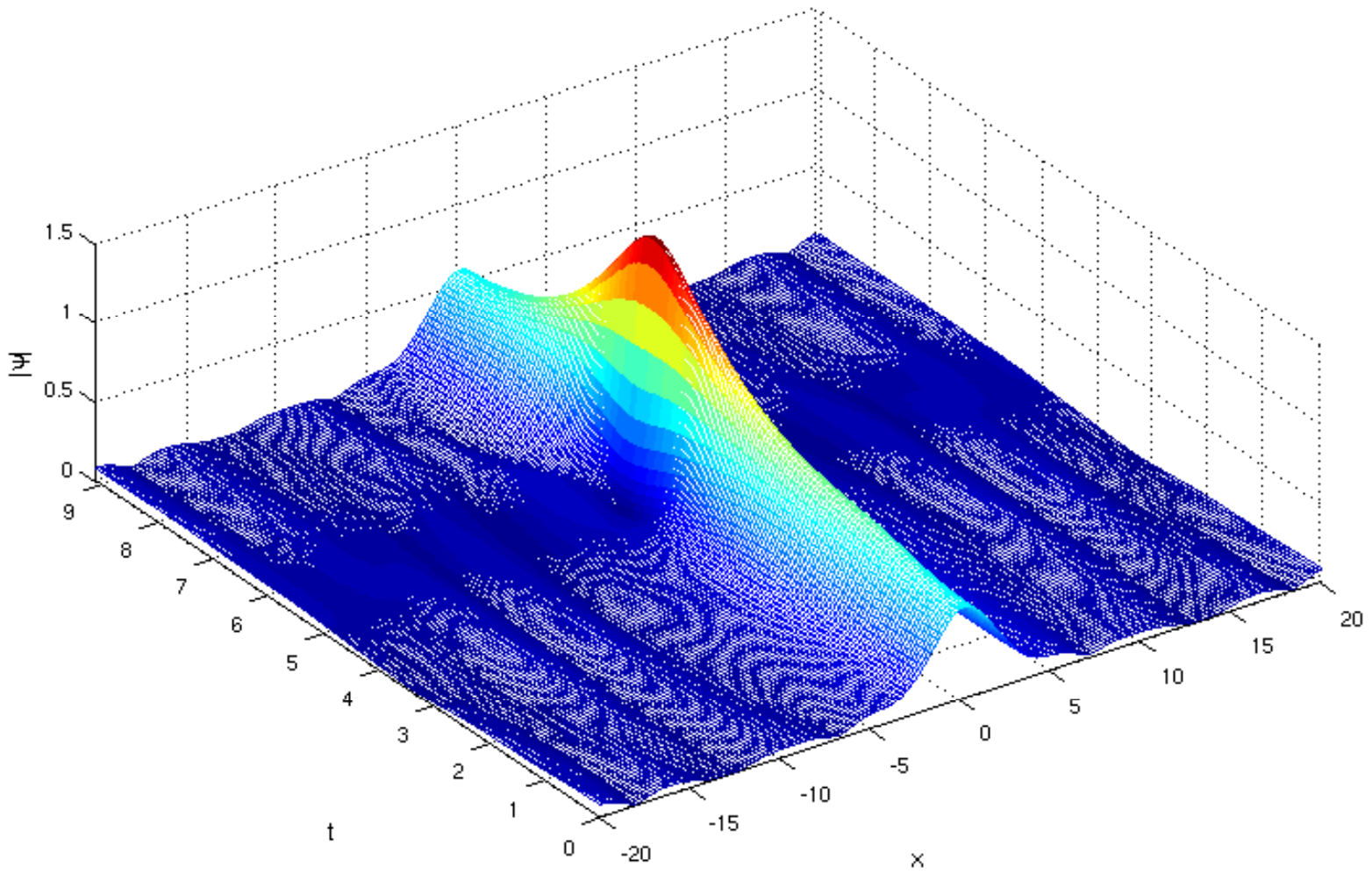

Figure 5.10: Absolute value of the periodic soliton with $\gamma = 0.01$, $h = 0.161$ and $T = 9.08$ (blue dot in panel (a) of Figure 5.12). Only the central section $[-20, 20]$ of the full spatial interval $[-16\pi, 16\pi]$ is shown. In contrast to solutions in the moderately damped regime (cf. Figure 5.3) and to solutions located in regions on the bifurcation curve absent of fine structure (cf. Figure 5.11), the soliton pictured here is surrounded by large-amplitude radiation waves.

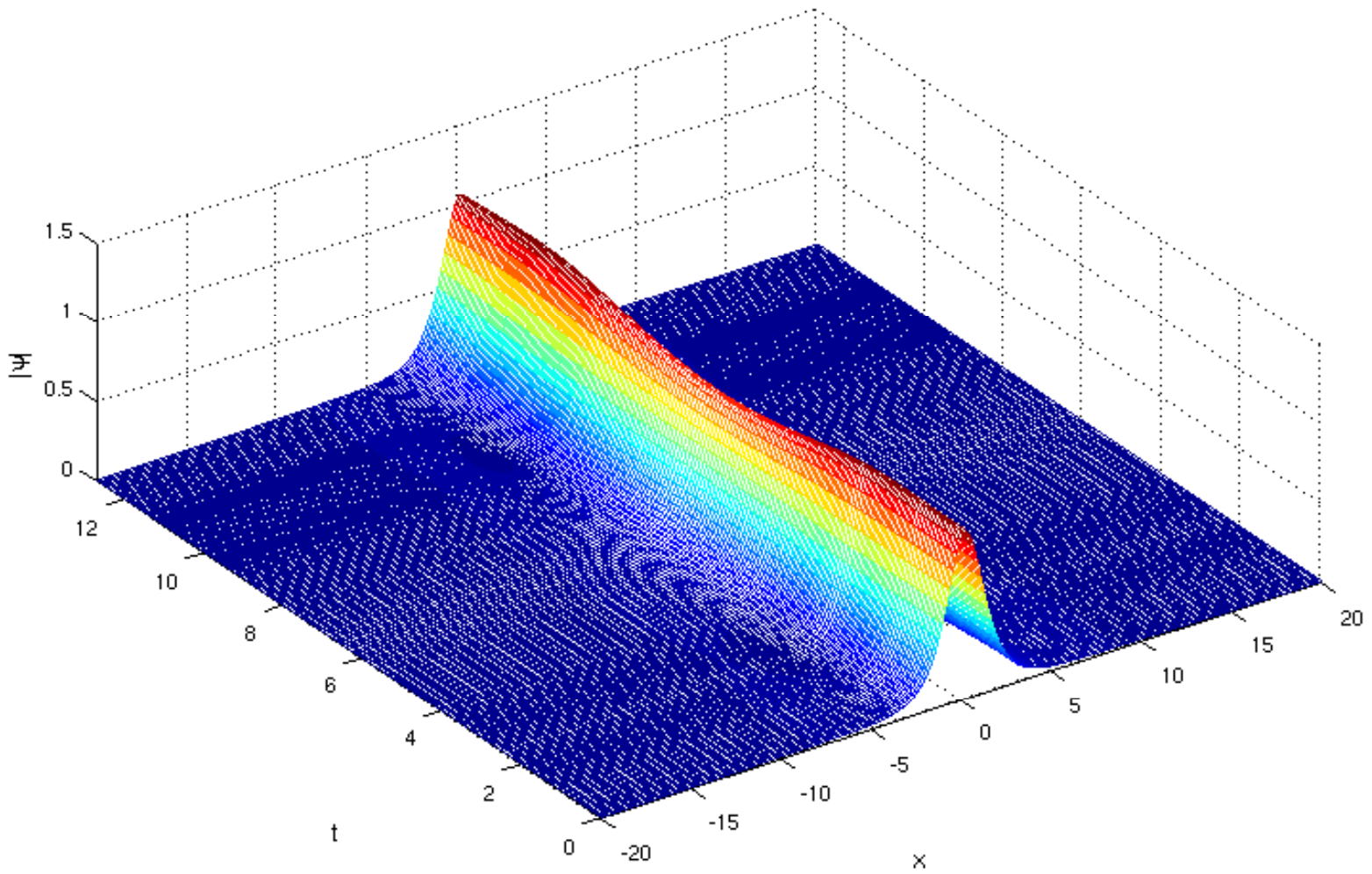

Figure 5.11: Absolute value of the periodic soliton with $\gamma = 0.01$, $h = 0.031$ and $T = 12.69$ (red dot in panel (a) of Figure 5.12). Only the central section $[-20, 20]$ of the full spatial interval $[-16\pi, 16\pi]$ is shown. In comparison to Figure 5.10, the radiation waves here are barely visible.

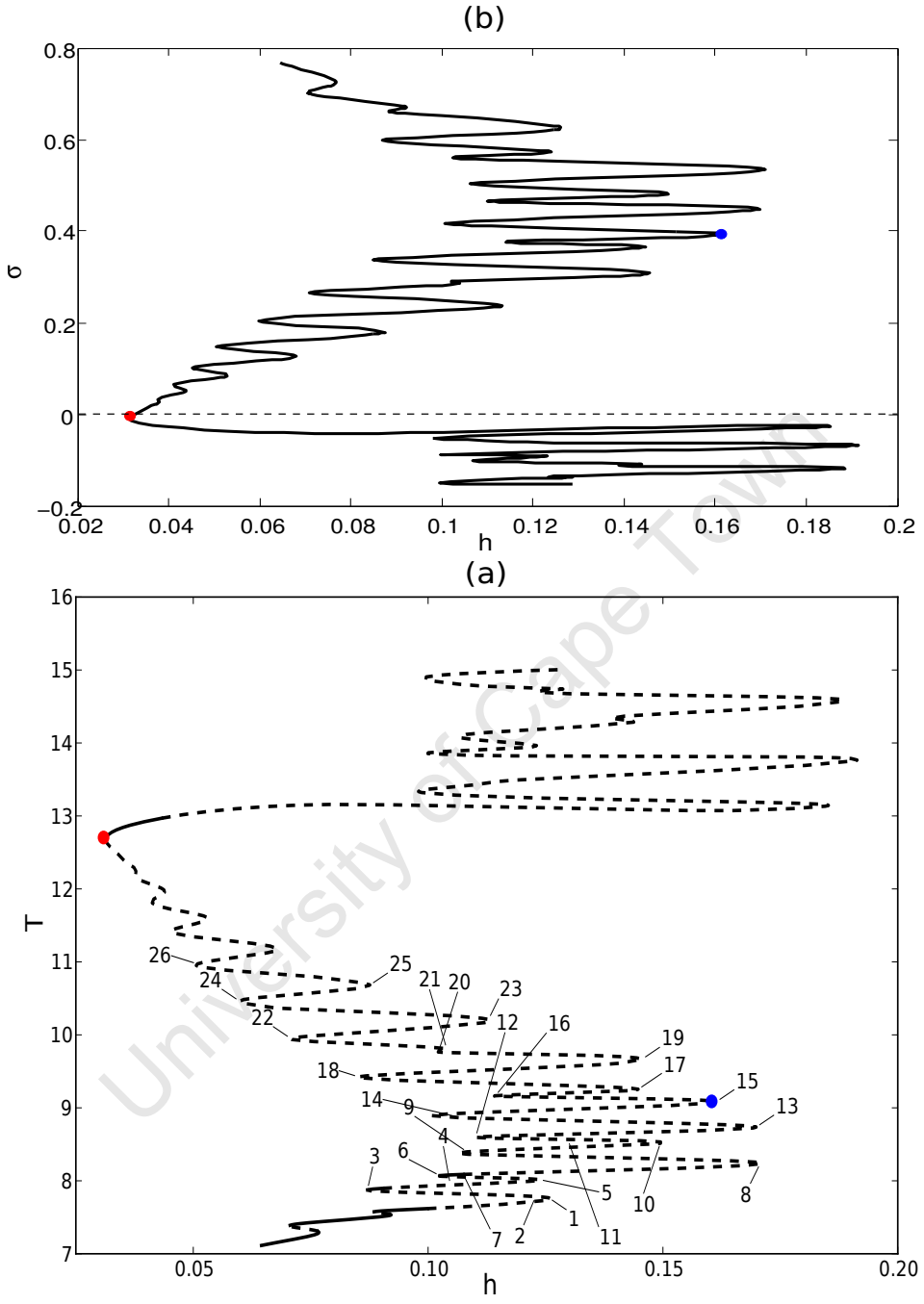

Figure 5.12: (a) Bifurcation diagram of periodic solitons for small periods ($T \leq 15$) with $\gamma = 0.01$. Representative solutions denoted by the blue and red dots are shown in Figures 5.10 and 5.11 respectively. The labelled solution points are referenced in Table 5.1. Period-doubling bifurcations are not shown. (b) The radiation indicator σ of the second-harmonic ($\omega = \frac{4\pi}{T}$) for solutions along the bifurcation curve in (a). As we follow the bifurcation curve in (a) upwards, the σ curve snakes downwards.

Solution	Ω_1	Ω_2	Ω_3	$\lvert\frac{Y_2}{Y_1}\rvert^2 \times 100\%$	$\lvert\frac{Y_3}{Y_1}\rvert^2 \times 100\%$
1	2	3	4	16	1
2	2	3	4	19	3
3	2	3	4	24	7
4	2	3	4	40	14
5	2	3	4	67	29
6	2	3	5	5	23
7	2	3	5	5	23
8	2	3	4	26	6
9	2	3	4	18	4
10	2	3	4	15	7
11	2	3	4	58	23
12	**3**	2	4	84	41
13	**3**	2	4	85	42
14	2	3	4	39	15
15	2	3	4	24	7
16	**3**	4	1	34	8
17	**3**	4	5	55	8
18	2	4	6	10	4
19	2	3	4	14	4
20	2	3	4	36	23
21	2	4	5	10	19
22	2	3	6	21	19
23	2	3	4	24	7
24	2	1	3	28	19
25	2	3	1	25	19
26	2	3	4	32	6
27	2	3	1	41	19

Table 5.1: Summary of radiation frequency data. Solution numbers correspond to solution labels in panel (a) of Figure 5.12. Ω_1, Ω_2 and Ω_3 are respectively the first, second and third most dominant harmonics as measured from the frequency spectrum; and $|Y_2/Y_1|^2$ and $|Y_3/Y_1|^2$ give the contributions of the second and third most dominant harmonics relative to the dominant harmonic as measured by their spectral densities.

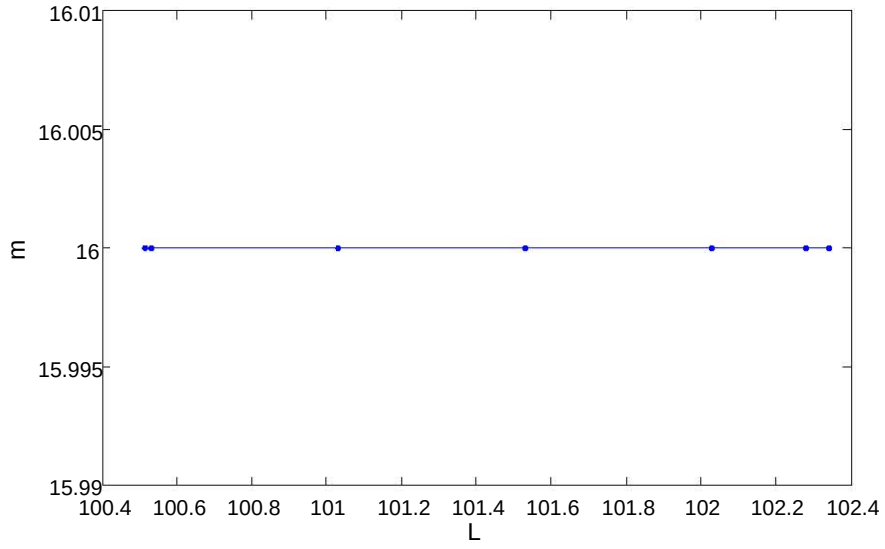

Figure 5.13: The ratio of the spatial interval length to the wavelength of the radiation, $m = L/\lambda$, for a particular characteristic solution (blue dot in Figure 5.12). $m = 16$ to within numerical accuracy.

of the characteristic solutions studied, both within and away from the fine structure.

Although it is not distinguishable from Figure 5.10, a study of the time evolution of the spatial profile of the radiation waves for solution points located within the fine structure reveal that they are in fact standing waves. Thus the ratio $m = L/\lambda$ tells us how many wavelengths are fitted into the spatial interval. Note also that the solution only exists over a small range of L. Evidently, the number of wavelengths is fixed. However, when the same continuation exercise is performed for solution points away from the fine structure (for example the red dot in panel (a) of Figure 5.12) we find that the solution is defined over far larger range of L. Evidently for characteristic solution points within the fine structure, where the radiation wave amplitude is large, the solution "locks" onto an integer value m, whereas for characteristic solutions away from the fine structure the radiation wave amplitude is small enough to allow the solution to jump between integer values of m.[§]

The fact that m is exactly integer valued is very curious. If the soliton were not present then we would indeed expect m to be integer valued because we have to fit an integer number of radiation waves onto the (spatial) ring.

[§]There are a few exceptional characteristic solutions located within the fine structure for which the solutions manage to "jump" to another integer value. For such solutions the radiation amplitude is smaller and only one "jump" is ever observed.

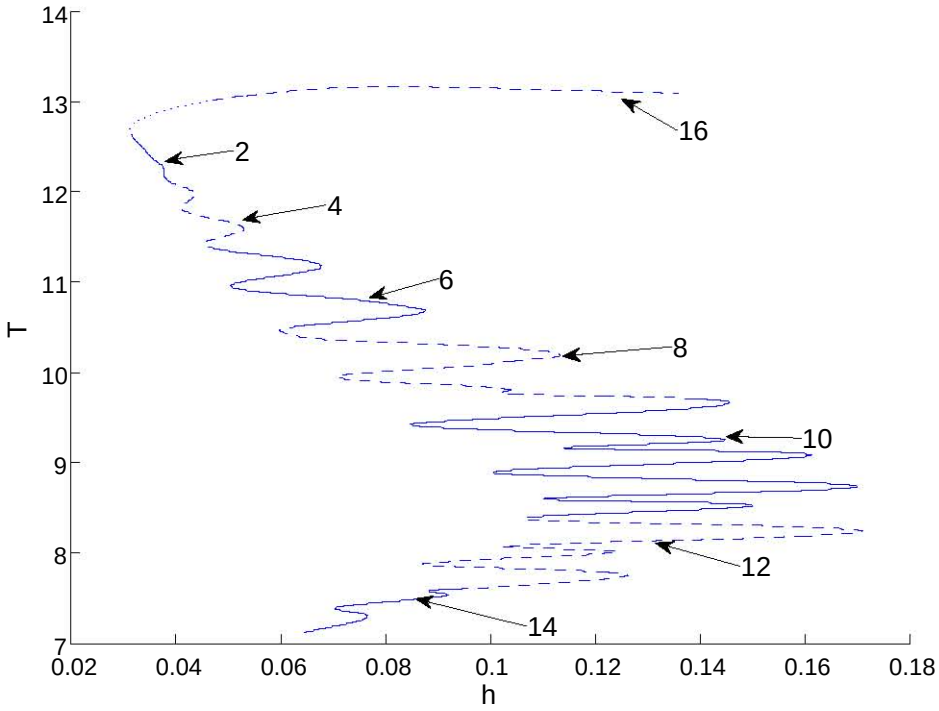

Figure 5.14: Integer values of $m = L/\lambda$ along the bifurcation curve with $L = 32\pi$ and $\gamma = 0.01$ fixed. Each arrow and integer pertains to the whole segment of the respective solid or dashed line. As we climb the bifurcation curve the number of wavelengths decreases steadily, until we reach $T \approx 13$ (dotted line) where the second-harmonic radiation becomes blocked and the radiation amplitude is too small to be precisely measured. From here the cycle then restarts with the third-harmonic now being the most dominant radiation channel.

It is as if the soliton is keeping perfectly in step with the radiation. In fact further study of the spatial profile of the full periodic solution reveals that this is indeed true: the soliton width, call it l, and the radiation wavelength λ are roughly the same size, $l \sim \lambda$. The "wavelength" of the soliton matches that of the radiation and together, the soliton and its radiation, fit very neatly onto the ring that is their spatial domain.

The linear dispersion relation (5.2) allows us to make a qualitative prediction about how m should vary along the bifurcation curve. From equation (5.2) we know that $\omega \sim k$ implying that $T \sim \lambda$ and therefore that $m \sim 1/\lambda \sim 1/T$. As we climb the bifurcation curve to larger periods, m should take smaller integer values.

This rule turns out to be roughly true as illustrated by Figure 5.14, where we have demarcated the *approximate* regions with the same integer values

m along the bifurcation curve. The plot is only approximate because we have removed smaller anomalous regions where m jumps around somewhat erratically. Naturally, we should not expect exact agreement as the basis for this prediction, the linear dispersion relation (5.2), was derived on the assumption that the amplitude of the background radiation was negligible.

Figure 5.14 presents another curious fact: the number of wavelengths fitted into the spatial interval, $m = L/\lambda$, is always even. We speculate that this curiosity is related to the periodic geometry of the spatial domain and the spatial symmetry of the solution $\psi(-x,t) = \psi(x,t)$ (cf. §4.1.1). However, the details of this are presently beyond our understanding.

The full details of how m varies along the bifurcation curve is shown alongside the average radiation intensity $\langle\ |\psi|^2\rangle$ in Figure 5.15. $\langle\ |\psi|^2\rangle$ is a measure of the average amplitude of the radiation over a fixed spatial length and over one full period,

$$\langle\ |\psi|^2\rangle = \frac{1}{T}\frac{1}{L/4}\int_0^T \int_{L/4}^{L/2} |\psi|^2 dx dt. \tag{5.6}$$

Bearing in mind that the spatial interval is as $[-L/2, L/2]$, only integrating over the $(L/4, L/2)$ therefore ensures that we only average over the radiation waves and not the soliton core.

Figure 5.15 illustrates how $\langle\ |\psi|^2\rangle$ mimics the fine structure oscillations of the bifurcation curve. For each turning point along the radiation intensity curve, there is a corresponding turning point along the bifurcation curve within the fine structure. Furthermore, the radiation intensity is greatest at the middle of the first fine structure bunch ($T \approx 9$) and very small where there is no fine structure ($T \approx 13$). Naturally, we would expect *some* correlation between the driving strength h and $\langle\ |\psi|^2\rangle$ because, for weak damping, most of the energy input through the driving is dissipated through the radiation flux. But the fact that the correlation is so close corroborates our previous hypothesis that it is precisely the large-amplitude radiation waves that are producing the fine structure along the bifurcation curve.

Thus, taking the large-scale snaking structure and the fine scale structure into account, we see that the bifurcation structure of the parametrically driven NLS in the weakly damped regime is governed by a compromise between the dynamics that dominate the moderately damped system, namely the interplay of the homoclinic solution and the fixed point ψ_-, and the large-amplitude radiation waves. For stronger damping γ or larger spatial domains L, the radiation intensity is smaller and the Shil'nikov dynamics fully describe the bifurcation structure of the time-periodic solitons (as illustrated by the $\gamma = 0.05$ panel in Figure 5.7 and the $L = 256\pi$ panel in Figure 5.9). Then, as we decrease γ or L, the radiation intensity increases and the fine structure proliferates along the large-scale snaking structure (as

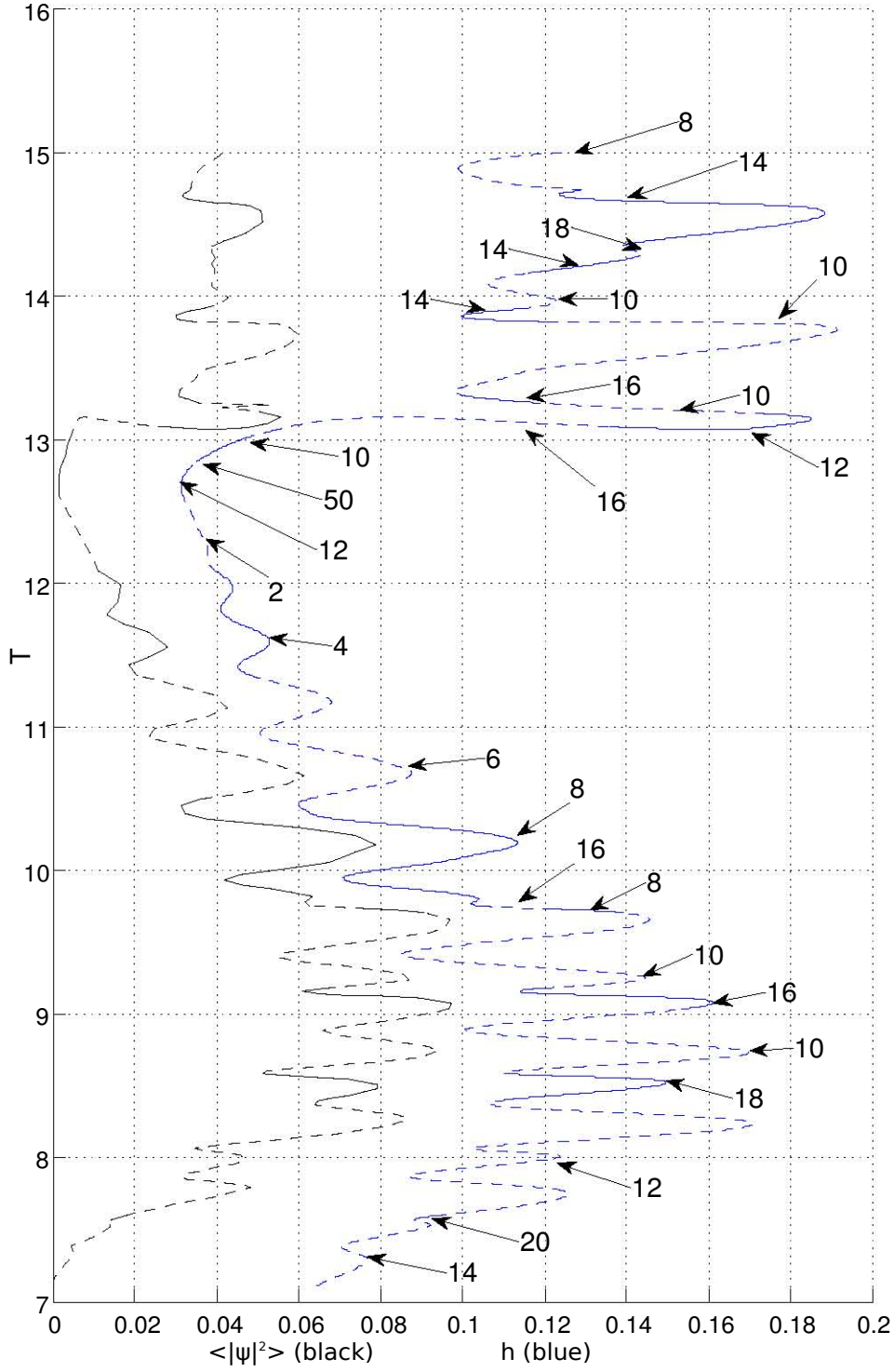

Figure 5.15: Integer values of $m = L/\lambda$ along the bifurcation curve with $L = 32\pi$ and $\gamma = 0.01$ fixed. Each arrow and integer pertains to the whole segment of the respective solid or dashed line.

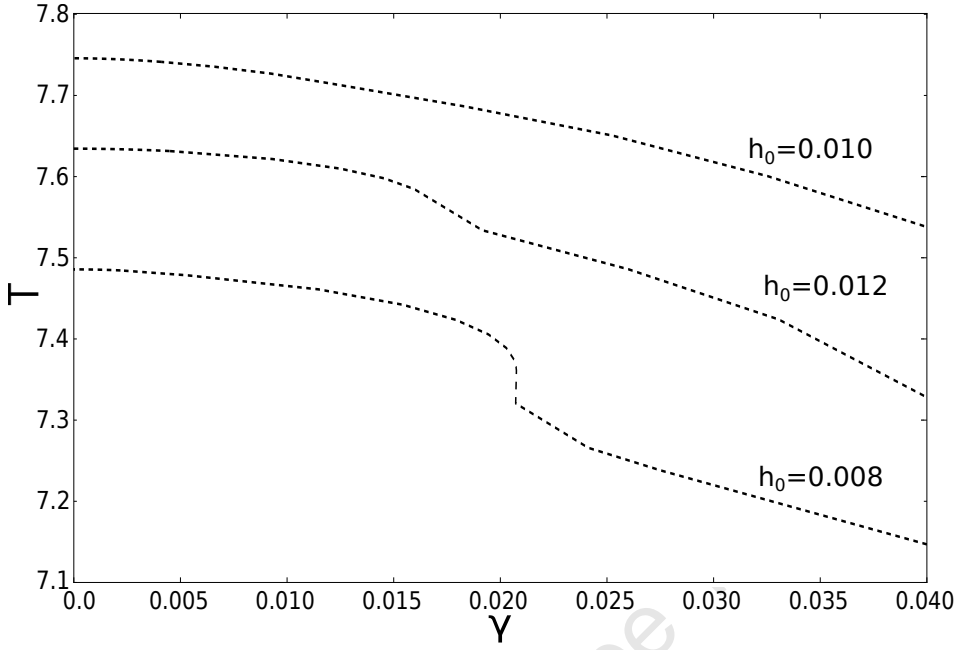

Figure 5.16: Bifurcation curves for the undamped time-periodic soliton with $L = 32\pi$ for several fixed driving strengths h_0.

exemplified by the $\gamma = 0.01$ and 0.002 panels in Figure 5.8 and the $L = 32\pi$ and 16π panels in Figure 5.9).

We have observed that the large amplitude radiation waves (Figure 5.15) and the geometry of the spatial interval (Figure 5.9) are closely linked to the presence of the fine structure. These two key factors led us to speculate that a more complete understanding of the exact mechanism causing the fine structure oscillations lies in first understanding why the number of wavelengths fitted into the spatial interval, m, are exactly *even integer* valued.

5.3.3 Zero damping $\gamma = 0$

Using an asymptotic multi-scale expansion Alexeeva, Barashenkov and Pelinovsky [2] were able to show that no periodic solution exists on the *infinite* line for the undamped parametrically driven NLS. Their analytics showed that, in the undamped case, any temporally periodic soliton would be suppressed by radiation. This conclusion was verified by direct numerical simulation.

On the *finite* periodic interval, however, undamped periodic soliton solutions do exist. By numerically continuing damped periodic solutions through decreasing γ we were able to obtain undamped periodic solutions for various fixed initial driving strengths h_0. The results of this continuation, for several

h_0 \ L	0.08	0.010	0.012
32π	$[0.081, 0.090]$	$[0.091, 0.104]$	$[0.124, 0.126]$
64π	$[0.073, 0.094]$		
128π	$[0.078, 0.087]$		

Table 5.2: Range of driving strengths h over which the undamped periodic soliton exists for various initial driving strengths h_0 (from which the continuation in γ was initiated) and spatial interval lengths L.

fixed driving strengths h_0, are shown in Figure 5.16 . A typical undamped solution is included in Figure 5.17

Having obtained the undamped solution for fixed h_0, we can then continue the solution in h with γ fixed to zero. This computation revealed that the undamped solution only exists over a very small range of driving strengths h and, furthermore, that this domain of existence depended on both the driving strength h_0 from which the continuation in γ was initiated and the spatial interval length L. Table 5.3.3 summarizes the results for various initial h_0 and L.

5.3.4 New regions of stability

Comparing the bifurcation curve for moderate damping ($\gamma = 0.2$), Figure 5.2, to the bifurcation curve for the $\gamma = 0.05$ shown in the first panel of Figure 5.7, we note that in both cases the only stable solutions are found near the beginning of the respective bifurcation curves where the period is small. However, as γ is decreased from $\gamma = 0.05$ down to $\gamma = 0.04$ (middle panel in Figure 5.7), a new stable region emerges at the second turn of the large-scale snaking curve. Further decrease in γ down to $\gamma = 0.01$ (middle panel in Figure 5.8 and reproduced in panel (b) of Figure 5.12) results in the appearance of several more stable regions. All these new stable regions appear for small driving strengths h along the left-hand turns of the large- and fine-scale structure of the bifurcation curve.

The reported stability for several γ was verified by direct simulation using the Fourier split-step method (cf. §4.1.2). The results of a particular simulation are shown in Figure 5.18.

The emergence of new regions of stability is of great interest as they are physically realisable states in systems modelled by the parametrically driven NLS. Moreover, the weak damping regime is arguably more physically relevant than the other damping regimes. For example, the parametrically driven NLS finds application in modelling nonlinear optical phenomena [27, 57, 63] and the technology there is geared towards engineering lasers and optical fibres that are as dampless as possible - when sending optical

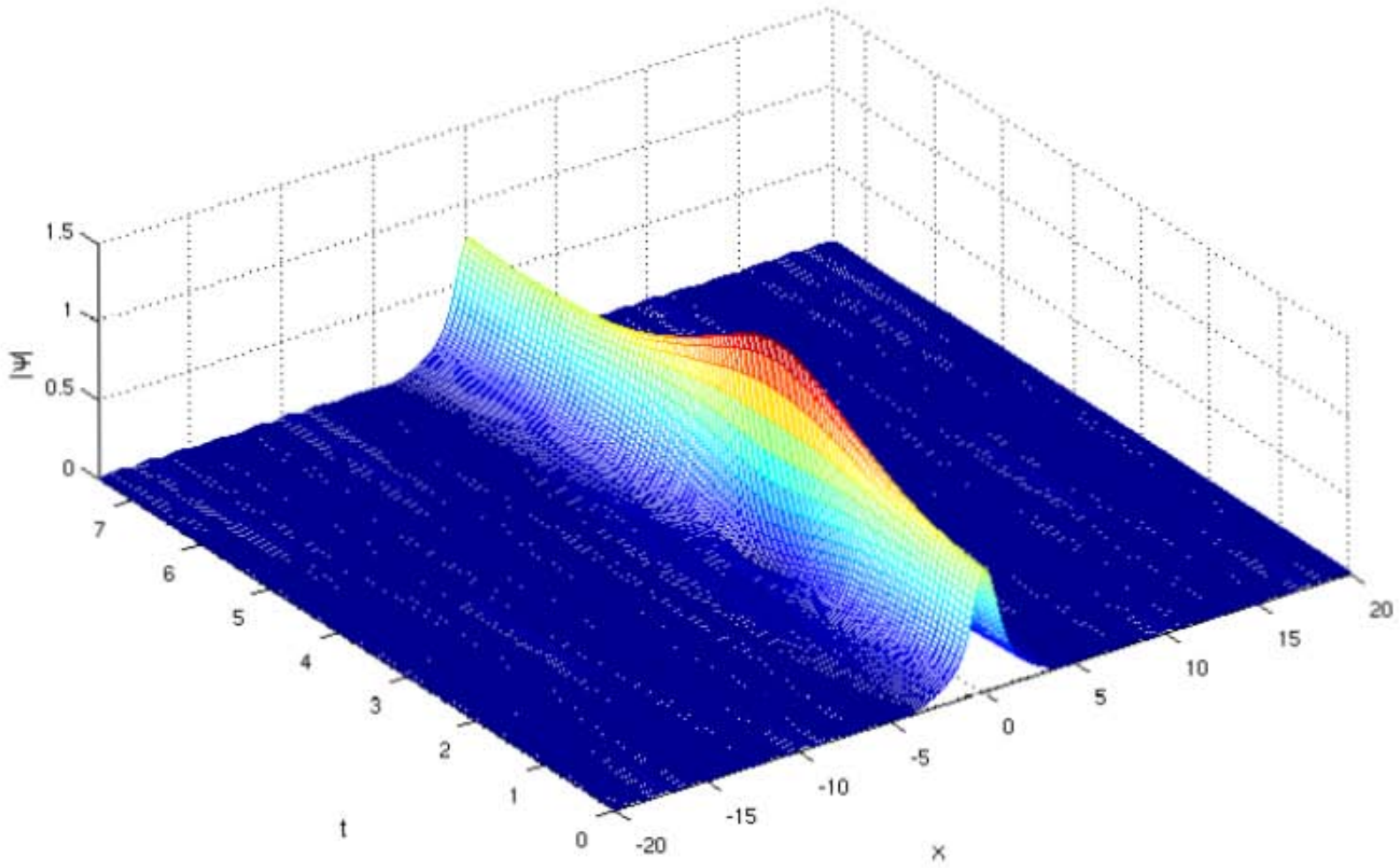

Figure 5.17: Undamped periodic soliton solution for $h = 0.082$ and $T = 7.49$. Only the central section $[-20, 20]$ of the full spatial interval $[-16\pi, 16\pi]$ is shown.

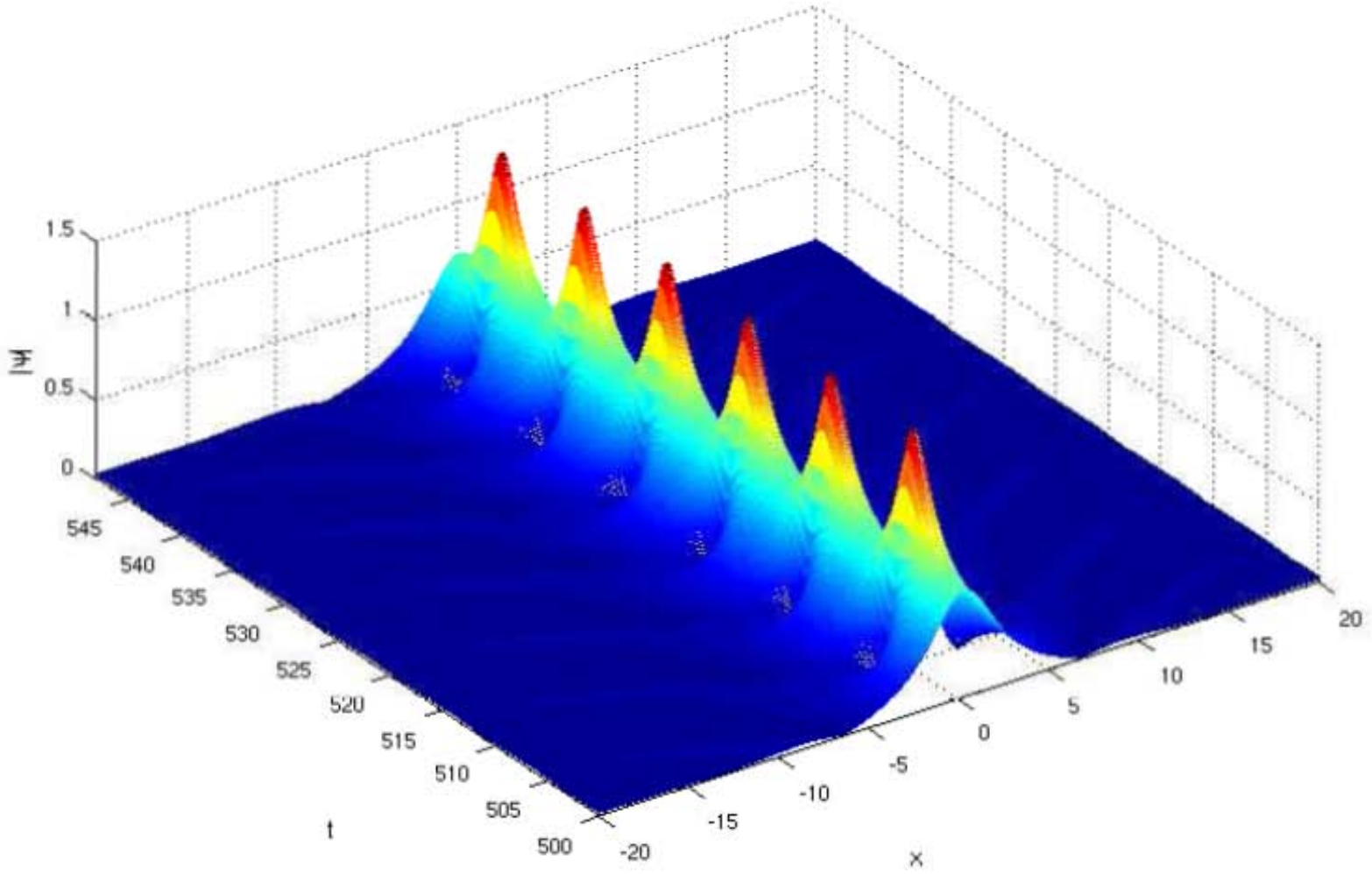

Figure 5.18: Simulated stable solution with $\gamma = 0.01$, $h = 0.107$, and $T = 8.09$ for large times. Several periods are shown. Only the central section $[-20, 20]$ of the full spatial interval $[-16\pi, 16\pi]$ is included.

pulses over long distances we want to suppress damping. Otherwise put, we are interested in wave motion which is not possible when a system is overdamped.

Figures 5.7 and 5.8 reveal that the appearance of new regions of stability is correlated with the growth of fine structure - new regions of stability appear as the fine structure proliferates. On the other hand, the $L = 256\pi$ panel in Figure 5.9 shows that while the fine structure oscillations in the bifurcation curve dissipate for large L, the new regions of stability persist. Thus, while it seems likely that the mechanism creating the fine structure is giving periodic solutions associated with small driving strengths h their increased stability, the exact details are not clear. Nevertheless, it is hoped that, with a more complete understanding of how the large-amplitude radiation waves on a periodic spatial interval give rise to the fine structure, we will gain a better understanding of the new regions of stability.

The stability of the solutions in (h, γ) parameter space is neatly summarised by the "Feigenbaum tree" shown in Figure 5.19. The stability diagram highlights the appearance and then the subsequent growth of the pockets of stability as we decrease the damping.

5.4 Bifurcation diagram

Bondila, Barashenkov and Bogdan [18] constructed the existence and stability chart for the parametrically driven NLS soliton solutions on the plane of the two control parameters, the driving strength parameter h and the damping coefficient γ, by directly simulating the system over a discrete range of the parameter values; this chart was reproduced in Figure 1.1. Barashenkov, Zemlyanaya and van Heerden [15] later reconstructed the attractor chart, shown in Figure 1.2, using numerical continuation. More precisely, looping through a discrete range of γ, they continued the soliton solutions in h and then pieced together the attractor chart using interpolation. Because both attractor charts were constructed from a finite number of discrete solution points and bifurcation points they remain only approximate. We supplement and refine both these charts by continuing the one-parameter bifurcation curves for the Hopf and period-doubling bifurcations and the approximate locus of the homoclinic orbit. Our attractor chart is shown in Figure 5.20.

Our construction of the single-soliton attractor chart was carried out as follows. The locus of the Hopf and period-doubling bifurcations were computed by first continuing our solution in h (with γ fixed) until the point of bifurcation; and then following the locus of the bifurcation in h *and* γ as described in §3.3.5. Similarly, the approximate locus of the homoclinic orbit was computed by fixing the period T (with T large) of the periodic solution and continuing the solution in h *and* γ. The results are denoted by

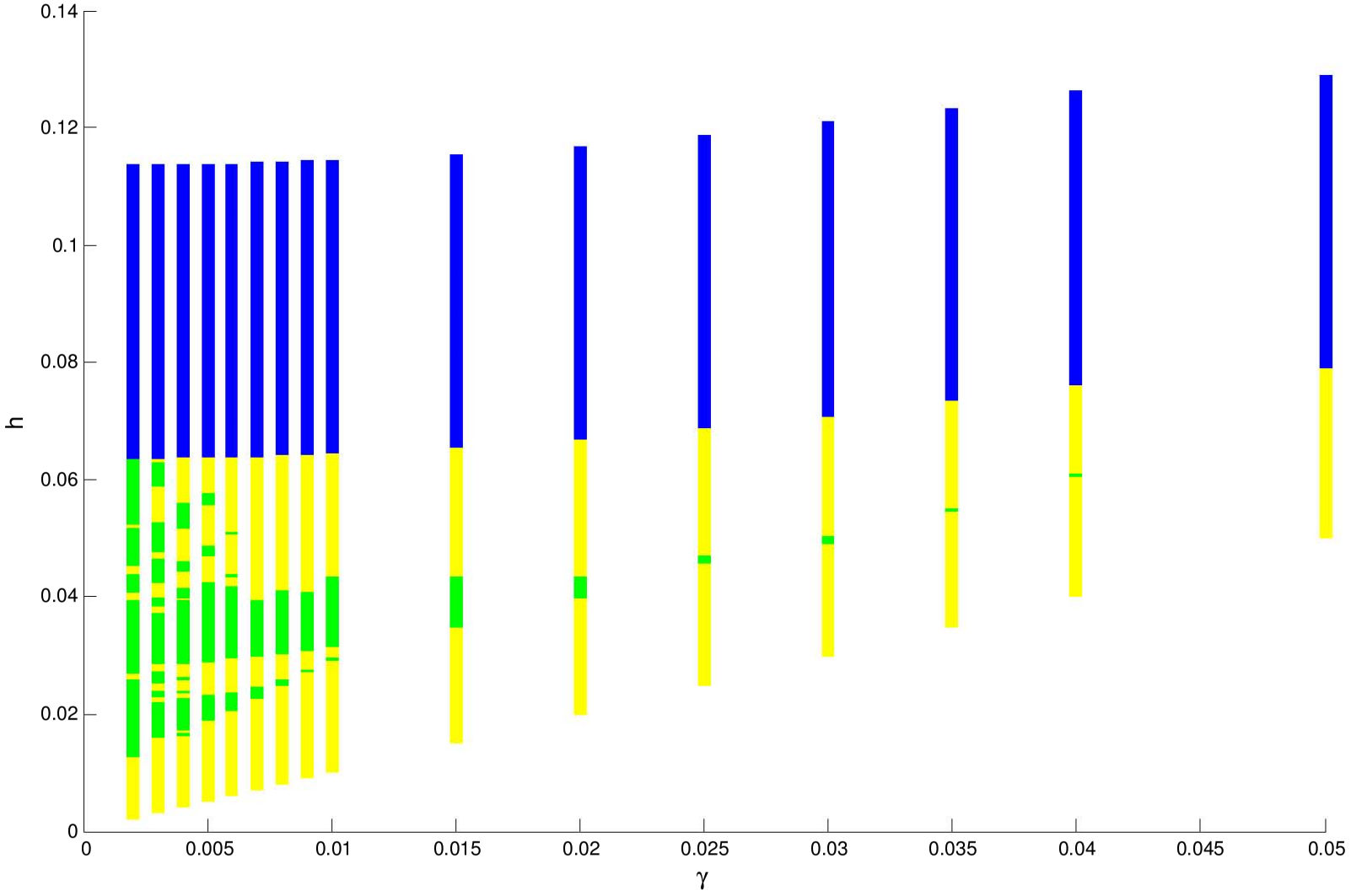

Figure 5.19: Stability chart highlighting the domain of existence of the nontrivial attractors in (h, γ) parameter space for $L = 32\pi$. Stable time-periodic solitons are shown in blue while stable stationary solitons are shown in yellow. Cases of bistability, where stable time-periodic and stable stationary solitons coexist, are shown in green.

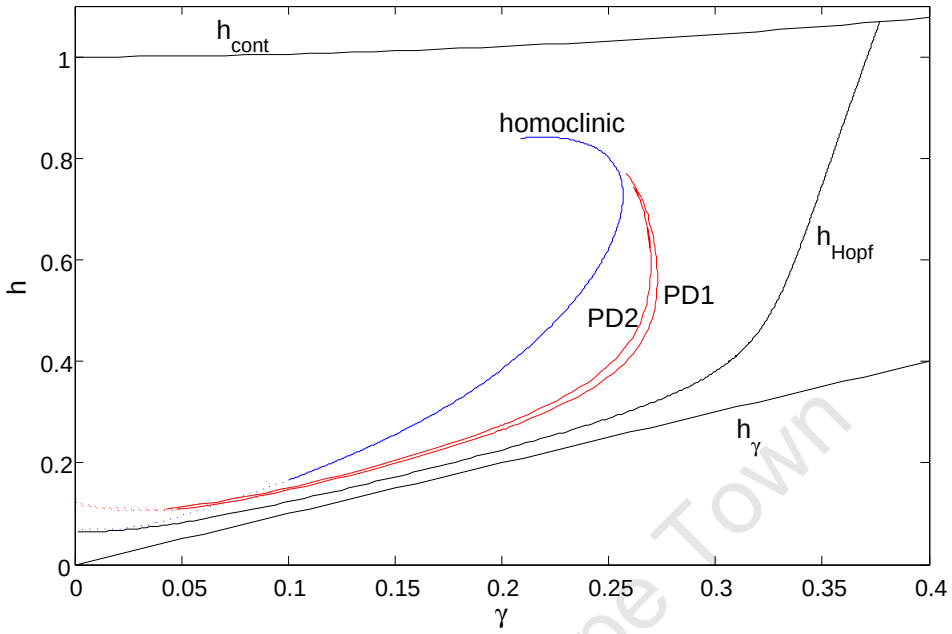

Figure 5.20: Single-soliton attractor chart of the parametrically driven NLS. h_{Hopf}, h_γ and h_{cont} denote the Hopf, $h = \gamma$ and $h = \sqrt{1+\gamma^2}$ (1.6) curves respectively; PD1 and PD2 are the respective period-doubling bifurcation curves of the period-one and period-two solitons; and the curve describing the approximate homoclinic orbit is also labelled. The solid bifurcation curves (h_{Hopf}, PD1, PD2 and homoclinic) were traced out by numerical continuation. The dotted curves were obtained by interpolation of a finite number of discrete bifurcation points. Further details are given in the text.

the respective solid curves in Figure 5.20.

Between the h_{Hopf} and $h_\gamma = \gamma$ curves the only nontrivial solutions are the stationary solitons $\psi_\pm$ (1.4), whereas between the h_{cont} and h_{Hopf} curves both stationary and periodic solitons coexist. Inside curve PD1, period-two solitons are found and inside curve PD2, period-four and higher period solitons are also found. The locus of the approximate homoclinic solution represents a set of special periodic solutions.

As already discussed in detail, for small γ the interval length becomes an important factor. Specifically, as γ decreases and the fine structure proliferates, it is difficult to track the locus of points corresponding to the period-doubling bifurcations. We are forced to increase the spatial interval and the number of Fourier modes for small γ. Eventually this becomes computationally infeasible. Thus, the locus of period-doubling bifurcations for $\gamma \leq 0.04$ has been interpolated from discrete bifurcation points. That is to say, for weak damping, we continued our periodic solution in h under

an increased resolution (a larger number of Fourier modes) until the point of the period-doubling bifurcation for several fixed γ and then interpolated these discrete bifurcation points. The interpolation curve is denoted by the dotted red curves in Figure 5.20.

The (approximate) locus of points corresponding to the homoclinic solution is also affected by the fine structure for weak damping. In addition to this, for small γ, to obtain a good approximation of the homoclinic solution with a *finite-period* periodic solution we must go to larger and larger periods. Because of these hindrances, we opted to interpolate the (approximate) locus of the homoclinic orbit from discrete homoclinic solution points for $\gamma \leq 0.1$, as we did for the period-doubling bifurcation. The resulting interpolation curve is denoted by the dotted blue curve in Figure 5.20.

The fact that the locus of period-doubling bifurcations and the approximate homoclinic orbit cross at $\gamma \approx 0.07$ is not alarming, as the homoclinic orbit need not necessarily lie inside the period-doubling curves. To understand this it is important to recall that homoclinic solution is simply the large-period limit of the periodic solution. Demanding that the homoclinic orbit lie inside the period-doubling is tantamount to the (incorrect) assumption that the homoclinic solution is the limiting case of successive period doubling bifurcations of the periodic solution.

Chapter 6

Continuation of Directly Driven NLS Soliton Solutions

The focus of our study in this chapter will be on the temporally periodic solitons of the directly driven NLS. We investigate solutions typical of three different damping regimes, namely strong damping ($\gamma = 0.2$), moderate damping ($\gamma = 0.15$), and weak damping ($\gamma = 0.01$). In addition we examine the domain of existence of the stationary solitons $\psi_{\pm}$ (1.15). Finally, we conclude the chapter by presenting the bifurcation diagram in (h, γ) parameter space.

The bifurcation curves in each of the damping regimes of the directly driven NLS show many parallels with their counterparts in the parametric case. Naturally, this is largely expected as the systems are very closely related. Nevertheless, the different driving mechanisms do manifest slightly different dynamics.

In the case of strong and moderate damping in directly driven NLS, we will encounter several soliton complexes. With the exception of §5.2.1, this thesis has only been concerned with single-soliton solutions. That said, the soliton complexes in the strongly and moderately damped system arise naturally and any study of the single-soliton solutions in these regimes is incomplete without an analysis of the arising soliton complexes. To paraphrase [15]: the soliton complexes play a key role as phase space organisers in the directly driven NLS.

6.1 Domain of existence of stationary solitons

As discussed in §1.2, due to the lack of analytical bounds, the sizes of the domains of existence of the directly driven NLS stationary $\psi_{\pm}$ solitons (1.15) are not firmly established. However, previous investigations [7] suggest that the domain is likely finite. In an effort to investigate the domain size, we numerically continued the $\psi_{\pm}$ solitons alternately in h and γ.

From the outset we must accept that we can only ever answer this question within numerical accuracy. Put differently, even if the numerics suggest a finite domain size, it is possible that the domains are in fact infinite, albeit vanishingly thin for larger h and γ as in the case of the parametrically driven NLS stationary ψ_- soliton (1.4). Nevertheless, a good indicator of the verity of the numerical results is how the results differ when we increase the numerical accuracy.

We begin our investigation with the stationary ψ_- soliton. We could simply employ our standard Fourier expansion approach to continue the time-independent ψ_- solution. This approach simply amounts to solving the algebraic system given by setting the left-hand side of system (4.26) to zero. While this method will work, transforming the time-independent directly driven NLS (an ODE) into a system of algebraic equations is more work than is necessary. More specifically it is efficient: to increase numerical accuracy and refine the spatial mesh in our standard Fourier expansion approach, we need to increase the number of Fourier modes, which rapidly becomes computationally expensive.

A more efficient approach is to start directly from the time-independent directly driven NLS. This equation is a second-order ODE, which is easily reduced to a system of first-order ODEs:

$$\begin{cases} u_x = v, \\ v_x = -2|u|u + u - h - i\gamma u, \end{cases} \tag{6.1}$$

where u and v are complex. Recall (§4.1.1) that the evenness of the stationary $\psi_\pm$ solitons implies that they can always be described as periodic in space. Thus, continuing stationary soliton solutions to the (time dependent) directly driven NLS reduces to solving system (6.1) as a periodic BVP, with periodic boundary conditions*

$$u(0) = u(L), \quad v(0) = v(L). \tag{6.2}$$

Continuing the stationary solitons in this manner allows us to utilize AUTO's built-in collocation mesh and achieve a spatial accuracy of $\Delta x < 0.05$ on the spatial domain of length $L = 32\pi$. Our computations for the ψ_- soliton showed that the domain is finite but and extends to $(h, \gamma) = (0.426, 0.663)$. This value was robust under refinements of the collocation mesh. Moreover, it is in exceptionally close agreement with the results tabulated in [7], who found that the ψ_- solution domain extends to $(h, \gamma) = (0.426, 0.66)$. The results for the ψ_- solution are plotted in Figure 6.1.

Using the same algorithm, the ψ_+ soliton domain was also demonstrated to be finite and extended no further than $(h, \gamma) = (0.391, 0.592)$.

*To actually implement this in AUTO we scale out the spatial domain length L.

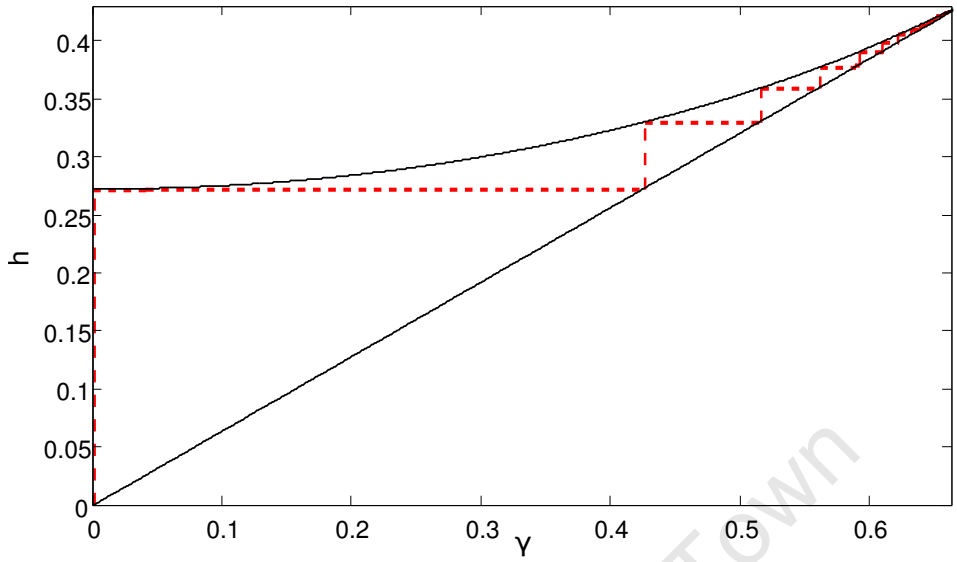

Figure 6.1: Domain of existence of the stationary ψ_- soliton. The existence boundaries, shown in black, were computed by interpolating the end points of each branch of the red continuation curve of the stationary ψ_- soliton. The stability of the solutions is not shown.

6.2 Temporally-periodic solitons

6.2.1 Strong damping: $\gamma = 0.2$

The bifurcation curve of a representative solution for strong damping is presented in Figure 6.2. The periodic solution is born in the Hopf bifurcation of the stationary ψ_- soliton (1.15) at $h = 0.181$. Near the Hopf point the soliton is well approximated by the stationary ψ_- soliton and is stable. As the driving strength h is increased, and we follow the soliton along the lower (solid) branch in Figure 6.2, the amplitude of oscillation of the soliton becomes more pronounced but the soliton remains stable. At the maximum of the lower branch, marked by the blue dot (reconstructed in Figure 6.4), the soliton is already surrounded by large-amplitude radiation.

Continuing the solution further with increasing h, the neighbouring radiation half-wavelengths grow in amplitude. At the right-most end point, where the lower branch meets the upper branch, a periodic soliton complex has formed. A comparison of the real and imaginary parts of the soliton complex to the corresponding *damped* stationary solitons, reveal that the solution is composed of a central periodic ψ_- soliton and two distinct neighbouring periodic ψ_+ solitons.

Following the solution back along the upper (dashed) branch with decreasing driving strength h, the solution loses stability and the neighbouring periodic ψ_+ solitons oscillate with decreasing amplitude until they are virtu-

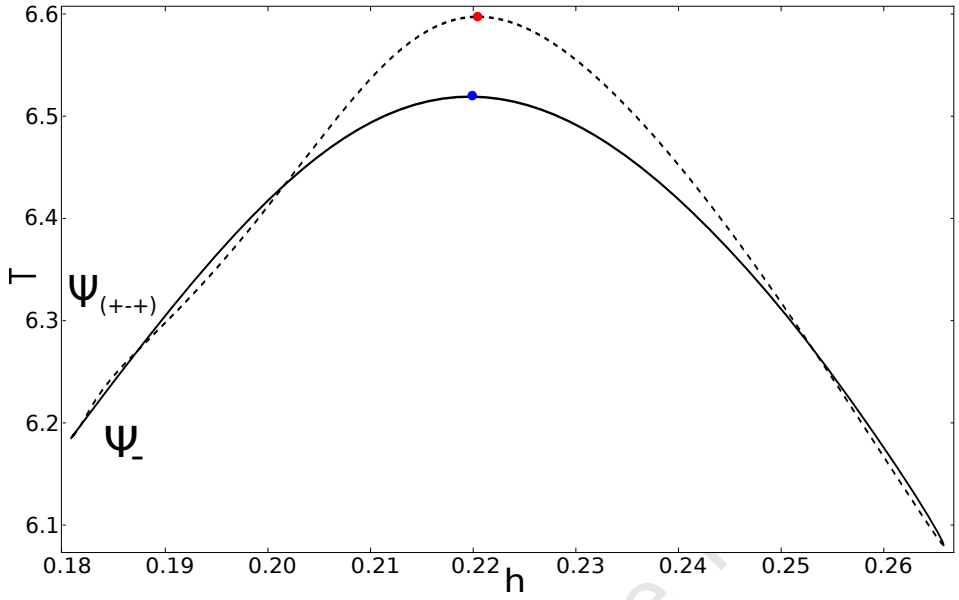

Figure 6.2: Bifurcation diagram of the time-periodic directly driven NLS soliton with $\gamma = 0.2$ and $L = 32\pi$. Two representative solutions (blue and red dots) are shown in Figures 6.4 and 6.5 respectively.

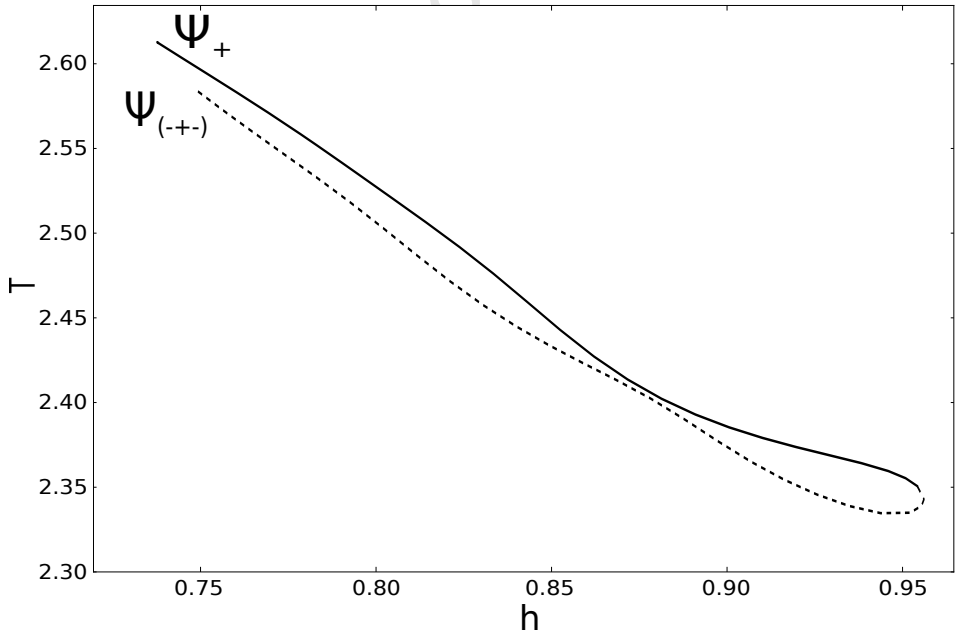

Figure 6.3: Bifurcation diagram of the time-periodic *parametrically* driven NLS soliton with $\gamma = 0.35$ and $L = 32\pi$, included for comparison with Figure 6.2.

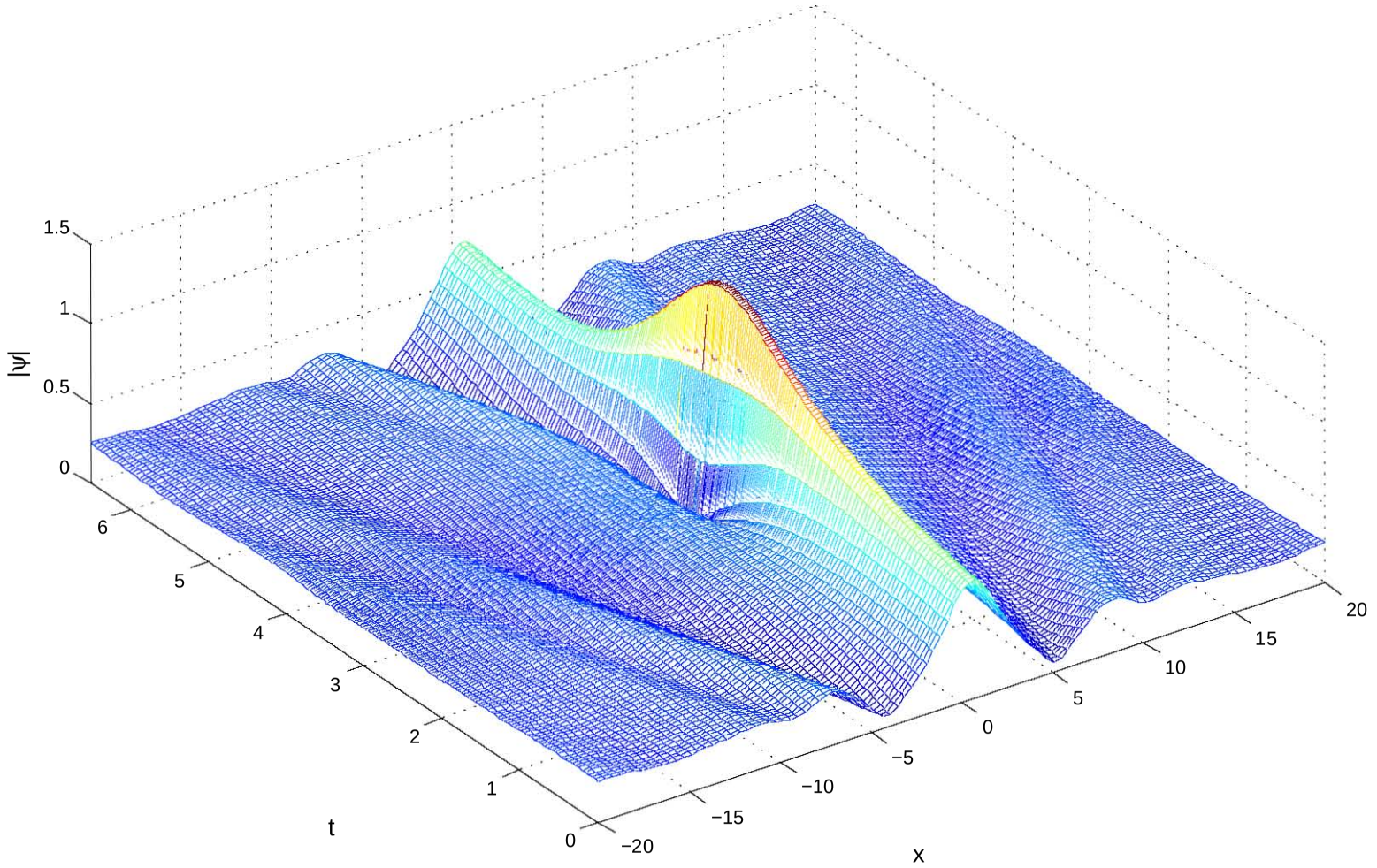

Figure 6.4: Absolute value of the periodic soliton with $\gamma = 0.2$, $h = 0.219$ and $T = 6.52$ along the lower branch in Figure 6.2 (blue dot solution). Only the central section $[-20, 20]$ of the full spatial interval $[-16\pi, 16\pi]$ is shown. The soliton is surrounded by large-amplitude radiation that will seed the periodic ψ_+ solitons that flank the periodic ψ_- soliton in Figure 6.2.

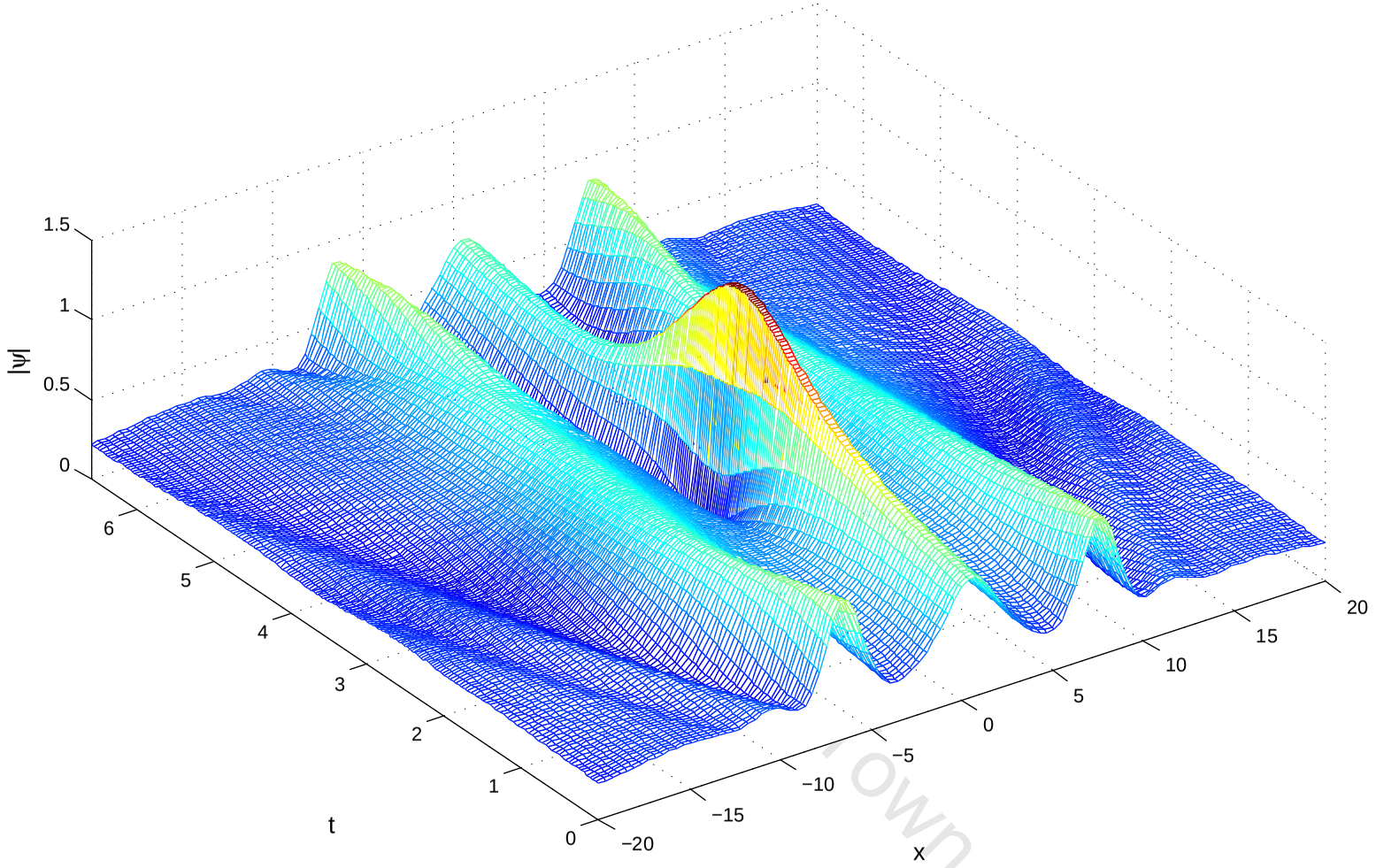

Figure 6.5: Absolute value of the periodic soliton with $\gamma = 0.2$, $h = 0.222$ and $T = 6.60$ along the upper branch in Figure 6.2 (red dot solution). Only the central section $[-20, 20]$ of the full spatial interval $[-16\pi, 16\pi]$ is shown. The periodic ψ_- soliton is now flanked by two periodic ψ_+ solitons. The interaction between the periodic ψ_+ solitons which flank the periodic ψ_- soliton is minimal: both of the periodic ψ_+ solitons remain centred at $|x| = 7$ over the full period. Contrast this with the solitons which flank the periodic ψ_- solitons in the case of moderate damping (Figure 6.7).

ally stationary (cf. red dot solution reconstructed in Figure 6.5). The central periodic ψ_- soliton also oscillates with decreasing amplitude, although its transformation to the stationary ψ_- soliton is slower and only complete by the left most end point of the upper (dashed) branch at $h = 0.181$. Note that, although the solutions at the end point of the upper (dashed) and the lower (solid) branch have similar periods, they do *not* coincide.

It is interesting to compare the bifurcations curves for strong damping in the cases of parametric (Figure 6.3) and direct (Figure 6.2) driving. For strong damping, Barashenkov, Zemlyanaya and van Heerden [15] observed a very similar organisation of the phase space of the periodic solitons in the case of parametric driving to that witnessed here in the case of direct driving. The bifurcation curve of the periodic parametrically driven NLS soliton is also composed of two branches, one starting from the stationary ψ_+ soliton (1.4) and the other ending with the stationary $\psi_{(-+-)}$ soliton complex. In close similarity to the case of direct driving, for parametric driving, the ψ_+ branch is stable while $\psi_{(-+-)}$ branch is unstable.

On the other hand, there are differences in the appearance of bifurcation curves between the direct and parametric cases. Most notably, while the bifurcation curve in the direct case is very nearly closed, the bifurcation curve in the parametric case is not. The shape of the respective bifurcations curves are also different in the two cases.

6.2.2 Moderate damping: $\gamma = 0.15$

The bifurcation curve for $\gamma = 0.15$, an exemplary case for the moderately damped system, is shown in Figure 6.6. The evolution of the periodic solution along the bifurcation curve, as a function of the driving strength h, is similar to the strongly damped case. Indeed, interpreting the corresponding "lower" branch of the bifurcation curve in Figure 6.6 as the branch that begins at the Hopf point at $h = 0.140$ and ends at the right-most end point $h = 0.248$, we observe a similar evolution of the periodic solution: as the driving strength h is increased, large-amplitude radiation waves grow around the soliton until the neighbouring half wavelengths eventually develop into periodic ψ_+ solitons, as verified by an analysis of their real and imaginary parts. Similar remarks apply to the corresponding "upper" branch along which, through decreasing driving strengths h, the periodic soliton complex slowly loses its time dependence evolving into the stationary $\psi_{(+-+)}$ complex.

However, there are also clear dissimilarities between the moderately and strongly damped cases. Although in both the strongly and moderately damped systems similar soliton complexes are present, the interaction between the constituents of the complex is different in the two cases. While the strongly damped periodic soliton complexes are marked by clearly separated single-solitons, the moderately damped complexes are less well defined. Fur-

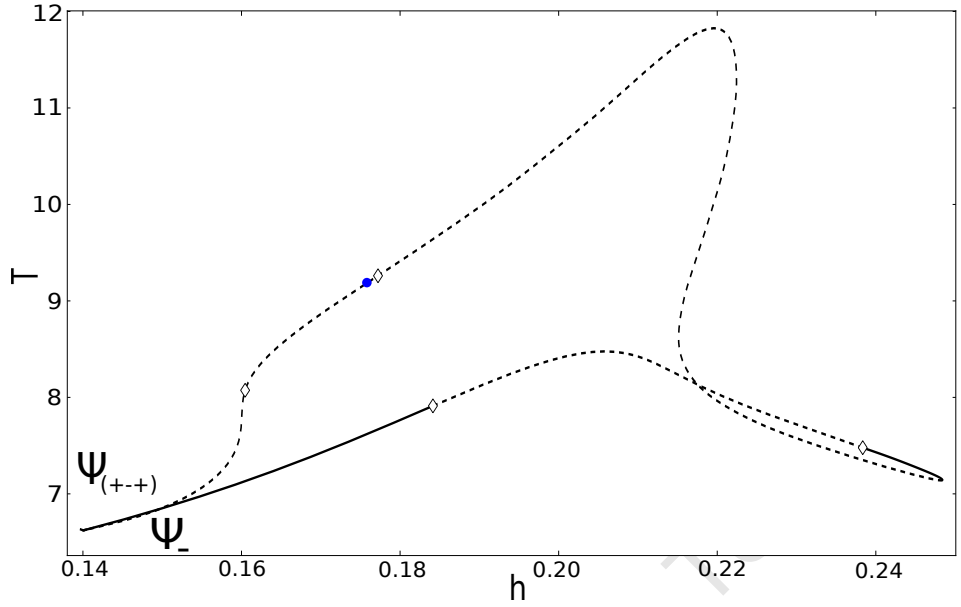

Figure 6.6: Bifurcation diagram for the time-periodic directly driven NLS soliton with $\gamma = 0.15$ and $L = 32\pi$. The diamonds indicate period-doubling bifurcations. A representative solution (blue dot) is shown in Figure 6.7.

thermore, the constituent single-solitons in the strongly damped case show very little interaction within the complex as exemplified by Figure 6.5. The constituent single-solitons of the moderately damped complexes are, in contrast, very strongly interacting as illustrated by Figure 6.7.

The bifurcation curves also differ between the two damping regimes. Specifically, unlike the strongly damped system, the bifurcation curve of the moderately damped periodic solutions is composed of two separate stability regions and multiple period-doubling bifurcations are present. Nevertheless, we can still envisage a continuous deformation of the bifurcation curve of the moderately damped system (Figure 6.6) into that of the strongly damped system (Figure 6.2).

It is interesting to note that the differences highlighted above - that of two separate stability regions on the "lower" branch that lose and then regain stability through period-doubling bifurcations - also occur in the parametrically driven NLS in the equivalent case of moderately damping. Indeed, Barashenkov, Zemlyanaya and van Heerden [15] observe, in what they term the "intermediate" damping regime ($\gamma = 0.265$), the same stability switching along with the evolution of the stationary ψ_+ soliton into the stationary $\psi_{(-+-)}$ soliton complex.

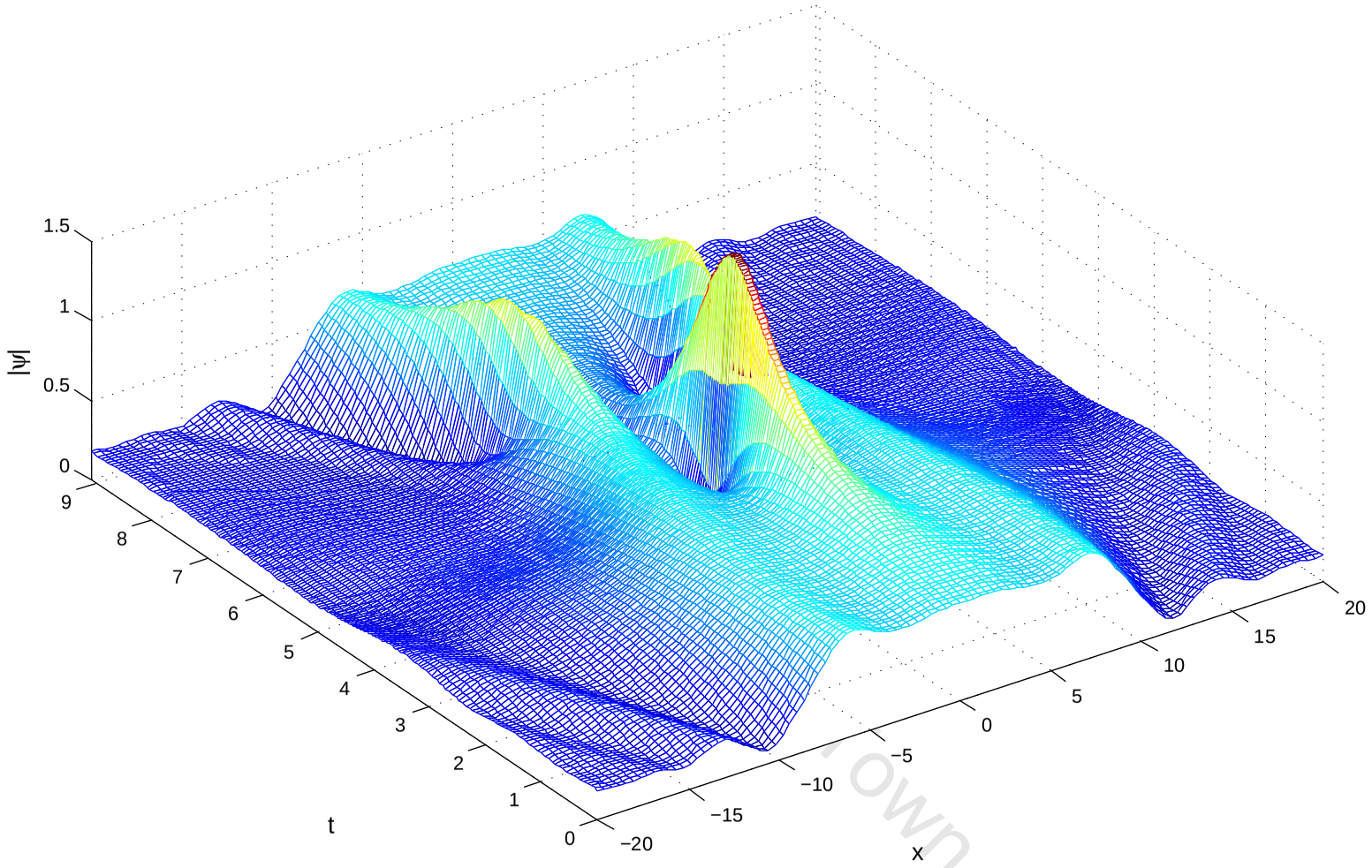

Figure 6.7: Absolute value of the periodic solution with $\gamma = 0.15$, $h = 0.174$ and $T = 9.08$ along the upper branch in Figure 6.2 (blue dot solution). Only the central section $[-20, 20]$ of the full spatial interval $[-16\pi, 16\pi]$ is shown. The soliton complex consists of a central periodic ψ_- soliton and two closely neighbouring periodic ψ_+ solitons. There is strong interaction between periodic ψ_- soliton and the periodic ψ_+ solitons which flank it: the respective cores of the periodic ψ_+ solitons move from $|x| = 5$ to $|x| = 6.5$ (and then back again) over the course of a one period.

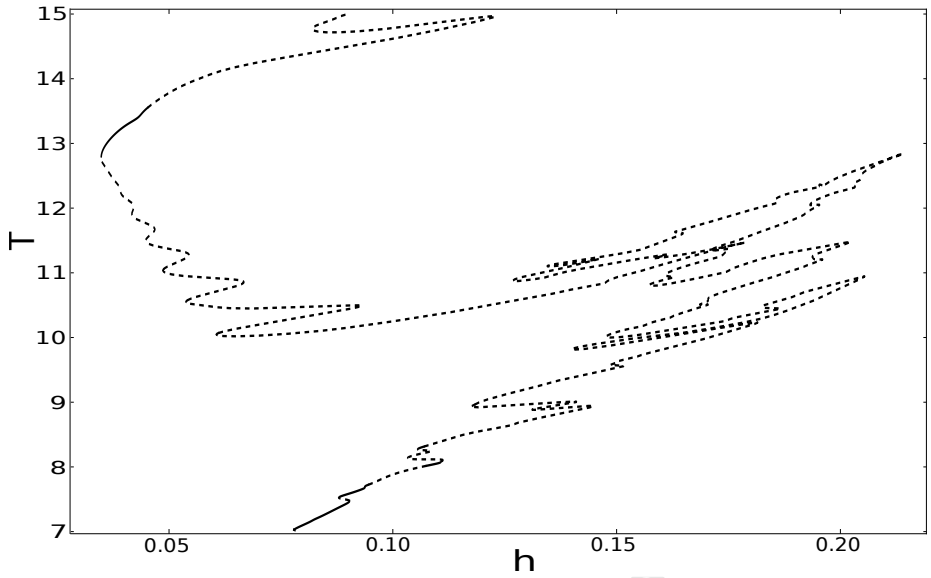

Figure 6.8: Bifurcation diagram of time-periodic directly driven NLS soliton with $\gamma = 0.01$ and $L = 32\pi$ for small periods $T \leq 15$. Period-doubling bifurcations are not shown.

6.2.3 Weak damping: $\gamma = 0.01$

The weakly damped system is dominated by large-amplitude radiation. As in the case of parametric driving, the bifurcation curves are disrupted by fine structure oscillations. A typical case is included in Figure 6.8. Although we will not go into the details in this dissertation, we hypothesise that it is again the presence of large-amplitude radiation on a finite periodic spatial domain that is warping the bifurcation curve and generating the equivalent fine structure in the directly driven NLS.

6.2.4 Bifurcation diagram

Barashenkov and Smirnov [7] constructed a detailed stability and existence chart for the stationary solitons of the directly driven NLS (reproduced in Figure 1.3). Spatschek, Pietsch, Laedke and Eickermann [76] later produced an approximate attractor chart for both stationary and temporally periodic solutions of the directly driven NLS (cf. Figure 1.4). Our chart, shown in Figure 6.9, correlates well with that of [76] and [7] but also offers a more refined resume of the bifurcating behaviour of the directly driven NLS in (h, γ) parameter space. The chart was constructed from our continuation results of the stationary solitons and the one-parameter bifurcation curves for the Hopf and period-doubling bifurcations of the periodic solitons. The

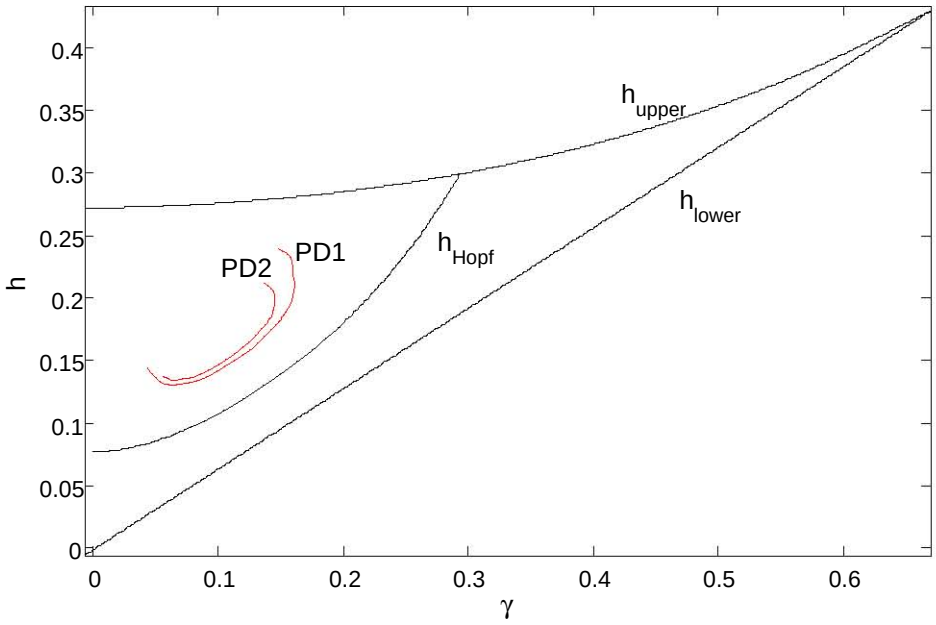

Figure 6.9: Soliton attractor chart of the directly driven NLS. h_{Hopf} denotes the Hopf curve; h_{upper} and h_{lower} demarcate the respective upper and lower boundaries of the domain of existence of the stationary $\psi\pm$ solitons; and PD1 and PD2 are the respective period-doubling bifurcation curves of the period-one and period-two solitons. No homoclinic solution arises in the directly driven case. Further details are given in the text.

bifurcation curves were computed as in the parametric case (see §5.4).

Between the h_{Hopf} and h_{lower} curves the only nontrivial solutions found are the stationary solitons $\psi_{\pm}$ (1.15), whereas between the h_{upper} and h_{Hopf} curves both stationary and periodic solitons coexist. Inside curve PD1 period-two solitons are found and inside curve PD2 period-four and higher period solitons are also found.

There are several key differences between the direct (Figure 6.9) and parametric (Figure 5.20) attractor charts. Firstly, the domains of existence of the stationary $\psi_{\pm}$ solitons are finite in the case of direct driving. Secondly, in contrast to the parametric case, the period-doubling bifurcation curves in the direct case do not extend to small γ. Finally, no homoclinic solution arises in the directly driven case.

Chapter 7

Conclusions

In this thesis we have developed a numerical continuation algorithm, implemented in AUTO, for the continuation of temporally periodic solitons of the parametrically driven NLS and the directly driven NLS. Our algorithm has enabled us to investigate periodic soliton solutions in two previously understudied parameter regimes in the parametrically driven NLS, namely large-period periodic solutions and the weakly damped system, and also offer a cursory study of the periodic soliton solutions of the directly driven NLS.

Access to large-period periodic solitons of the parametrically driven NLS revealed the full dynamics of these solutions of the moderately damped system. In this regime, we found that the parametrically driven NLS exhibits a bifurcating structure that can be understood in light of Shil'nikov's results: the dynamics of the time-periodic solitons are dominated by the interplay of the homoclinic orbit and the saddle-focus stationary ψ_- soliton. This result is naturally of contextual interest, but is also of theoretical interest as we have found an instance where finite dimensional dynamical systems theory predications are applicable to the infinite dimensional case.

A large portion of our study was devoted to investigating weakly damped periodic parametrically driven NLS solitons. In the weakly damped regime, we found that the characteristic snaking structure of the bifurcation curve was disrupted by fine structure oscillations. The growth of this fine structure was coupled with the proliferation of stable periodic solutions. These stable time-periodic solutions are important physically realisable states in the practically relevant weakly damped regime. A summary of the appearance and growth of these new regions of stability is given in the "Feigenbaum tree" in Figure 5.19.

It should be emphasised that the fine structure is in part a consequence of the finite periodic spatial interval. On the infinite spatial interval this fine structure and will not persist. The remaining dynamics of the time-periodic soliton solutions would simply be explained by Shil'nikov's mechanism. The

effect of the periodic finite spatial interval is further illustrated by the existence of *undamped* periodic solitons of the parametrically driven NLS, which do not exist on the infinite interval.

While a strong connection between the large amplitude radiation waves on the finite periodic spatial interval and the fine structure of the bifurcation curves was established, we were unable to elucidate the exact mechanism giving rise the fine structure oscillations in the weakly damped system. This mechanism, along with understanding the new regions of stable time-periodic solutions in detail, remain important open questions and points of great interest for future research.

We were also able to track the behaviour and evolution of the periodic driven driven NLS soliton as a function of the driving strength h for various damping regimes. The phase space of the directly driven NLS for strong damping was found to be very similar to that of the strongly damped system in the case of parametric driving. In both systems as h is increased the single-period soliton born from the stationary soliton at the point of Hopf bifurcation evolves into a periodic three-soliton complex, while subsequently decreasing h results in the periodic complex becoming progressively less time dependent and ultimately forming a stationary soliton complex.

In the case of moderate damping the periodic directly driven NLS soliton undergoes much the same evolution as in the strongly damped system, originating from the stationary soliton and developing into the stationary three-soliton complex as the driving strength h is varied. We also observe two separate branches of stable periodic solitons: the periodic soliton born at the Hopf point is stable but loses stability through a period-doubling bifurcation shortly before regaining it through another period-doubling bifurcation. This precise evolution of the single-soliton to the soliton complex along with the branches of stability separated by period-doubling bifurcations also occurs in the "intermediately" [15] damped parametrically driven NLS.

Further parallels were noted in the weakly damped regimes of the two systems. Indeed, similar fine structure oscillations were found to proliferate throughout the bifurcation curves with increasing amplitude as the damping was decreased. Although we did not go into the details in this work, we speculate that a similar radiation dependent mechanism as in the parametrically driven NLS is warping the bifurcation curve and generating this fine structure. A detailed study of this phenomenon is left to future research.

Although we observed many similarities between the cases of direct and parametric driving, we also noted important contrasts between the two systems. Firstly, while the stationary parametrically driven NLS solitons are known to exist for all γ, the stationary solitons of the directly driven system only have a finite domain of existence, as demonstrated numerically. Secondly, no homoclinic solutions exist in the case of direct driving and hence, for moderate damping, the bifurcation structure of the periodic soli-

tons of the directly driven NLS does *not* display any characteristic snaking structure.

We concluded our study of both the parametric and the directly driven systems by generating refined bifurcation diagrams shown in Figures 5.20 and 6.9 respectively. The parametrically driven NLS chart served largely as a means to corroborate summaries in the literature which were generated using more approximate numerical methods, while the directly driven NLS chart offered a more substantial refinement of previous studies.

Further to all these results we have developed an continuation algorithm that is of general applicability to the study of periodic solutions of a variety of PDEs. Indeed, our algorithm is suited to the study of temporally periodic solutions of any PDE bearing some spatial periodicity. Future research will be built around applying our continuation algorithm to other soliton bearing PDEs such as the Ginzburg-Landau equation.

Acknowledgements

I would like to thank my supervisor, Igor Barashenkov, for offering the encouragement, focused guidance and sizeable input to complete this work. I am also grateful to Andrew Lewis and the rest of the SAGrid team for granting me access to the UCT high performance computing servers; their support and interest in the numerical work was invaluable. Further thanks is to Andrey Pototsky for help in implementing the FFTW library.

Bibliography

[1] A. A. Aigner, A. R. Champneys and V. M. Rothos, *A new barrier to the existence of moving kinks in Frenkel-Kontorova lattices*, Phys. D, 186:148-170 (2003).

[2] N. V. Alexeeva, I. V. Barashenkov and D. E. Pelinovsky, *Dynamics of the parametrically driven NLS solitons beyond the onset of the oscillatory instability*, Nonlinearity, 12:103140 (1999).

[3] D. M. Ambrose and J. Wilkening, *Computation of time-periodic solutions of the Benjamin-Ono equation*, J. Nonlinear Sci., 20:277-308 (2010).

[4] A. Andronov and E. Leontovich, *Some cases of the dependence of the limit cycles upon parameters*, Uchen. Zap. Gork. Univ., 6:3-24 (1939). In Russian.

[5] I. V. Barashenkov, M. M. Bogdan and V. I. Korobov, *Stability diagram of the phase-locked solitons in the parametrically driven, damped nonlinear Schrödinger equation*, Europhys. Lett., 15:113-118 (1991).

[6] I. V. Barashenkov, M. M. Bogdan, and T. Zhanlav, in *Nonlinear World*, Proceedings of the Fourth International Workshop on Nonlinear and Turbulent Processes in Physics, Kiev (1989), edited by V. G. Bar'yakhtar *et al.*, World Scientific, Singapore, 3 (1990).

[7] I. V. Barashenkov and Y. S. Smirnov, *Existence and stability chart for the ac-driven, damped nonlinear Schrödinger solitons*, Phys. Rev. E, 54:57075725 (1996).

[8] I. V. Barashenkov, Y. S. Smirnov and N. V. Alexeeva, *Bifurcation to multisoliton complexes in the ac-driven, damped nonlinear Schrödinger equation*, Phys. Rev. E, 57:23502364 (1998).

[9] I. V. Barashenkov and E. V. Zemlyanaya, *Existence threshold for the ac-driven damped nonlinear Schrödinger solitons*, Physica D, 132:363372 (1999).

[10] I. V. Barashenkov and E. V. Zemlyanaya, *Stable complexes of parametrically driven, damped nonlinear Schrödinger solitons*, Phys. Rev. Lett. 83:2568-2571 (1999).

[11] I. V. Barashenkov and E. V. Zemlyanaya, *Travelling solitons in the damped-driven nonlinear Schrödinger equation*, SIAM J. Appl. Math., 64:800-818 (2004).

[12] I. V. Barashenkov and E. V. Zemlyanaya, *Soliton complexity in the damped-driven nonlinear Schrödinger equation: Stationary to periodic to quasiperiodic complexes*, Phys. Rev. E, 83:056610 (2011).

[13] I. V. Barashenkov and E. V. Zemlyanaya, *Travelling solitons in the externally driven nonlinear Schrödinger equation*, arXiv:1107.0483v1 [nlin.PS] (2011).

[14] I. V. Barashenkov, E. V. Zemlyanaya and M. Bär, *Travelling solitons in the parametrically driven nonlinear Schrödinger equation*, Phys. Rev. E, 64:016603 (2001).

[15] I. V. Barashenkov, E. Zemlyanaya and T. van Heerden, *Time-periodic solitons in a damped-driven nonlinear Schrödinger equation*, Phys. Rev. E 83:056609 (2011).

[16] M. Beck, J. Knobloch, D. J. B Lloyd, B. Sandstede and T. Wagenknecht, *Snakes, ladders and isolas of localized patterns*, SIAM J. Math. Anal., 41:936-972 (2009).

[17] M. Bondila, MSc Thesis: Numerical study of the parametrically driven damped nonlinear Schrödinger equation, Dept. of Math. & Appl. Math., University of Cape Town (1995).

[18] M. Bondila, I. V. Barashenkov and M. Bogdan, *Topography of attractors of the parametrically driven nonlinear Schrödinger equation*, Physica D, 87:314-329 (1995).

[19] H. R. Brand, C. Fradin, P. Finn, W. Pesch and P. Cladis, *Electroconvection in nematic liquid crystals: Comparison between experimental results and the hydrodynamic model*, Phys. Lett. A, 235:508-514 (1997).

[20] J. Burke and E. Knobloch , *Snakes and ladders: localized states in the Swift-Hohenberg equation*, Phys. Lett. A, 360:681-688 (2007).

[21] J. Burke and E. Knobloch, *Multipulse states in the Swift-Hohenberg equation*, Dyn. Sys. Suppl., 109-117 (2009).

[22] M. Cabral and R. Rosa, *Chaos for a damped and forced KdV equation*, Physica D, 192:265-278 (2004).

[23] D. Cai, A. R. Bishop, N. Grønbech-Jensen and B. A. Malomed, *Bound solitons in the ac-driven, damped nonlinear Schrödinger equation*, Phys. Rev. E, 49:16771679 (1994).

[24] M. G. Clerc, S. Coulibaly and D. Laroze, *Localized states beyond the asymptotic parametrically driven amplitude equation*, Phys. Rev. E, 77:056209 (2008).

[25] M. Cross and P. Hohenberg, *Pattern formation outside of equilibrium*, Rev. Mod. Phys., 65:851-1112 (1993).

[26] J. H. P. Dawes, *Modulated and localized states in a finite domain*, SIAM J. App. Dyn. Sys., 8:909-930 (2009).

[27] I. H. Deutsch and I. Abram, *Reduction of quantum noise in soliton propagation by phase-sensitive amplification*, JOSA B, 11:2303-2313 (1994).

[28] A. Dhooge, W. Govaerts and Y. A. Kuznetsov, *MatCont: A Matlab package for numerical bifurcation analysis of ODEs*, ACM Trans. on Math. Software 29:141-164 (2003).

[29] E. Doedel, *AUTO: A program for the automatic bifurcation analysis of autonomous systems*, Congr. Numer., 30:265384 (1981).

[30] E. J. Doedel, B. E. Oldeman , F. Dercole, C. Zhang, R. Paffenroth, A. R. Champneys, T. Fairgrieve , Y. Kuznetsov, B. Sandstede and X. Wang, *AUTO-07P : Continuation and Bifurcation Software for Ordinary Differential Equations*, Technical Report, Concordia University, Montreal (2007).

[31] D. B. Duncan, J. C. Eilbeck, H. Feddersen and J. A. D. Wattis, *Solitons on lattices*, Physica D, 68:111 (1993).

[32] J. C. Eilbeck and R. Flesch, *Calculation of families of solitary waves on discrete lattices*, Phys. Lett. A, 149:200202 (1990).

[33] C. Elphick and E. Meron, *Localized structures in surface waves*, Phys. Rev. A, 40:3226 (1989).

[34] J. Epperson, *An Introduction to Numerical Methods and Analysis*, Rev. ed., Wiley (2007).

[35] J. Evans, N. Fenichel and J. A. Feroe, *Double impulse solutions in nerve axon equations*, SIAM J. Appl. Math., 42:219-234 (1983).

[36] J. A. Feroe, *Existence and stability of multiple impulse solutions of a nerve axon equation*, SIAM J. Appl. Math., 42:235-246 (1983).

[37] J. Fineberg, *Physics in a jumping sandbox*, Nature, 382:793-764 (1996).

[38] H. Friedel, E. W. Laedke and K. H. Spatschek, *Bifurcations and nonlinear dynamics of surface waves in Faraday resonance*, J. Fluid Mech., 284:341-358 (1995).

[39] M. Frigo and S. G. Johnson, *The design and implementation of FFTW3*, Proc. IEEE 93:216231 (2005).

[40] P. Glendinning and C. Sparrow, *Local and global behavior near homoclinic orbits*, J. Stat. Phy., 35:645-696 (1983).

[41] J. Guckenheimer and P. J. Holmes, *Nonlinear Oscillations, Dynamical Systems and Bifurcations of Vector Fields*, Springer-Verlag, New York (1983).

[42] S. P. Hastings, *Single and multiple pulse waves for the Fitzhugh-Nagumo equations*, SIAM J. Appl. Math., 42:247-260 (1982).

[43] Y. Hiraoka and T. Ogawa, *Rigorous numerics for localized patterns to the quintic SwiftHohenberg equation*, Japan J. Indust. Appl. Math., 22:57-75 (2005).

[44] R. Hirota, *The Direct Method in Soliton Theory*, Cambridge University Press (2004).

[45] R. Hirota and J. Satsuma, *A variety of nonlinear network equations generated from the Bäcklund transformation for the Toda lattice*, Progress of The. Phy. Suppl., 59:64100 (1976).

[46] A. Homburg, PhD thesis: *Some global aspects of homoclinic bifurcations of vector fields*, Department of Mathematics, University of Groningen (1993).

[47] A. Homburg and B. Sandstede, *Homoclinic and heteroclinic bifurcations in vector fields*, Handbook of Dyn. Sys., 3:379-524 (2010).

[48] S. M. Houghton and E. Knobloch, *Homoclinic snaking in bounded domains*, Phys. Rev. E., 80:026210 (2009).

[49] T.-C. Jo and D. Armbruster, *Localized solutions in parametrically driven pattern formation*, Phys. Rev. E, 68:016213 (2003).

[50] D. J. Kaup and A. C. Newell, *Solitons as particles, oscillators, and in slowly changing media: A singular perturbation theory* Proc. R. Soc. London Ser. A, 361:413-446 (1978).

[51] E. Knobloch, D. Moore, J. Toomre and N. O. Weiss, *Transitions to chaos in two-dimensional double-diffusive convection*, J. Fluid Mech., 166:409-448 (1986).

[52] M. Kollmann, H. W. Capel, T. Bountis, *Breathers and multibreathers in a periodically driven damped discrete nonlinear Schrödinger equation*, Phys. Rev. E 60:1195-1211 (1999).

[53] Y. A. Kuznetsov, *Elements of Applied Bifurcation Theory*, 2nd ed., Springer (1998).

[54] E. W. Laedke and K. H. Spatschek, *On localized solutions in nonlinear Faraday resonance*, J. Fluid Mech., 223:589-601 (1991).

[55] J. Lee-Thorp, BSc(Hons) project: *Spectral continuation algorithm for the parametrically driven damped nonlinear Schrödinger equation*, Dept. of Math. & Appl. Math., University of Cape Town (2010).

[56] D. J. B. Lloyd , B. Sandstede , D. Avitabile and A. R. Champneys, *Localized hexagon patterns of the planar Swift-Hohenberg equation*, SIAM Journal on App. Dyn. Sys., 7:1049-1100 (2008).

[57] S. Longhi, *Ultrashort-pulse generation in degenerate optical parametric oscillators*, Opt. Lett., 20:695-697 (1995).

[58] K. Lust and D. Roose, *Computation and bifurcation analysis of periodic solutions of large-scale systems*. In E. Doedel and L.S. Tuckerman, editors, *Numerical methods for bifurcation problems and large-scale dynamical systems*, Vol. 119 of IMA Vol. Math. & Appl., Springer-Verlag (2000).

[59] Y.-P Ma, J. Burke and E. Knobloch, *Defect-mediated snaking: A new growth mechanism for localized structures*, Physica D: Nonlinear Phenomena, 23:1867-1883 (2010).

[60] A. Mazor and A. R. Bishop, *Phase-pulling and breather instability in an AC-driven damped one-dimensional sine-Gordon system* Physica D, 27:269-293 (1987).

[61] A. Mazor, A. R. Bishop and D. W. McLaughlin, *Phase-pulling and space-time complexity in an ac driven damped one-dimensional sine-Gordon system* Phys. Lett. A, 119:273-279 (1986).

[62] J. M. McSloy, W. J. Firth, G. K. Harkness and G.-L. Oppo, *Computationally determined existence and stability of transverse structures II: Multipeaked cavity solitons*, Phys. Rev. E, 66:046606 (2002).

[63] A. Mecozzi, L. Kath, P. Kumar and C. G. Goedde, *Long-term storage of a soliton bit stream by use of phase-sensitive amplification*, Opt. Lett. 19:2050-2052 (1994).

[64] T. R. O. Melvin, A. R. Champneys, P. G. Kevrekidis and J. Cuevas, *Radiationless travelling waves in saturable nonlinear Schrödinger lattices*, Phys. Rev. Lett., 97:124101 (2006).

[65] T. R. O. Melvin, A. R. Champneys, P. G. Kevrekidis and J. Cuevas, *Travelling solitary waves in the discrete Schrödinger equation with saturable nonlinearity: Existence, stability and dynamics*, Phys. D, 237:551-567 (2008).

[66] T. R. O. Melvin, A. R. Champney and D. E. Pelinovsky, *Discrete Traveling Solitons in the Salerno Model* SIAM J. Appl. Dyn. Sys., 8:689-709 (2009).

[67] J. W. Miles, *Parametrically excited solitary waves*, J. Fluid Mech. 148:451-460 (1984).

[68] Y. Pomeau, *Front motion, metastability and subcritical bifurcations in hydrodynamics*, Physica D, 23:3-11 (1986).

[69] D. E. Pelinovsky, T. R. O. Melvin and A. R. Champneys, *One-Parameter Localized Traveling Waves in Nonlinear Schrödinger Lattices*, Phys. D, 236:22-43 (2007).

[70] R. Richter R and I. V. Barashenkov, *Two-dimensional solitons on the surface of magnetic fluids*, Phys. Rev. Lett. 94:184503 (2005).

[71] S. Residori, *Patterns, fronts and structures in a liquid-crystal-light-valve with optical feedback*, Phys. Rep., 416:201-272 (2005).

[72] B. Sandstede, PhD thesis: *Verzweigungstheorie homokliner Verdopplungen*, Institut für Angewandte Analysis und Stochastik, Berlin, Germany (1993). In German.

[73] B. Sandstede, *Center manifolds for homoclinic solutions*, J. Dyn. & Diff. Eq., 12(3):449-510 (2000).

[74] L. P. Shilnikov, *A case of existence of a countable number of periodic motions*, Soviet Math. Dokl., 8:54-58 (1965).

[75] L. P. Shilnikov, *A contribution to the problem of the structure of an extended neighborhood of a rough equilibrium state of saddle-focus type*, Math. USSR-Sb., 10:91-102 (1970).

[76] K. H. Spatschek, H. Pietsch, E. W. Laedke and Th. Eickermann, *On the role of soliton solutions in temporal chaos: Examples for plasmas and related systems in singular behaviour and bonlinear dynamics*. In T. Bountis and St. Pnevmatikos, editors, Proceedings of the International Conference on Singular Behavior and Nonlinear Dynamics, Samos 555-564, World Scientific (1988).

[77] T. R. Taha and M. J. Ablowitz, *Analytical and numerical aspects of certain nonlinear evolution equations*, J. Comput. Phys. 55:192 (1984).

[78] G. Terrones, D. W. McLaughlin, E. A. Overman and A. J. Pearlstein, *Stability and bifurcation of spatially coherent solutions of the damped-driven NLS equation*, SIAM J. Appl. Math. 50:791 (1990).

[79] M. Tlidi, A. G. Vladimirov and P. Mandel, *Interaction and stability of periodic and localized structures in optical bistable systems*, IEEE J. Quant. Electr., 39:216-226 (2003).

[80] M. V. Tratnik and J. E. Sipe, *Bound solitary waves in a birefringent optical fiber*, Phys. Rev. A, 38: 2011-2017 (1988).

[81] C. Tresser, *About some theorems by L. P. Shil'nikov*, Ann. Inst. Henri Poincaré Phys. Théor. 40:441461 (1984).

[82] P. B. Umbanhowar, F. Melo and H. L. Swinney, *Localized excitations in a vertically vibrated granular layer*, Nature, 382:793-796 (1996).

[83] V. K. Vanag and I. R. Epstein, *Stationary and oscillatory localized patterns, and subcritical bifurcations*, Phys. Rev. Lett., 92:128301 (2004).

[84] T. van Heerden, MSc Thesis: *Temporally periodic solitons of the parametrically driven, damped nonlinear Schrödinger equation*, Dept. of Math. & Appl. Math., University of Cape Town (2010).

[85] A. Yochelis, J. Burke and E. Knobloch, *Reciprocal oscillons and nonmonotonic fronts in forced nonequilibrium systems*, Phys. Rev. Lett., 97:254501 (2006).

[86] E. Zemlyanaya and N. Alexeeva, *Oscillating solitons of the driven, damped nonlinear Schrödinger equation*, Theo. & Math. Phys., 59:870-876 (2009).

[87] E. Zemlyanaya and N. Alexeeva, *Breathers in a damped-driven nonlinear Schrödinger equation*, Theo. & Math. Phys., 168:858864 (2011).